Winter 2018

Photocatalytic CO2 reduction using well-defined metal sites on nanostructured surfaces

Thomas G. Fenton
University of New Hampshire, Durham

PHOTOCATALYTIC CO_2 REDUCTION USING WELL-DEFINED METAL SITES ON NANOSTRUCTURED SURFACES

BY

Thomas G. Fenton

BS, State University of New York at Oneonta, 2013

DISSERTATION

Submitted to the University of

New Hampshire

in Partial Fulfillment of

the Requirements for the Degree of

Doctor of Philosophy

in

Chemistry

December, 2018

This dissertation has been examined and approved in partial fulfillment of the requirements for the degree of Doctor of Philosophy in Chemistry by:

Dissertation Director, Gonghu Li, Associate Professor,

Department of Chemistry

Howard R. Mayne, Professor,

Department of Chemistry

Margaret E. Greenslade, Associate Professor,

Department of Chemistry

Roy P. Planalp, Associate Professor,

Department of Chemistry

Jonathan Rochford, Associate Professor, University of Massachusetts Boston

Department of Chemistry

November 8th, 2018

Original approval signatures are on file with the University of New Hampshire Graduate School.

ACKNOWLEDGMENTS

I would like to first extend my thanks to my advisor Dr. Gonghu Li. He has given me a wonderful opportunity to work with him on these research endeavors. His continued support and guidance led me to grow as a scientist and as a professional. I also would like to extend my gratitude to Dr. Howard Mayne, Dr. Margaret Greenslade, Dr. Roy Planalp and Dr. Jonathan Rochford. Each individual supported me through coursework or professional development and their demonstrated professionalism and work-ethic will have a large influence on my continued career.

I am grateful for Nancy Cherim, Kristin Blackwell, Dr. Patricia Wilkinson, John Wilderman, Peg Torch and Laura Bicknell. Their continued support in research and information was immeasurable. I also want to extend my thanks to Cindi Rowher. Her constant support and encouragement made this experience possible and have bettered me as a person.

I also must extend my thanks to my groupmates, Dr. Chao Liu, Dr. Tong Jin, Dr. Michael Louis, Dr. Peipei Huang, Ben Stewart, and others. Without their assistance and teaching, I would not have been able to accomplish this undertaking.

This journey would not have been possible without the encouragement of great friends and family, such as Tyler Bennett, Nikku Ferreri, Dan Keefe, Tiffany Thompson, Jeff Kleinschmidt, my parents Steve and Susanne, and my brothers Craig and William. Their support I am eternally grateful for.

TABLE OF CONTENTS

LIST OF TABLES

TABLE OF FIGURES

ABSTRACT

PHOTOCATALYTIC CO_2 REDUCTION USING WELL-DEFINED METAL SITES ON NANOSTRUCTURED SURFACES

By

Thomas G. Fenton

University of New Hampshire, December, 2018

Carbon dioxide's (CO_2) presence as a greenhouse gas has increased drastically as industry expands across the globe. The utilization of this waste product as a resource is crucial in completing its carbon cycle with fossil fuels. Unfortunately, CO_2 is thermodynamically stable due favorable entropy as a gas and enthalpically stable linear carbonyls. Nature can convert this waste product to a resource via photosynthesis where CO_2 is converted into sugars. Metal catalysts have been developed to mimic photosynthesis with promising results in CO_2 to fuel conversion by using sunlight as an energy source. Homogeneous catalysts have been studied extensively, but they suffer from poor stability under photochemical conditions. Heterogeneous catalysts also have been previously studied due to their stability and low cost but they lack catalytic efficiency. Promising multi-functional catalysts have been developed recently, but there is a lack of understanding on the mechanism of CO_2 reduction for these systems.

In Chapter I, an introduction to CO_2 reduction is provided along with examples of catalysts that have been studied previously in the literature. Multiple types of catalysts are include homogeneous, heterogeneous and hybrid. Hybrid rhenium (Re) catalysts are discussed as well and further explained in Chapter II, where ligand derivatization and surface linkages are optimized for

enhanced CO_2 reduction. The effects of structural changes and surface attachment are investigated, and infrared studies demonstrate the importance of ligand derivatization on catalysis.

Chapter III investigates a different hybrid system where cobalt macrocycles are deposited onto mesoporous silica surfaces. The photocatalytic properties of different macrocyclic ligands are studied. A conjugated macrocycle is introduced for visible light absorption and steric effect. Additionally, each catalyst was heated to see how the changes in surface conformations affect the selectivity of CO_2 reduction.

Heterogeneous catalysts are investigated in Chapter IV where cobalt is deposited as an oxide on silica and mesoporous silica surfaces. Macrocyclic ligands are added during photocatalysis to observe possible *in situ* formation of an active catalytic species. Loadings of cobalt are also varied to study the effect of larger or smaller cobalt sites on the surface. Chapter V expands upon heterogeneous catalysts with Cu and Sn deposited on a commercially available semiconductor, P25 TiO_2. Surface CO adsorption is studied via infrared studies to help understand their role in CO_2 reduction. Additionally, oxygen vacancies on TiO_2 are studied for each sample for their role in the catalytic mechanism.

LIST OF ABBREVIATIONS

ACN	acetonitrile
APTMS	3-aminopropyltrimethoxysilane
ATR	attenuated total reflection
BET	Brunauer, Emmett and Teller
BJH	Barrett, Joyner and Halenda
bpy	2,2'-bipyridine
cyclam	1,4,8,11-tetraazacyclotetradecane
dmbpy	4,4'-dimethyl-2,2'-bipyridine
DCM	dichloromethane
DMF	dimethylformamide
DRIFTS	diffuse reflectance infrared Fourier transform spectroscopy
DRUV	diffuse reflectance ultraviolet-visible spectroscopy
EDTMS	bis[(3-trimethoxysilyl)propyl]-ethylenediamine
FTIR	Fourier transform infrared spectroscopy
HMD	5,7,7,12,14,14-hexamethyl-1,4,8,11-tetra-azacyclotetradeca-4,ll-diene
IR	infrared
MLCT	metal to ligand charge transfer
SBA-15	Santa Barbara Amorphous-15
SEM	scanning electron microscopy
SPR	surface plasmon resonance
TCD	thermal conductivity detector

TEA	triethylamine
TEOA	triethanolamine
THF	tetrahydrofuran
TON	turnover number
TPD	temperature programmed desorption
XPS	X-ray photoelectron spectroscopy

I. INTRODUCTION: CATALYSTS FOR CO_2 REDUCTION

1.1 Motivation for Work

Since modern industrialization, fossil fuels have been used as the primary energy feedstock for various industry sectors such as transportation or electricity. They are energy dense fuels which are unrivaled by any other modern energy fuel sources. Gasoline for example has a theoretical energy density of 13000 Wh/kg, whereas the average battery used in an equivalent electric vehicle only has a theoretical energy density from 200-300 Wh/kg.[1] This drastic difference has led to fossil fuel's extensive use throughout industry and the difficulty in finding alternative sources of energy. Although widely used, a major drawback of these fuels is the byproducts generated from combustion. Carbon dioxide (CO_2) is a major waste product from fossil fuels where the gaseous CO_2 is displaced into the atmosphere post-combustion. Measurements have shown increased CO_2 concentration in the atmosphere over time starting primarily during the industrialization period where fossil fuel use has increased.[2] Due to its stable structure, once CO_2 reaches the atmosphere it is very difficult to remove. It acts as a greenhouse gas absorbing infrared radiation from the earth and reflecting it back towards the surface. This leads to environmental issues such as global warming and climate change which are growing concerns to the scientific community, and society as a whole.

Efforts to reduce CO_2's presence have been focused on utilization of alternative sources of energy, such as wind, water or nuclear.[2-4] However, a common issue is the energy generated by these sources does not meet the current energy demand. One promising approach however is the use of solar fuels. These fuels are defined as resources that are generated by man-made methods of

mimicking photosynthesis. They are produced by catalysts that generate resources that are industrially useful, such as methanol.[5-8] Plants have carried out this process for millions of years and perfected the use of sunlight as a resource to generate sugars. Similarly, catalysts have been synthesized that utilize sunlight as an energy feedstock to generate fuels instead of sugars. In contrast to wind and water energy sources, the energy associated with sunlight hitting the earth in 1 hour can power the world for 1 year. For plants to undergo photosynthesis, their primary source of carbon feedstock is atmospheric CO_2. This is identical for solar fuels where CO_2 can be utilized and converted to fuels either through chemical or thermal transformation.[9-11] We use this as inspiration to develop catalysts that can mimic photosynthesis, by producing solar fuels instead of sugars. These fuels are industrially useful and can help phase out fossil fuels as a primary feedstock, at the same time as reducing CO_2 atmosphere concentration. This will take the waste product generated by fossil fuels and recycle it to a resource, thus completing the carbon cycle for CO_2 emissions.

CO_2 as stated before is stable in its gaseous state and takes a large amount of energy to undergo a chemical transformation. Most industrially useful fuels such as methanol or ethanol can be synthesized from the reduction of CO_2. The potential to reduce to a CO_2 radical (single electron) occurs at -1.9 V vs. normal hydrogen electrode (NHE) which is a large potential difference. Most fuels require multiple electrons and protons for a complete transformation. Reactions can be coupled with a proton source and multiple equivalents to reduce the high potential required (calculated values are from the half-cell reaction in aqueous solutions at pH 7 vs. NHE, Equations 1-1 through 1-5).[12-13]

$CO_2 + 2H^+ + 2e^- \rightarrow HCO_2H$	$E^o = -0.61$ V	(Equation 1-1)
$CO_2 + 2H^+ + 2e^- \rightarrow CO + H_2O$	$E^o = -0.52$ V	(Equation 1-2)
$CO_2 + 4H^+ + 4e^- \rightarrow HCHO + H_2O$	$E^o = -0.48$ V	(Equation 1-3)
$CO_2 + 6H^+ + 6e^- \rightarrow CH_3OH + H_2O$	$E^o = -0.38$ V	(Equation 1-4)
$CO_2 + 8H^+ + 8e^- \rightarrow CH_4 + 2H_2O$	$E^o = -0.24$ V	(Equation 1-5)

Equation Scheme 1. Potentials for various CO_2 reduction products coupled with a proton source versus Normal Hydrogen Electrode (NHE).

However, multiple equivalents of electrons and protons are needed, which is kinetically challenging to have all the equivalents needed near a single reduction site. Nature achieves this by using an enzyme called carbon monoxide dehydrogenase which utilizes a binuclear nickel/iron center to provide two electrons to reduce CO_2 to CO.[14-15] This binuclear system can achieve the close proximity required to generate multiple reductive equivalents on a single CO_2 molecule. Inspired by this enzyme, we aim to develop a catalytic system that can mimic its core catalytic site reducing CO_2 to CO. Having multiple catalytic centers in close proximity working in tandem, drastically reducing kinetic barriers.

Catalysts that can reduce CO_2 to CO have been studied extensively for the last 40 years. A generic mechanism for this reductive transformation is shown below (Equations 2-1 to 2-4).[16-17] Note that the mechanism is for a single e^- transfer, where CO_2 requires two e- for successful reduction to CO. A typical photocatalytic system contains a photosensitizer (P) which absorbs light at either UV or visible wavelengths to generate an excited state (P*). A photosensitizer is an organic molecule or inorganic complex that can absorb light over a wide energy range. The excited species is then reduced by a sacrificial electron donor (D) which gives the singly reduced photosensitizer (P^-) and an oxidized donor (D^+). This photosensitizer then transfers its electron to the catalytic site

(C) to generate the reduced catalytic species (C^-) which can then bind to CO_2 to generate the catalytic product.

$$P + h\upsilon \rightarrow P^* \qquad \text{(Equation 2-1)}$$

$$P^* + D \rightarrow P^- + D^+ \qquad \text{(Equation 2-2)}$$

$$P^- + C \rightarrow P + C^- \qquad \text{(Equation 2-3)}$$

$$C^- + CO_2 \rightarrow C + \text{products} \qquad \text{(Equation 2-4)}$$

Equation Scheme 2. General mechanism for CO_2 reduction products coupled with a photosensitizer and a sacrificial electron donor.

It is essential that the electron transfer between the catalyst and photosensitizer be efficient; if not, the catalytic species cannot be easily generated. To tune this efficiency, the photosensitizer used can be varied or even part of the catalytic site. Most common photosensitizers are p-terphenyl, and the transition metal complex Ruthenium (II) tris bipyridine ($Ru(bpy)_3^{2+}$). These photosensitizers are employed in tandem with a wide variety of catalysts.

Currently, there are 3 types of major catalysts for CO_2 reduction and they include homogeneous, heterogeneous and hybrid. Homogeneous catalysts are organic complexes that contain an atomic metal site that is in the same phase as the reactants. Their catalytic system usually contains the catalyst, an electron donor and a light absorber. Heterogeneous catalysts are solid-state metallic or metal oxide structures that contain multiple reactive sites that are in a separate phase from the reactants. More recently, hybrid catalysts have been developed where homogeneous catalysts are anchored to a solid support which is can be inert or active in CO_2 reduction.

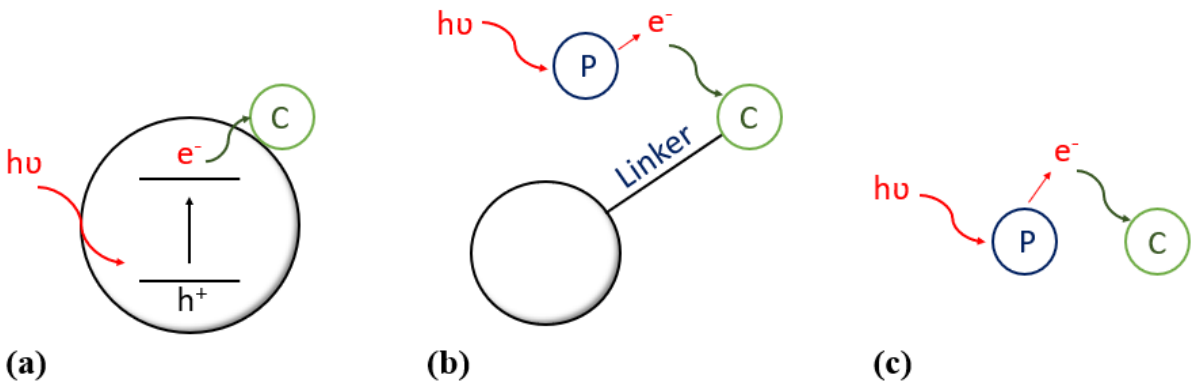

Figure 1. Schematic of the types of catalysts discussed, heterogeneous (a), hybrid (b) and homogeneous (c). Photosensitizer is represented by P and catalysts are represented by C.

1.2 Homogeneous catalysts

Homogeneous catalysts for CO_2 reduction are often inorganic metal complexes with coordinating ligands. Select compounds can be highly active for CO_2 reduction under photo or electrochemical conditions. Also referred to as molecular catalysts, they have high selectivity for reduction products. Advantages to these catalysts include the ability to stabilize reactive intermediate transition states between the linear CO_2 and the product. Once bound, the metal center can then reduce CO_2 and act as an electron transfer agent to donate multiple reductive equivalents. Additionally, the ligands and metals available to perform this can be easily tuned by varying the ligand structures which can be easily functionalized. The effects on catalytic efficiency and reactive intermediates can easily be studied spectroscopically. In particular, two molecular catalyst systems have been studied extensively, Co(cyclam) and fac-Re(bpy)$(CO)_3$Cl (Fig. 2). The mechanism of CO_2 reduction for these catalysts has been heavily investigated over the last 40 years and is still under debate. Understanding the mechanism of catalysis is highly desirable so that future catalysts can be tuned to be efficient and cost effective.

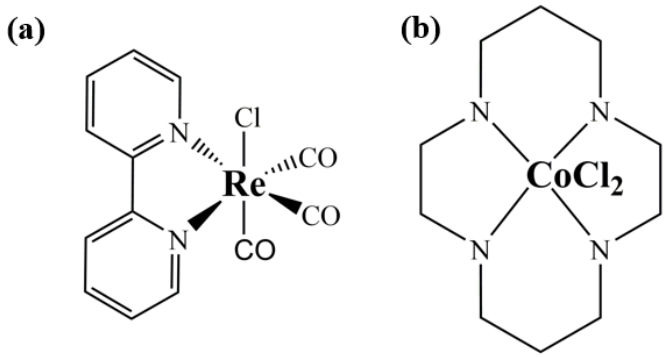

Figure 2. Parent complexes of Co(cyclam) and fac-Re(bpy)$(CO)_3$Cl.

1.2.1. Re(bpy)$(CO)_3$X complexes for catalytic CO_2 reduction

Fac-Re(bpy)$(CO)_3$X (where bpy is 2,2'-bipyridine, X is Cl or Br, all complexes discussed are fac thus will be omitted) was originally reported to be photocatalytically active for CO_2 reduction by Hawecker et al.[18-19] These molecular catalysts were found to be highly selective for CO production over H_2 and operated without a photosensitizer. TEOA was utilized as a sacrificial electron donor to reduce Re(I) to Re(0), TON's as high as 48 were achieved (TON is a measure of catalytic efficiency obtained by taking the moles of product divided by moles of catalyst, accounting for loading differences between experiments). To confirm gas phase CO_2 reduction, isotopically labeled $^{13}CO_2$ was used and researchers were able to detect the formation of ^{13}CO, supporting the photochemical reduction of CO_2.[19] It was proposed that CO_2 binds to the Re(I) catalyst through halide loss during illumination; however Re(bpy)$(^{13}CO)_3$Cl was also observed. By adding excess halide to the reaction, researchers showed decreased CO production, indicating the importance of the halide loss for CO_2 binding by inhibiting any competitive products that could bind upon formation.[19]

To help elucidate this mechanism, Meyer et al. reported the thermal or photo insertion of CO_2 into a Re-hydride (Re(bpy)$(CO)_3$H) complex formed a formato species (Re(bpy)$(CO)_3$(OCOH)).[20]

This complex was identified as an intermediate in the CO_2 reduction cycle. It was further investigated by cyclic voltammetry experiments with $Re(bpy)(CO)_3Cl$ in a CO_2 atmosphere.[21] It was proposed that there are two pathways of reduction, one-electron and two-electron (Fig. 3). The one-electron pathway involves electron injection into the bipyridine ligand and halide loss. CO_2 then binds to the Re center and is displaced by another CO_2 molecule under low potentials to form CO and carbonate (CO_3^{2-}). The two-electron pathway involves a two-electron reduction of the Re center forming $[Re(bpy)(CO)_3]^-$. This species then binds and reduces CO_2 in the presence of an oxide ion acceptor.[21]

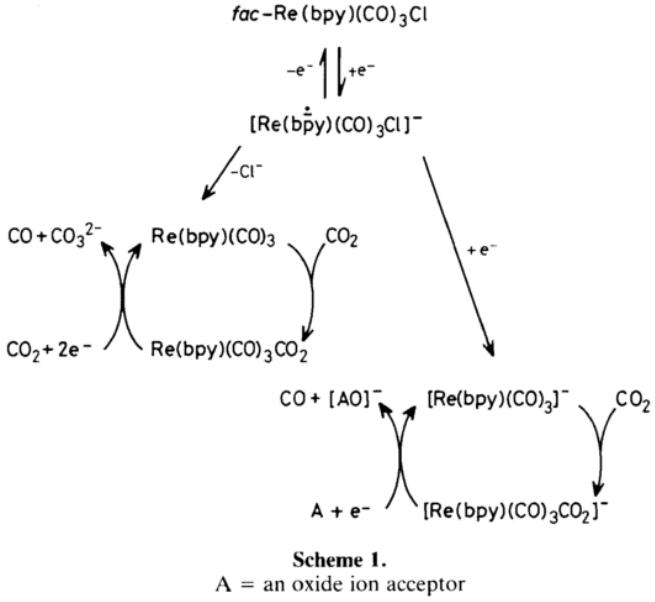

Scheme 1.
A = an oxide ion acceptor

Figure 3. Proposed one and two electron mechanisms of CO_2 reduction by Re(I)-bpy under electrochemical conditions. Reprinted with permission from Ref. 21. Copyright 1985 Royal Society of Chemistry.

These findings were further investigated by Geiger et al., where they showed TEOA reductively quenching photoexcited $Re(bpy)(CO)_3Br$ before CO_2 binding.[22] Once reduced, CO_2 rapidly binds and forms a new intermediate further supporting previous hypothesis of halide loss. This

intermediate was not identified. CO production was found to be efficient for the authors DMF/TEOA system and any addition of water hindered the reaction, indicating possible competing protonated species forming upon photoexcitation.

To probe these possible intermediate species, Johnson et al. employed infrared spectroelectrochemical studies to observe the *in situ* formation of intermediates during catalysis.[23] They confirmed the formation of CO and CO_3^{2-} spectroscopically and additionally observed formato intermediate species similar to those in previously established literature. Expanding upon this, Ishitani and co-workers supported the one-electron pathway by introducing different functionalization to the bipyridine ligand.[24] They showed CO formation in the dark was kinetically affected by functionalization and the π-back bonding between the Re and carbonyl's infrared peak shifts. Additionally, their UV-Vis studies showed that upon one-electron reduction, an electron was mainly located on the bpy ligand. Subsequent transfer of this electron to the Re center would cause the halide loss to bind CO_2.

Although these works reasonably established formate as an intermediate to the Re catalytic cycle, the exact mechanism is still debated. Fujita et al. investigated the possible role of dimeric mechanism with synthesized $[Re(dmb)(CO)_3]_2$.[25] Formation of the dimeric species *in situ* is kinetically slow and competes with CO_2 binding to reduced $Re(dmb)(CO)_3$. However, a CO_2 bridged dimer was identified indicating a possible binuclear mechanism similar to nature as previously discussed, however with varying products. This is the first literature example of an *in situ* Re dimeric species forming during CO_2 reduction in literature. Additionally, $[Re(dmb)(CO)_3]_2(OCO_2)$ and $Re(dmb)(CO)_3(OC(O)OH)$ are detected as intermediates whereas the formato species was not observed.

Agarwal et al. built upon this investigation with computational studies of dimer formation and other intermediates (Fig. 4).[26-28] CO release was calculated to be through ligand exchange rather than photodissociation. A long-lived carboxylate dimer intermediate reacts with excess CO_2 to release CO and reform the CO_2 dimer which was experimentally observed by Fujita and coworkers. The initial binding of CO_2 to the Re center is the largest energy barrier for the reaction coordinate and required for the formation of the dimer intermediate. Ishitani and coworkers showed that TEOA, a common electron donor for these systems assists CO_2 binding experimentally even in ambient conditions.[29] This lowers the energy barrier required for binding and is thus an important catalytic intermediate.

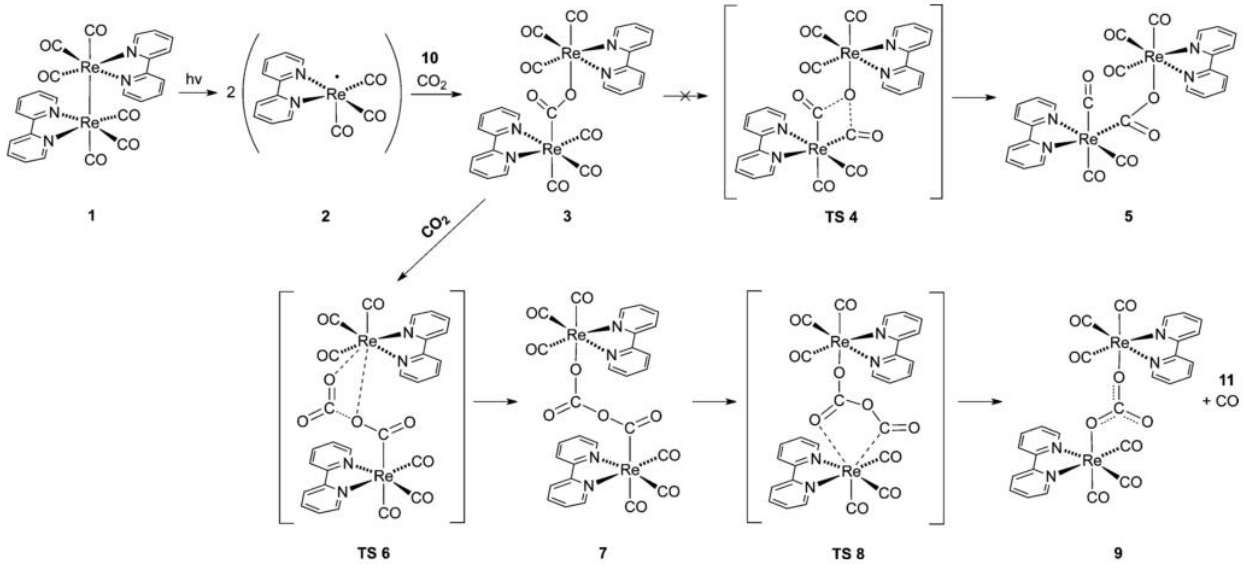

Figure 4.Proposed mechanism of CO_2 reduction for Re(I)-bpy acquired via DFT studies. A dimeric pathway is proposed where a carboxylate dimer is formed before CO_2 release. Reprinted with permission from Ref. 26. Copyright 2012 American Chemical Society.

Continued investigation of the intermediates of this mechanism were carried out by Kubiak et al. via electrochemical methods.[30-33] Building upon the parent Re complex, functionalization of the

bipyridine ring with methyl acetamidomethyl groups was performed to facilitate hydrogen bonding between two separate complexes.[31] Successful observation of a Re-Re dimer was observed via spectroelectrochemical infrared studies where CO_2 disproportionation was possible at lower overpotentials, favoring the binuclear catalytic pathway.

1.2.2. Co(cyclam) complexes for catalytic CO_2 reduction

Similar to the Re system, cobalt(II) cyclam is also capable of CO_2 reduction to CO and its catalytic mechanism has been extensively studied.[17] Electrochemical reduction of CO_2 was first performed by Fisher et al., where varying macrocycles were combined with Co and Ni metal centers.[34] CO and H_2 were both observed at varying potentials, depending on the functionalization of the macrocyclic ligand that was used. To help elucidate the mechanism, many kinetic studies of CO_2 binding in the presence of varying solvents, photosensitizers and instrumental techniques were performed. Initially, Tinnemans et al. proposed a CO_2 insertion into a Co-hydride bond, like the Re system previously discussed, forming a formato complex.[35] Fujita and coworkers explored the binding of CO_2 to Co(cyclam) under electrochemical conditions determining fast binding to form a CO_2-Co(cyclam) complex which was extremely stable.[36] A possible dimeric mechanism was also suggested where two Co complexes formed a binuclear bridge with a carboxylic acid in ACN. This complex however was only isolated as crystals and was not observed in UV-Vis studies.[37] Building upon CO_2 binding studies, various Co macrocycles were utilized in studying CO_2 reactivity in various redox potentials (Fig. 5). The CO_2 bonding coefficient strongly correlated (increased) with the a negative shift in the Co(I/II) redox couple for each complex, however it decreased with increasing steric bulk of the macrocyclic ligand.[38] CO binding was also investigated for various Co macrocycles where the binding constant of CO/CO_2 increased as reduction potentials were more negative.[39] Hydrogen bonding interactions with the N-H group on

each macrocyclic with CO_2 showed increased adduct formation. Macrocycles with bulky groups near the amine protons showed destabilization of adduct formation, indicating the importance of the amine-CO_2 interaction for binding. This was further proven via infrared spectroscopy and ^1H studies where N-H hydrogen bonding interaction with CO_2 was experimentally observed to assist in adduct formation.[40]

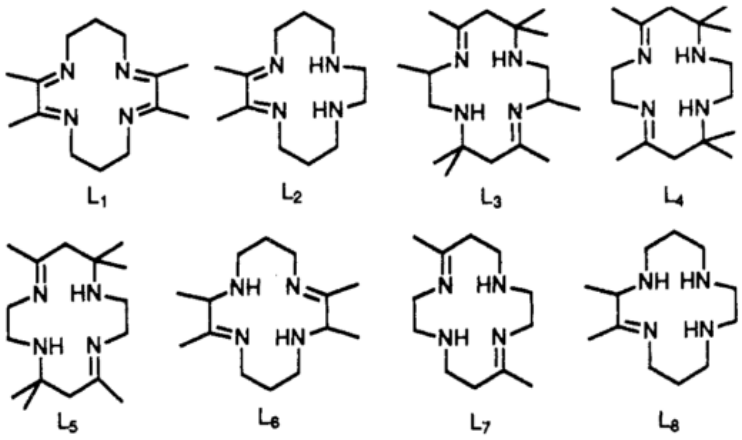

Figure 5. Macrocycles used for kinetic studies of CO_2 adduct formation with Co under electrochemical conditions. Increased methyl units are added to study steric effects upon CO_2 binding. Reprinted with permission from Ref. 38. Copyright 1990 American Chemical Society.

Photocatalytic reduction of CO_2 from Co(cyclam) was first reported by Matsuoka et al. using p-terphenyl as a photosensitizer and triethylamine (TEA) as an electron donor.[41] CO production was increased with the addition of methanol to assist in solubility of the Co complex and act as a proton donor. TEOA was utilized as an electron donor to increase the solubility of CO_2 in the acetonitrile solution. Building upon previous electrochemical work, various macrocycles were tested under the same photochemical conditions.[42] Macrocycles without sterics preventing CO_2 adduct formation showed increased CO production compared to those with organic functionalization. Sterically hindered macrocycles showed poor selectivity with an increase in H_2 production which was only

improved with the use of TEOA to assist in binding. Thus, demonstrating the importance of adduct formation and how the use of different electron donors can assist in binding based on the steric nature of the ligand.

To spectroscopically observe the intermediates of CO_2 reduction for these Co macrocyclic complexes, continuous and flash photolysis techniques were utilized.[43] Laser excitation of p-terphenyl in the presence of Co(HMD) (where H=5,7,7,12,14,14-hexamethyl-l,4,8,ll-tetraazacyclotetradeca-4,11-diene) and TEA showed direct electron transfer from p-terphenyl to Co(HMD) to form a reduced species. Upon introduction of CO_2, the species lifetime decreased due to adduct formation with Co(HMD). The spectral features of the adduct showed five and six coordinate CO_2 adducts, indicating that solvent coordinates also during catalysis.

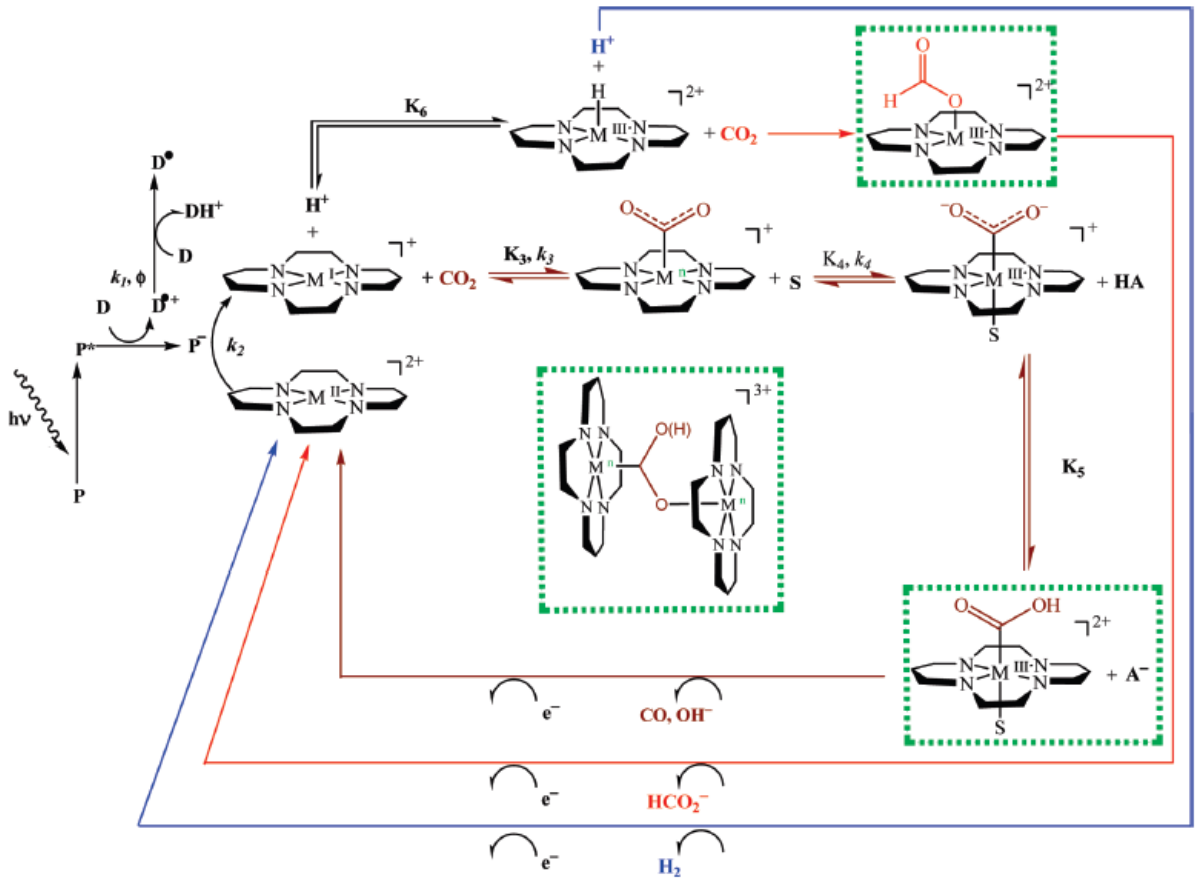

Figure 6. Proposed mechanism of CO_2 reduction with a Co(cyclam) complex. Pathways of H_2 (blue), formate (red) and CO (brown) are shown. Reprinted with permission from Ref. 17. Copyright 2009 American Chemical Society.

Mechanistically this supports the hypothesis that adduct formation is crucial to CO_2 reduction. Functionalization around the macrocyclic ring can be tuned to facilitate hydrogen bonding with the amine N-H groups to CO_2 and assist in adduct binding. Additionally, the presence of an electron donor such as TEA or TEOA can improve CO_2 solubility in solution further enhancing binding via carbamate formation. To facilitate selectivity towards CO formation, the use of a proton donor such as methanol can be used. It is also possible for CO_2 insertion into a Co hydride, however CO_2 binding is much more rapid as shown kinetically. For CO production, a binuclear complex is a possible intermediate, however was only isolated via crystals and not observed

spectroscopically *in situ*. Each of these mechanisms detailed are possible during a catalytic cycle, therefore promoting a single mechanism to maximize selectivity is a vital challenge.

1.3 Heterogeneous catalysts

Heterogeneous catalysts are solid-state catalysts that contain metals that are not ligated by organic molecules. These catalysts exist as oxides or in reduced forms such as nanoparticles or as metal-oxide nanoparticles. The most commonly studied heterogeneous catalysts include semiconducting materials, due to their practical use and wide range of advantages.[44-46] The advantages of these materials for CO_2 reduction include their robustness and recyclability. Metal oxides can withstand the harsh energy conditions of UV experiments whereas homogeneous organic catalysts can degrade. They are also crystalline solids; thus they can be easily isolated and cleaned for recyclability not requiring intense purification. Disadvantages include poor efficiency due to charge recombination. Charge recombination occurs when photoexcited electrons relax back to the conduction band and are not used by CO_2, thus decreasing efficiency. Additionally, these catalysts are difficult to derivatize and control surface structure. Any synthetic modifications to the material must be considered to saturate the surface, whereas atomic control for homogeneous systems is possible. Because of this, uniformity of the surface catalyst sites is a direct challenge to catalyst design and improvement.

Early studies of semiconductors for CO_2 reduction date back to the late 1970's where they were initially investigated for photoelectrochemical (PEC) catalysis.[47-50] A typical electrochemical cell is set up where it is irradiated by UV light and sealed under CO_2 atmosphere. The heterogeneous semiconductor acts as a photocathode where it harvests light to perform CO_2 reduction. The anode completes the other half reaction where oxidation of electron donor occurs, such as water oxidation. Both these reactions can also occur on the heterogeneous semiconductor, where instead

of a half-cell, the semiconductor is suspended in solution. Reduction of CO_2 can occur in tandem with oxidation of an electron donor, completing the catalytic cycle on single nanoparticles.

For the process of CO_2 reduction to occur, several crucial steps are required. First, photoexcitation of an electron needs to be efficient where the light energy transferred must be greater than the band gap energy. If this photoenergy is too low, photoexcitation is impossible. Once the electron-hole pair (e^- - h^+) is generated, the photoexcited electron can then be transferred either to a co-catalyst or bound CO_2 (Fig. 7). The co-catalyst is either a nanoparticle or composite structure that assists electron transfer to CO_2 to help reduce charge recombination. Once CO_2 is reduced, an electron donor is oxidized to fill the conduction band and restart the catalytic process. Eliminating charge recombination is a major challenge to this process, which has the greatest effect on catalytic efficiency.

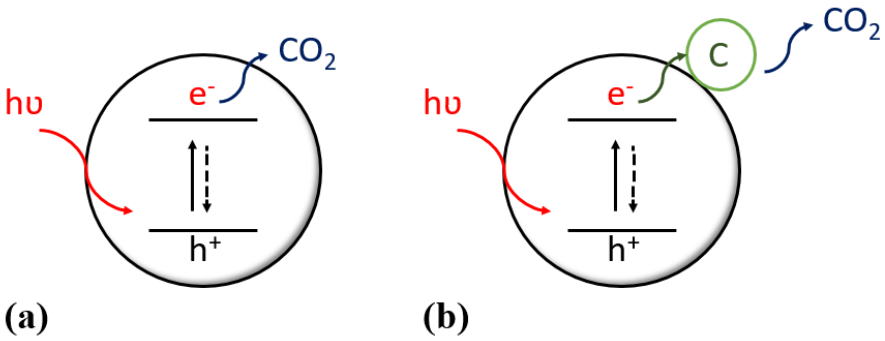

Figure 7. Schematic of electron transfer between a semiconductor (a) and CO_2. A co-catalyst can be added to assist in electron transfer (b). Dotted arrows represent electron relaxation as charge recombination.

The most common heterogeneous catalyst studied for CO_2 reduction is titanium dioxide (TiO_2).[45, 51-54] It is inexpensive, stable under harsh photocatalytic conditions, and can perform a wide variety of reactions. Water splitting[55-57], and dye degradation[58-60] are other reactions that are studied

extensively outside of CO_2 reduction. TiO_2 has three crystal structures (anatase, rutile and brookite), but a commercially available material, P25 TiO_2, has shown superior photocatalytic properties. TiO_2 also has a very large band gap of ~3.2 eV for the anatase phase. Charge recombination is the main contributor to poor efficiencies in photocatalytic CO_2 reduction. Reduction potentials for CO_2 reduction vary from -0.6 to -0.2 V so a semiconductor with a conduction band just above these potentials is ideal. This is due to the desire to have fast electron transfer between bands of similar energy levels. TiO_2 does achieve this, however since the band gap is quite large, it requires the use of UV irradiation for photoactivation.

To decrease charge recombination, there are two commonly studied methods. One of the most studied is the addition of a co-catalyst to assist in electron transfer and binding of CO_2. Also referred to as a Z-scheme system, where the co-catalyst accepts the photoexcited electron from the semiconductor material into its conduction band. Once the electron is transferred, it is very difficult for back transfer to the original conduction band. The electron can then be photoexcited within the co-catalyst to reduce CO_2. Co-catalysts can be metallic, polymeric or molecular. Polymeric and molecular co-catalysts (hybrid catalysts) will be discussed later. The other method is doping where the band gap of the semiconductor is tuned via introduction of other elements. This can often decrease the band gap energy for a material, but in turn can change product selectivity in CO_2 reduction.

A promising and well-studied co-catalyst utilized for CO_2 reduction is copper. It has been shown to reduce CO_2 to a variety of hydrocarbon products much cheaper alternative to other co-catalysts such as palladium. Additionally, the electron transfer between Cu and TiO_2 is rapid compared to playing a significant role in reducing charge recombination. Initially, Hirano and coworkers physically mixed TiO_2 and Cu powder together under photochemical conditions in water.[61] They

observed products such as methanol, formaldehyde and formic acid as products from CO_2 reduction. It was suggested that water molecules could be oxidized on TiO_2 upon photoexcitation.[61] Cu sites would be deposited to TiO_2 accepting the excited electron then react CO_2 and water to generate hydrocarbon products.[61] Adachi and co-workers expanded on this work by depositing Cu on TiO_2 to eliminate *in situ* coordination.[62] Interestingly the selectivity of products shifted where only methane and ethylene were observed. It was suggested that the coordinated Cu formed carbon radicals from CO_2 that would continue to abstract H atoms in solution.[62]

To help understand causes for the change in selectivity, Boccuzzi and co-workers prepared Cu/TiO_2 samples via wet impregnation of chemisorption hydrolysis.[63] After calcination, both samples showed widely different Cu sites where wet impregnation formed large crystallites covering the surface. Chemisorption however showed small particles dispersed on the TiO_2 surface. Infrared and temperature programmed reduction (TPR) CO adsorption studies showed that both samples had different characteristic adsorptions. Wet impregnation did not show any CO adsorptions characteristic of three-dimensional copper particles whereas chemisorption showed CO adsorbed on Cu^0 step and edge sites. These differences demonstrated the wide difference in Cu structural characteristics where surface morphology is dependent on catalyst preparation. These structural characteristics then in turn can account for changes in selectivity.

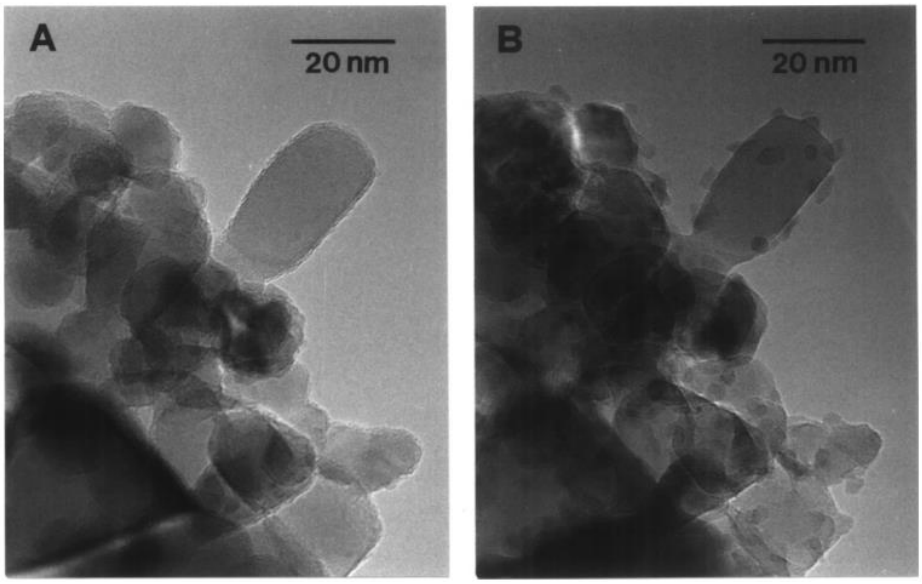

Figure 8. TEM of the chemisorption sample taken immediately (a) and after 2 min exposure to the electron beam (b). The nanoclusters of Cu are visible and are not seen for the wet impregnation method under the same conditions. Reprinted with permission from Ref. 63. Copyright 1997 Elsevier.

To study the effects of loading of Cu on the TiO_2 surface towards catalytic efficiency, Slamet and co-workers prepared varying loadings of CuO via impregnation.[64] Small uniform Cu nanoparticles were deposited on the surface, increasing in particle dispersity with lower loadings. It was shown that 3% CuO loading was the most efficient in producing methanol versus other loadings. The temperature of photocatalysis was varied where the activation energy is positive for CuO suggesting CO desorption as a limiting step. As Cu cluster sizes increase, recombination within those bulk materials also increases, limiting catalytic activity. Not only does morphology of Cu on the surface affect selectivity of products, but the loading of Cu can affect catalytic efficiency suggesting the presence of an optimum cluster size.

The role of defect sites in tandem with co-catalysts on TiO_2 for CO_2 reduction has also been investigated.[65] In particular, oxygen vacancies (V_o) have been shown to create unpaired electrons or reduced Ti centers, which can serve as reactive sites. Liu and coworkers used infrared studies

to evaluate the effect of V_o on CO_2 activation in the presence of Cu as a co-catalyst.[66] Generation of V_o on TiO_2 via H_2 treatment greatly increased photocatalytic activity additionally reducing Cu^{2+} to Cu^{1+}. The reduced Cu species was suggested to destabilize the adsorbed CO_2^- thus enhancing its conversion to CO. A major drawback of this system is the regeneration of oxygen in vacancies as the reaction proceeds, reducing long lasting catalytic activity.

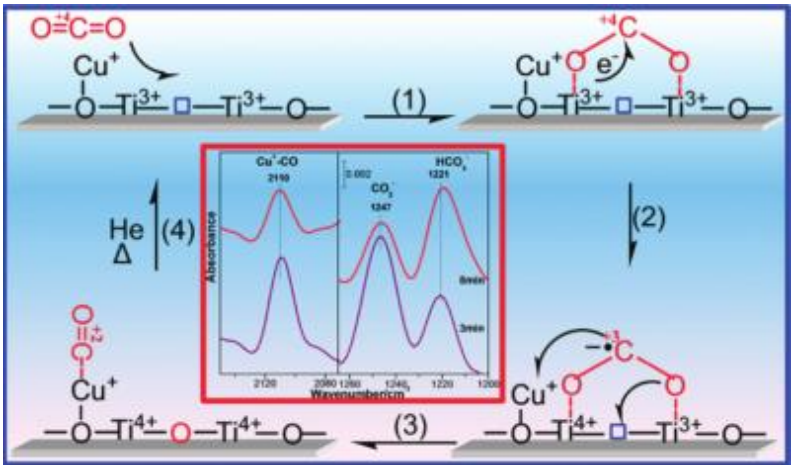

Figure 9. Schematic of CO_2 reacting with oxygen vacancies on TiO_2 and Cu sites. Reprinted with permission from Ref. 66. Copyright 2012 American Chemical Society.

Liu and co-workers continued to investigate the role of Cu for this reaction by utilizing X-ray adsorption spectroscopy (XAS).[67] XAS showed that as reactions proceeded, photoinduced oxidation of Cu occurred, decreasing activity. Additionally, heating under H_2 could not fully recover V_o or Cu back to a reduced state indicating recyclability issues with catalysts. However, addition of electron donors such as water or methanol increased the presence of Cu^+ species by acting as hole scavengers.

1.4 Hybrid catalysts

Apart from homogeneous and heterogeneous catalysts, hybrid catalysts are defined by a combination of both. Referred to as surface-immobilized catalysts, these materials are homogeneous catalysts that are covalently linked on solid-state surfaces. Other varieties include homogeneous catalysts incorporated into frameworks or porous frameworks, physisorption, or polymerization on to the surface. The advantages of such a system include the rigidity and robustness of a solid-support material, combined with the catalytic efficiency and tunability of the bound catalyst. The material is also recyclable and easily recovered post reaction. However, the major disadvantage is the lack of control on distribution of catalytic sites on the surface. Catalysts can aggregate or stack upon deposition, although diluting methods can be implemented. Additionally, characterization techniques become more limited and convoluted due to the complex nature of the deposited catalyst and the added surface interactions.

The number of studies of these catalysts has increased over the last few years, where the interest in catalytic cooperation between the catalyst and surface or effects of ligand derivatization are commonly studied.[68-70] Both variables play a major role in CO_2 reduction efficiency where simple changes in surface coordination or ligand derivatization can greatly change catalytic properties. For example, successful covalent surface attachment of $Re(bpy)(CO)_3Cl$ to mesoporous silica was achieved by Dubois and co-workers.[71] Derivatization through the bipyridine ring was used to immobilize the tricarbonyl Re(I) catalyst to SBA-15 via attachment through an amino silane group. The immobilized complex showed enhanced activity and increased stability compared to the homogeneous complex and physiosorbed analogue. Additionally, derivatization of the bipyridine ring resulted in a red shift of the catalytic complex, providing possible benefits in enhanced visible light harvesting. To further probe the effect of derivatization, Liu and coworkers compared an

electron-withdrawing amide functionalized bipyridine to an electron-donating amide in homogeneous photocatalysis (Fig. 10).[72] Both complexes showed greatly decreased activity from parent $Re(bpy)(CO)_3Cl$ demonstrating the strong influence on derivatization needed for covalent surface attachment.

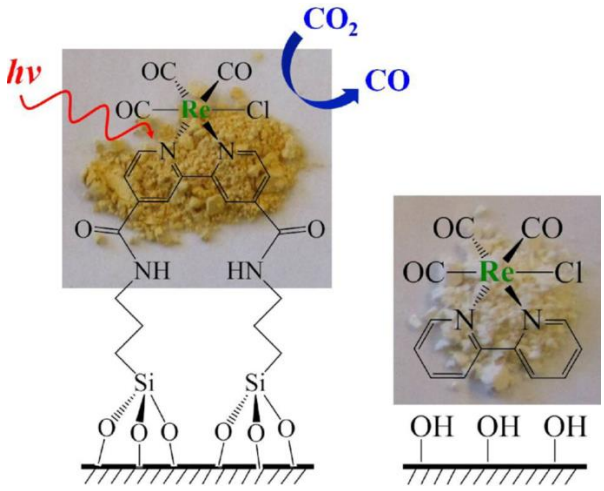

Figure 10. Structures of hybrid Re(I) and physiosorbed Re(I) catalysts. The red shift from derivatization is seen in the yellow color of the powdered material. Reprinted with permission from Ref. 71. Copyright 2012 Elsevier.

Further studies were conducted by varying the surface support that $Re(bpy)(CO)_3Cl$ was immobilized on to probe the effects of porosity on catalytic efficiency.[73] Kaolin and non-porous SiO_2 were utilized in combination with SBA-15 and were studied via DRIFTS. It was shown that as porosity of the support material increased, so did the formation of $Re(OH)(bpy)(CO)_3$. OH^- ions were able to accumulate in the increased porous environments as TEOA reacted with residual water trapped within the pores. This would facilitate the increased presence of this deactivating species for catalysts and decrease catalytic efficiency, demonstrating the importance of surface catalyst interactions.

Instead of immobilization on inert supports, immobilization on photoactive supports has also been extensively studied. These surfaces range from inorganic semiconductors, metal-organic frameworks (MOF) to periodic mesoporous organosilicas (PMO). Similar to work by Dubois and co-workers, Takeda et.al. immobilized $Re(bpy)(CO)_3Cl$ however onto a mesoporous light absorbing organosilica framework.[74] Biphenyl groups in this network absorbed UV light and were able to actively transfer this energy to the Re(I) catalyst complex. This resulted in enhancement of the photocatalytic reduction of CO_2. Additionally, the mesoporous network protected the Re(I) center from degradation under photocatalytic conditions. Further work was done by immobilizing a supramolecular Re(I)-Ru(II) photocatalyst showing enhancement under visible light conditions.[75]

Active supports like semiconductors such as TiO_2 or TaON can be used and act as a photosensitizer, transferring electrons to the active catalytic site. One example was prepared by Sekizawa and co-workers, where an Ru(II)-Ru(II) complex polymer was combined with a p-type semiconductor TaON.[76] Photocatalytic conversion of CO_2 to HCOOH was achieved utilizing methanol as an electron donor and proton source. As photoexcitation occurred in CO_2, a photogenerated hole was generated in the polymer hybrid which led to efficient electron transfer even under visible light. Additionally, both these steps prevented charge recombination within each material achieving a TON of 41.

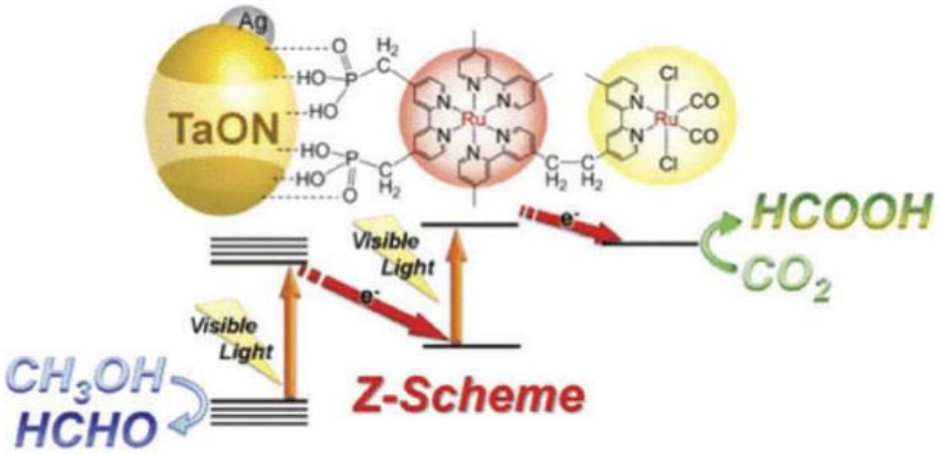

Figure 11. Schematic of Ru supramolecular hybrid catalyst with TaON. Methanol is oxidized whereas CO_2 is reduced to formic acid. Reprinted with permission from Ref. 76. Copyright 2013 American Chemical Society.

As previously discussed, utilization of water as an electron donor is highly desirable in mimicking photosynthesis. Sato and co-workers coupled a water oxidation catalyst, TiO_2 with Ru(II) polymerized on InP for photoreduction.[77] InP was chosen as an anchor due to its better charge transfer with the Ru(II) catalyst. The hybrid complex was able to achieve excellent selectivity of CO_2 reduction to formate and was improved by introduction of $SrTiO_3$ photoanode instead of TiO_2.[78] This was due to the larger band gap energy difference between $SrTiO_3$ and InP, preventing recombination.

More recently, Kuriki and co-workers developed an extremely efficient visible light photocatalyst that achieved a TON of over 1000.[79] Ru(II)bipyridine catalysts were functionalized with different anchoring groups and deposited on carbon nitride (C_3N_4). The electron transfer from the C_3N_4 support to Ru is highly efficient, where Ru(II) derivatized with phosphate linkers was the most efficient due to covalent attachment to the C_3N_4 surface. Other complexes that were not derivatized or methylated are unable to covalently attach to C_3N_4, thus electron transfer was greatly decreased.

A selectivity of 80% was achieved for formic acid where CO and H_2 were other byproducts. At the time of publication, it was the most efficient hybrid catalyst reported in literature.

II. PHOTOCHEMICAL REDUCTION OF CO_2 USING RHENIUM CATALYSTS

2.1 Effect of ligand substitution on photochemical proprieties of hybrid Re(I) complexes

2.1.1 Introduction

Homogeneous catalysts have been previously studied extensively for their catalytic properties in CO_2 reduction. One class of these catalysts are bipyridine complexes which contain Ru, Mn, and Re metal centers.[80] In particular, the Re(I) catalysts have been studied extensively for their electrochemical reduction of CO_2 since the 1980's.[20-21, 81] They show good selectivity for CO production versus H_2 or formic acid, which is desirable since CO is a precursor to many solar fuels. One disadvantage is their instability in photochemical conditions. High energy ultraviolet irradiation causes catalyst degradation to an oxidized form decreasing TON efficiencies. To overcome this issue, Dubois and coworkers developed a hybrid catalyst by attaching molecular catalysts to solid-state surfaces through covalent attachment.[71] Additionally, further hybrid catalysts have been synthesized via polymerization on surfaces and intercalation into porous frameworks.[74-75, 82-83] It was demonstrated that these hybrid systems had enhanced stability under photochemical conditions and enhanced reactivity.

Previously, Re(I) bipyridine complexes were attached through the 4,4' position of the aromatic ring.[71-72] Single chain amines were used as an anchor to the mesoporous silica surface through a substitution reaction with an acylated bipyridine ligand forming an amide. The Re(I) was then coordinated to the surface bound bpy ligand to give the hybrid complex. However, steric hindrance from the 4,4' ligand substitution as well as surface concentration of amine anchors prevent close

proximity of these catalytic sites to each other. This hinders the ability to study a possible binuclear mechanism for the cooperative reduction of CO_2 to CO.

Building upon previous work, 5,5'-dicarboxylic acid-2,2'-bipyridine was implemented as a ligand, shifting the binding site to the surface by one carbon. This ligand has previously been used in literature in supramolecular catalysts as well as a building block for metal-organic frameworks (MOF). By shifting the derivatization, the steric hindrance between two sites will be reduced upon covalent attachment. One ligand will bind to one amine anchor covalently immobilized on the surface, where the 5,5' substitution prevents covalent attachment to two surface anchors. The effect of substitution was also studied to observe how the 5,5' positions affect the photochemical properties versus the previously studied 4,4' position. A dipodal linker (two amine anchors covalently bound) was also studied to ensure proximity between two anchoring sites. Previously used monopodal linkages are dependent on surface concentration to ensure proximity between catalytic sites. By having two anchoring sites covalently bounded to each other, this eliminates concentration dependence, further promoting optimal geometry between two sites.

To observe the possible binuclear mechanism, spectroscopic techniques such as DRIFTS were implemented to observe adducts on the surface-bound Re(I) center by monitoring carbonyl shifts through *in situ* photocatalysis. Change in derivitization showed an increased presence of a formyl species upon infrared studies for the 5,5' ligand versus the 4,4'. Photocatalytic efficiency for CO_2 reduction was also studied with and without a photosensitizer $Ru(bpy)_3^{2+}$. Photocatalysis results showed the 4,4' ligand derivitization increased TON versus the 5,5' ligand derivitization whereas the monopodal versus dipodal linkage was dependent on the derivitization. This demonstrates the importance of the ligand derivatization on the photochemical properties of the Re(I) catalyst as well as the effect of the surface linker.

2.1.2 Experimental

a. Materials

All chemicals were used as received without any further purification. Poly(ethylene glycol)-block-poly(propylene glycol)-block-polyethylene glycol) (Pluronic P-123), tetraethyl orthosilicate (TEOS), hydrochloric acid, triethylamine (TEA), triethanolamine (TEOA), toluene, diethyl ether, dichloromethane (DCM), dimethylformamide (DMF), thionyl chloride, pentacarbonyl chlororhenium (I) (98%), tris(2,2'-bipyridine) dichlororuthenium(II) hexahydrate (99%, denoted "$Ru(bpy)_3^{2+}$") were obtained from Sigma-Aldrich. Aminopropyltrimethoxysilane (APTMS), N,N-bis[3-(trimethoxysilyl)propyl]ethylenediamine (EDTMS) were obtained from Gelest. 2,2'-bipyridine-4,4'-dicarboxylic acid, 2,2'-bipyridine-5,5'-dicarboxylic acid were obtained from TCI America.

b. Synthesis

Synthesis of Mesoporous Silica (SBA-15)

Mesoporous silica was synthesized according to methods by Zhao and coworkers.[84] Initially, 2 g of Pluronic P-123 was placed in 15 mL milli Q water to which 60 mL of 2 M HCl solution was added while stirring. The solution was stirred for 2-3 hours until all P-123 was dissolved. Then 4.61 mL of TEOS was added and the solution was heated to 70^{o}C and stirred for 24 hours. The white solution was then transferred to an autoclave and heated to 100^{o}C for 24 hours without agitation. A white precipitate was gravity filtered while washing with milli Q water until a neutral pH was obtained and dried. The dried powder was then calcined at 550^{o}C for 8 hours under O_2 flow.

Synthesis of APTMS Functionalized SBA-15

100 mg of SBA-15 was dried at 100ºC for 2 hours before being dispersed in 50 mL dry toluene under inert atmosphere. 75 µL of APTMS was added and the solution was stirred for 48 hours under nitrogen atmosphere at room temperature. The product was recovered via centrifugation and washed each three times with toluene, diethyl ether and DCM respectively. The resulting white powder was then dried under vacuum.

Synthesis of EDTMS Functionalized SBA-15

100 mg of SBA-15 was dried at 100ºC for 2 hours before being dispersed in 50 mL dry toluene under inert atmosphere. 75 µL of EDTMS was added and the solution was stirred for 48 hours under nitrogen atmosphere at room temperature. The product was recovered via centrifugation and washed three times with toluene, diethyl ether and DCM respectively. The resulting white powder was then dried under vacuum.

Synthesis of 4,4'-Acylated Bipyridines

In a typical synthesis, 25 mg of 4,4'-dicarboxylic-2,2'-bipyridine was dispersed in 15 mL of thionyl chloride. This solution was heated to 85ºC under inert atmosphere and refluxed overnight. Rotary evaporation was used to isolate the acylated yellow product.

Synthesis of 5,5'-Acylated Bipyridines

In a typical synthesis, 25 mg of 5,5'-dicarboxylic-2,2'-bipyridine was dispersed in 15 mL of thionyl chloride. This solution was heated to 85ºC under inert atmosphere and refluxed overnight. Rotary evaporation was used to isolate the acylated yellow product.

Synthesis of 4,4'-bipyridine-APTMS Functionalized SBA-15

100 mg of APTMS functionalized SBA-15 was dispersed in 40 mL DCM under N_2 flow. Then, freshly synthesized 4,4'-dichloro-2,2'-bipyridine was then dispersed in 15 mL DCM and added

dropwise to the stirring silica solution under continued N_2 flow. The solution was then heated to 70^{o}C and stirred overnight. The product was retrieved via centrifugation and washed three times each with DCM, diethyl ether and repeated DCM respectively. A yellow powder was isolated via drying under vacuum.

Synthesis of 5,5'-bipyridine-APTMS Functionalized SBA-15

100 mg of APTMS functionalized SBA-15 was dispersed in 40 mL DCM under N_2 flow. Then, freshly synthesized 5,5'-dichloro-2,2'-bipyridine was then dispersed in 15 mL DCM and added dropwise to the stirring silica solution under continued N_2 flow. The solution was then heated to 70^{o}C and stirred overnight. The product was retrieved via centrifugation and washed three times each with DCM, diethyl ether and repeated DCM respectively. A yellow powder was isolated via drying under vacuum.

Synthesis of 4,4'-bipyridine-EDTMS Functionalized SBA-15

100 mg of EDTMS functionalized SBA-15 was dispersed in 40 mL DCM under N_2 flow. Then, freshly synthesized 4,4'-dichloro-2,2'-bipyridine was then dispersed in 15 mL DCM and added dropwise to the stirring silica solution under continued N_2 flow. The solution was then heated to 70^{o}C and stirred overnight. The product was retrieved via centrifugation and washed three times each with DCM, diethyl ether and repeated DCM respectively. A yellow powder was isolated via drying under vacuum.

Synthesis of 5,5'-bipyridine-EDTMS Functionalized SBA-15

100 mg of EDTMS functionalized SBA-15 was dispersed in 40 mL DCM under N_2 flow. Then, freshly synthesized 5,5'-dichloro-2,2'-bipyridine was then dispersed in 15 mL DCM and added

dropwise to the stirring silica solution under continued N_2 flow. The solution was then heated to 70^{o}C and stirred overnight. The product was retrieved via centrifugation and washed three times with DCM, diethyl ether and DCM again respectively. A yellow powder was isolated via drying under vacuum.

Synthesis of $Re(CO)_3Cl$-4,4'-bipyridine-APTMS Functionalized SBA-15 (Re-A4-SBA-15)

100 mg of 4,4'-bipyridine-APTMS functionalized SBA-15 was dispersed in 50 mL dry toluene. 50 mg of pentacarbonyl chlororhenium(I) was added to the solution under stirring. The solution was then heated to 95^{o}C under inert atmosphere and was stirred overnight while covered with foil to reduce light exposure. The product was then retrieved via centrifugation and washed three times each with toulene, diethyl ether and repeated DCM respectively. A yellow powder was isolated and dried under vacuum.

Synthesis of $Re(CO)_3Cl$-5,5'-bipyridine-APTMS Functionalized SBA-15 (Re-A5-SBA-15)

100 mg of 5,5'-bipyridine-APTMS functionalized SBA-15 was dispersed in 50 mL dry toluene. 50 mg of pentacarbonyl chlororhenium(I) was added to the solution under stirring. The solution was then heated to 95^{o}C under inert atmosphere and was stirred overnight while covered with foil to reduce light exposure. The product was then retrieved via centrifugation and washed three times with toulene, diethyl ether and DCM again respectively. A yellow powder was isolated and dried under vacuum.

Synthesis of $Re(CO)_3Cl$-4,4'-bipyridine-EDTMS Functionalized SBA-15 (Re-D4-SBA-15)

100 mg of 4,4'-bipyridine-EDTMS functionalized SBA-15 was dispersed in 50 mL dry toluene. 50 mg of pentacarbonyl chlororhenium(I) was added to the solution under stirring. The solution

was then heated to 95°C under inert atmosphere and was stirred overnight while covered with foil to reduce light exposure. The product was then retrieved via centrifugation and washed three times with toulene, diethyl ether and DCM again respectively. A yellow powder was isolated and dried under vacuum.

Synthesis of $Re(CO)_3Cl$-5,5'-bipyridine-EDTMS Functionalized SBA-15 (Re-D5-SBA-15)

100 mg of 5,5'-bipyridine-EDTMS functionalized SBA-15 was dispersed in 50 mL dry toluene. 50 mg of pentacarbonyl chlororhenium(I) was added to the solution under stirring. The solution was then heated to 95°C under inert atmosphere and was stirred overnight while covered with foil to reduce light exposure. The product was then retrieved via centrifugation and washed three times with toulene, diethyl ether and DCM again respectively. A yellow powder was isolated and dried under vacuum.

c. Characterization

Optical spectra of hybrid silica samples were obtained using a Cary 50 Bio spectrophotometer outfitted with a Barrelino diffuse reflectance probe (for powder samples) and a transmission cell (for homogeneous solutions). Diffuse reflectance infrared Fourier-transform spectroscopy (DRIFTS) were collected on a Nicolet 6700 FTIR spectrometer equipped with a Harrick Praying Mantis diffuse reflectance accessory. Elemental analysis of the synthesized hybrid photocatalysts was performed via acid digestion utilizing a Varian Vista AX inductively coupled plasma atomic emission spectrometer. EPR spectra were collected on an X-band (9.5 GHz) Bruker ELEXSYS E-500 cw-EPR/ENDOR spectrometer at room temperature.

d. Photocatalytic Testing

For a typical photocatalytic CO_2 reduction test, 10 mg of sample was dispersed in 4 mL of a 3:1 DMF:TEOA solution in a quartz test tube with a mini stir bar. The sample tube was sealed with a septum and parafilm, then bubbled with CO_2 (99.999% Airgas) for 30 minutes in dark. Once bubbling was completed, the sample was irradiated with a 300-W Xe Arc lamp with an attached water filter and an AM 1.5 optical filter. The light intensity was fixed at 30 mW/cm^2. While the reaction solution was stirred under light, the head space was sampled using a gas tight syringe for analysis using an Agilent 7820 GC equipped with a Thermal Conductivity Detector (TCD) and a 60/80 Carboxen 1000 column.

2.1.3 Results and Discussion

For this study, the substitution of the bipyridine ring was studied at both at the 4,4' and 5,5' position to observe any electronic effects caused by the change in substitution. Additionally, by using a dipodal surface linker with two available sites to react with the acylated bipyridine, close proximity between two rhenium sites is possible without being concentration dependent. Previously, proximity was only determined by surface concentration of monopodal sites and would largely be hindered by sterics through covalent attachment of the 4,4' position of the bipyridine.[71-72] By having covalent attachment through the 5,5' position, it is possible that two metal sites can bind to the same linker, thus elimanting the steric issue and forcing proximity. Another advantage is through a single-arm attachment due to the substitution preventing a two-arm attachment. This adds to the overall flexibility of the catalyst on the surface, further enhancing the probability of cooperative catalysis.

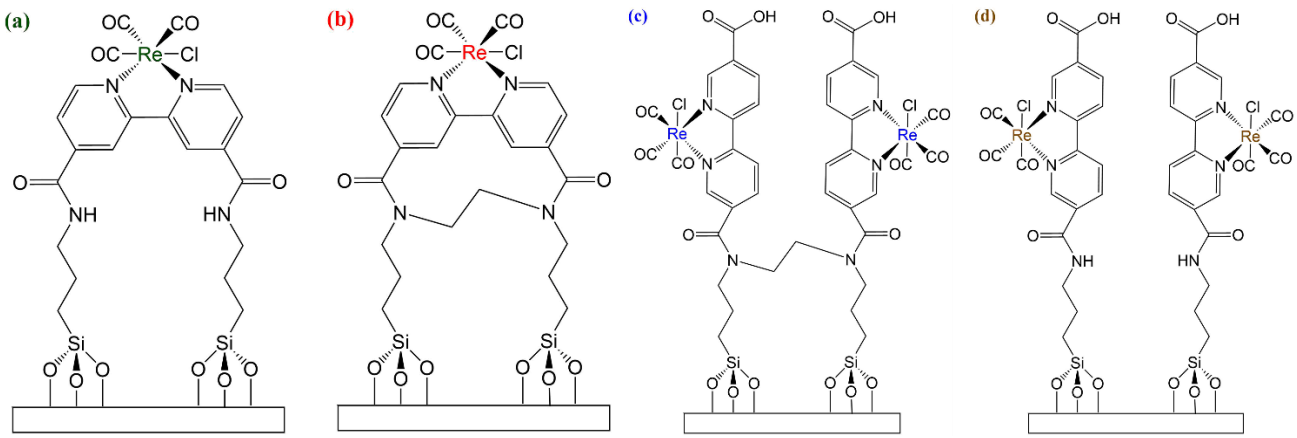

Figure 12. Structures for monopodal and dipodal Re(I) complexes with both 4,4' and 5,5' bipyridine configurations. a) Re-A4-SBA-15 b) Re-D4-SBA-15 c) Re-D5-SBA-15 d) Re-A5-SBA-15

To evaluate the amount of Re covalently bound to the surface for these hybrid catalysts, elemental analysis was performed via inductively coupled plasma – atomic absorption spectroscopy (ICP-AES). An interesting trend was found as hybrid catalysts utilizing the 5,5' substitution on the bipyridine, the loading of Re was substantially higher than samples utilizing the 4,4' substitution. Re-D5-SBA-15 and Re-A5-SBA-15 had loadings of 2.969 and 2.717 µmol/10mg respectively and Re-D4-SBA-15 and Re-A4-SBA-15 had loadings of 0.818 and 0.628 µmol/10mg respectively. It is not immediately clear as to why this trend occurs; however one factor could be the differing orientation resulting in the change in substitution. 5,5' substituted bipyridines are likely to bind perpendicular to surface amines due to sterics, thus binding to one NH surface group. 4,4' substitution likely binds to two NH surface groups upon amide formation, thus suggesting the complex lies parallel to the surface. This steric hinderance could inhibit ligand loading to the surface, and further supports the hypothesis of the 5,5' substituted bipyridine "standing up" while bound to the surface amine sites, promoting close proximity.

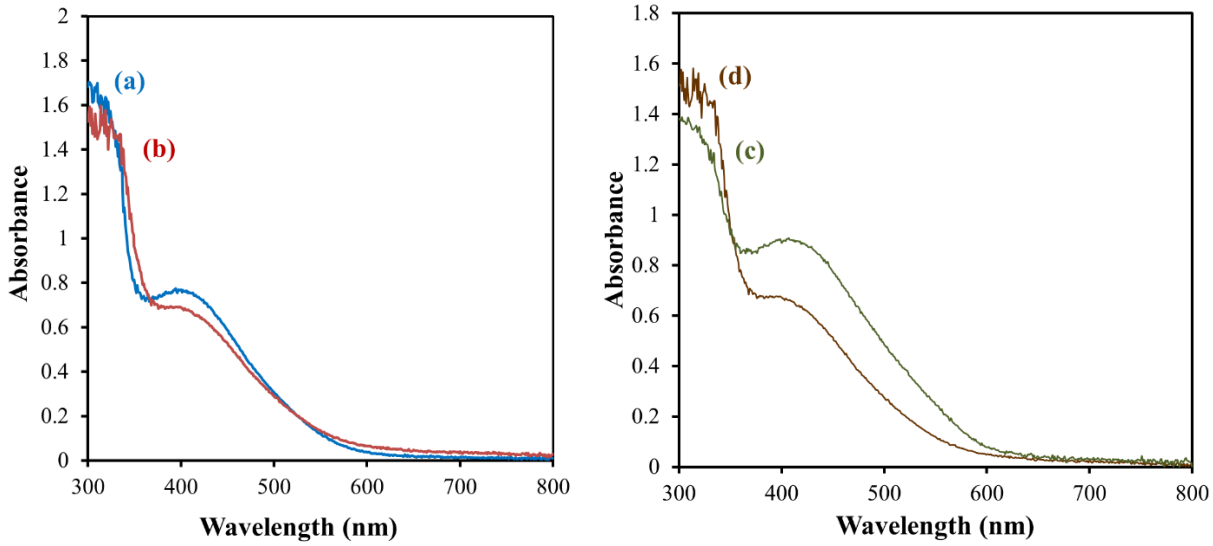

Figure 13. Diffuse reflectance UV-visible spectra (DRUV) of Re-D4-SBA-15 (a), Re-D5-SBA-15 (b), Re-A4-SBA-15 (c), and Re-A5-SBA-15 (d) in powder form. Barium sulfate was used as the background.

To evaluate the integrity of the Re system on the surface of the silica support in comparison with previous homogeneous studied derivatives, a variety of spectroscopic characterization techniques are utilized. Such techniques include diffuse reflectance UV-visible probe and infrared spectroscopy. For all four samples studied, they exhibit a absorption band around 410 nm (Fig. 13). This represents the metal-to-ligand charge transfer (MLCT) between the Re center and the bipyridine ligand.[72] Comparing to the homogeneous parent compound of $Re(bpy)(CO)_3Cl$ which has a MLCT at 370 nm, there is a significant shift. This 30-40 nm shift is a result of derivatization of the bpy ligand with electron-withdrawing amide groups, demonstrating the effect of derivitization towards the MLCT band.

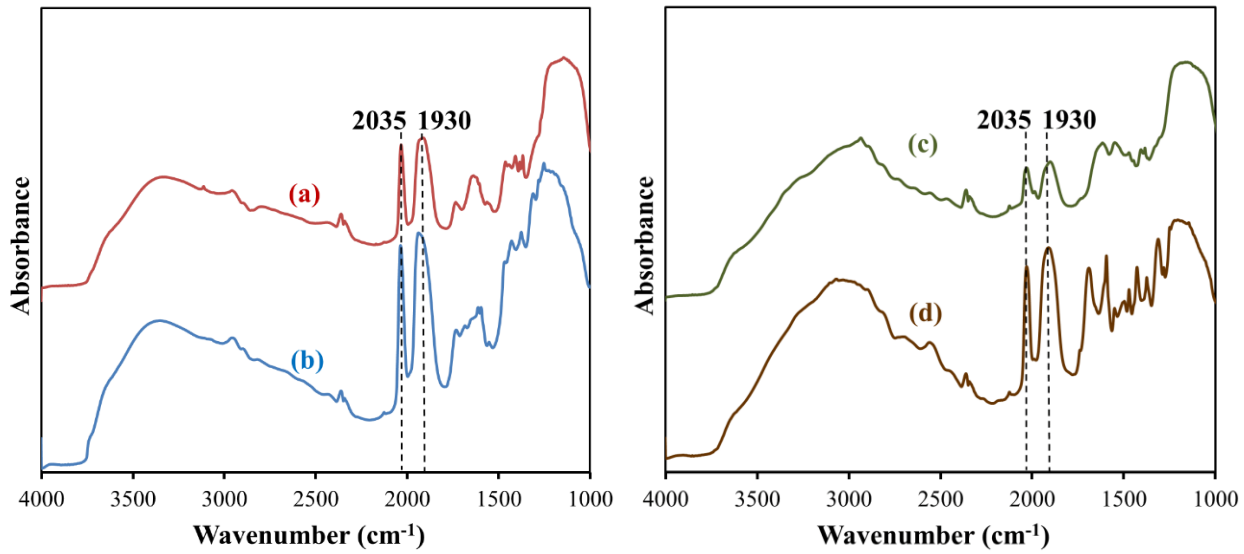

Figure 14. DRIFTS spectra of Re-D4-SBA-15 (a), Re-D5-SBA-15 (b), Re-A4-SBA-15 (c), and Re-A5-SBA-15 (d) in powder form. KBr was mixed with each sample and served as the background.

Fig. 14 shows DRIFTS spectra all four samples mixed with KBr as a background. Intense Re(I)-carbonyl bands can be seen at 2035 cm^{-1} and 1930 cm^{-1} for all spectra as well as other absorptions that are not labeled. These carbonyl bands are similar to other previously studied DRIFTS spectra that have been reported indicating that diimine-tricarbonyl Re(I) units are present in all samples.[71-73] However, it can be seen in Re-A4-SBA-15 sample two small additional bands at 2104 cm^{-1} and 1979 cm^{-1}. These carbonyl bands represent physiosorbed pentacarbonylchlororhenium(I) that did not react with surface bound bipyridine ligands. All samples are thoroughly washed with solvent to remove any physiosorbed Re, however it was not successful for this A4 sample. This can act as a contamination for CO_2 reduction studies and can alter CO production results. For the rest of this chapter, the focus will be on the Re-D4-SBA-15 and Re-D5-SBA-15 for this reason. Additionally, the monopodal linkers have been thoroughly investigated previously and thus are not of interest for this investigation.

The synthesized dipodal hybrid catalysts were tested in photocatalysis in the presence of CO_2 and TEOA as a sacrificial electron donor. For these conditions, CO was observed as the primary product from CO_2 reduction and no significant formation of formic acid and H_2 was observed (Fig. 15). Turnover numbers of CO production were obtained as 12.7 and 8.8 for Re-D4-SBA-15 and Re-D5-SBA-15 respectively where $Ru(bpy)_3^{2+}$ was utilized as a photosensitizer (Fig. 15). Without photosensitizer present, the amount of CO produced was considerably low compared to previously studied hybrid catalysts. This can be attributed to the lower light intensity utilized in this study which is 30 mW/cm^2 versus 100 mW/cm^2 used previously.

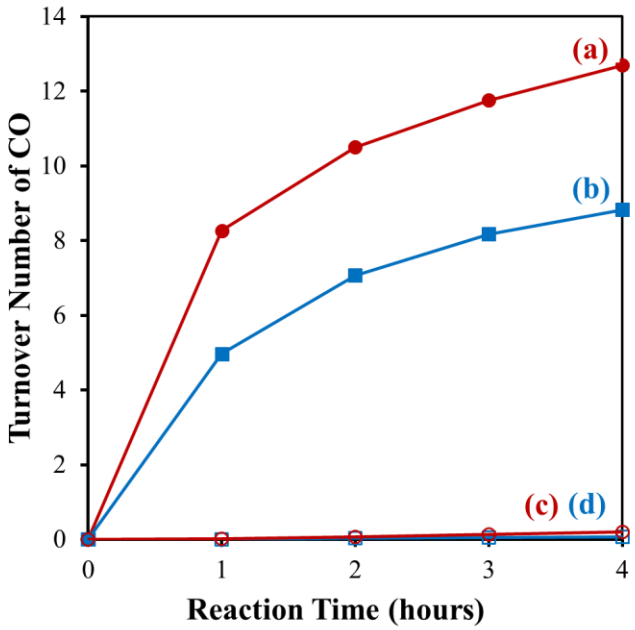

Figure 15. CO production in photocatalytic CO_2 reduction using Re-D4-SBA-15 (a,c) and Re-D5-SBA-15 (b,d) under simulated solar irradiation. In testing, $Ru(bpy)_3^{2+}$ (a,b) was used as a photosensitizer. Light intensity was 30 mW/cm^2 for all photocatalytic testing.

Upon performing photocatalysis testing of the dipodal samples in the absence of the $Ru(bpy)_3^{2+}$ photosensitizer however, a surprising phenomenon was observed. When light irradiation was

initiated, the reaction solution containing Re-D5-SBA-15 quickly changed color from yellow to bright green (Fig. 16). Usually for all previously studied Re(I) samples, the initial color is yellow and remains yellow over time, sometimes changing to orange in later experiments due to catalyst or solvent degradation. This green color had not been observed previously, and remained at room temperature, slowly decaying back to yellow once the light had been turned off.

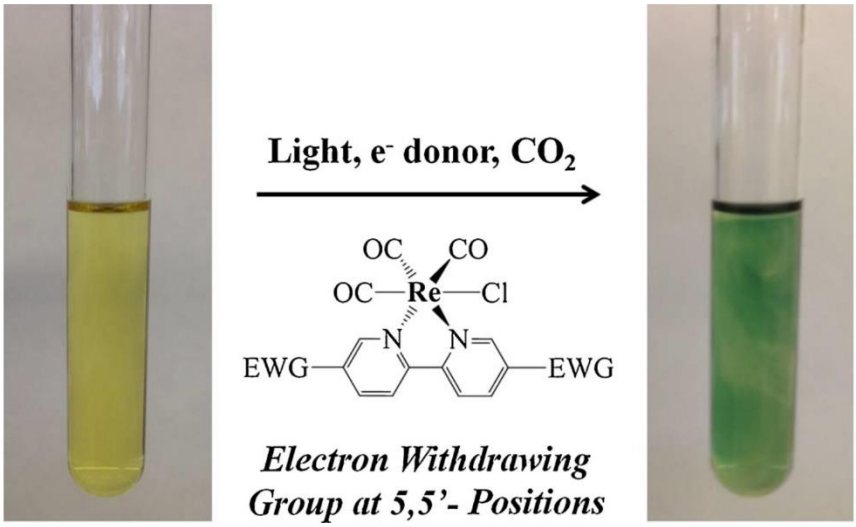

Figure 16. Color change observed while irradiating Re-D5-SBA-15 with light and the given conditions needed.

Control experiments revealed that for color change of the photocatalyst, amine electron donor (TEOA), CO_2 and light irradiation were all necessary. When exposed to ambient air, the color immediately changed back to yellow. This was not observed for the Re-D4-SBA-15 sample which always remained yellow upon light irradiation.

Spectroscopic analysis via transmission UV-Vis spectroscopy was performed to investigate this phenomenon. In a typical setup, about 1 mL of photocatalytic reaction mixture was added to a quartz cuvette and sealed with a septa and parafilm. This was then gently purged with CO_2 for 20

min and irradiated under UV light for 5 min. The decay of color was then measured over time in dark within the UV-Vis spectrometer.

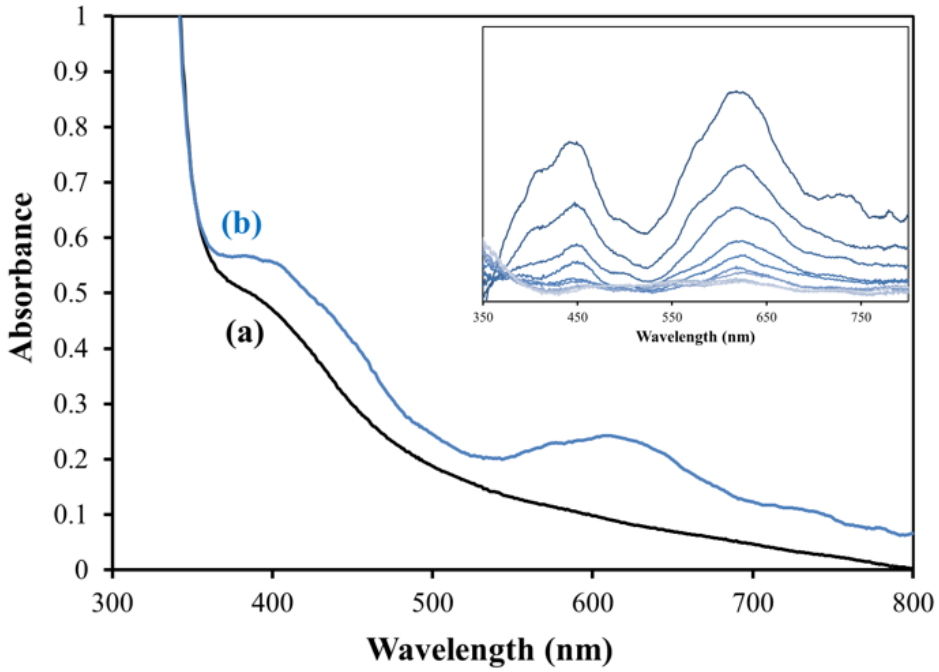

Figure 17. Transmission UV-Vis of a solution containing Re-D5-SBA-15, TEOA and CO_2 before (a, black line) and after (b, blue line) light irradiation for 5 min. Additional spectra were collected every 15 min after the light was turned off to obtain difference spectra (inset) which demonstrates the decay of the green color in dark.

Upon irradiation of Re-D5-SBA-15, two bands at 620 nm and 450 nm appear and are associated with the green color formed upon light exposure. From the inset in figure 17, it is apparent that once in dark these two bands gradually decay back to the initial trace. This experiment was repeated with Re-D4-SBA-15 which did not show either band upon light irradiation (Fig.18). Subtraction spectra further supported the lack of the two bands associated with the green color.

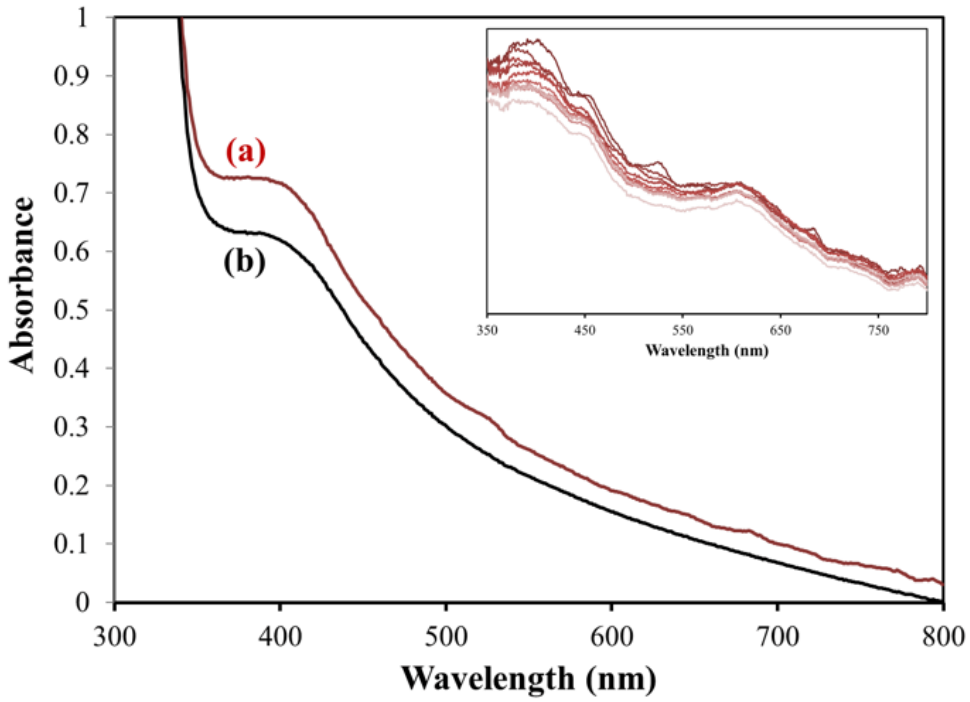

Figure 18. Transmission UV-Vis of a solution containing Re-D4-SBA-15, TEOA and CO_2 before (a, black line) and after (b, red line) light irradiation for 5 min. Inset spectra were collected similar to Re-D5-SBA-15.

To help probe this mechanism, homogeneous samples of derivatized Re(I) compounds, $Re(CO)_3Cl$-5,5'-dicarboxylic-2,2'-bipyridine (Re-5) and $Re(CO)_3Cl$-4,4'-dicarboxylic-2,2'-bipyridine (Re-4) were synthesized and tested in the same transmission UV-Vis experiment. The use of homogeneous compounds was to eliminate the presence of the mesoporous silica as a support, which can cause light scattering during a transmission experiment. Similar to the hybrid material, Re-5 immediately turned green and showed two broad peaks around 450 nm and 620 nm after exposure to light while the intensity of the MLCT around 400 nm decreased significantly (Fig. 19). Re-4 remained yellow in color after light irradiation and only showed complete disappearance of the MLCT band around 400 nm. This disappearance is attributed to the formation of the one-electron reduced Re species upon light exposure.

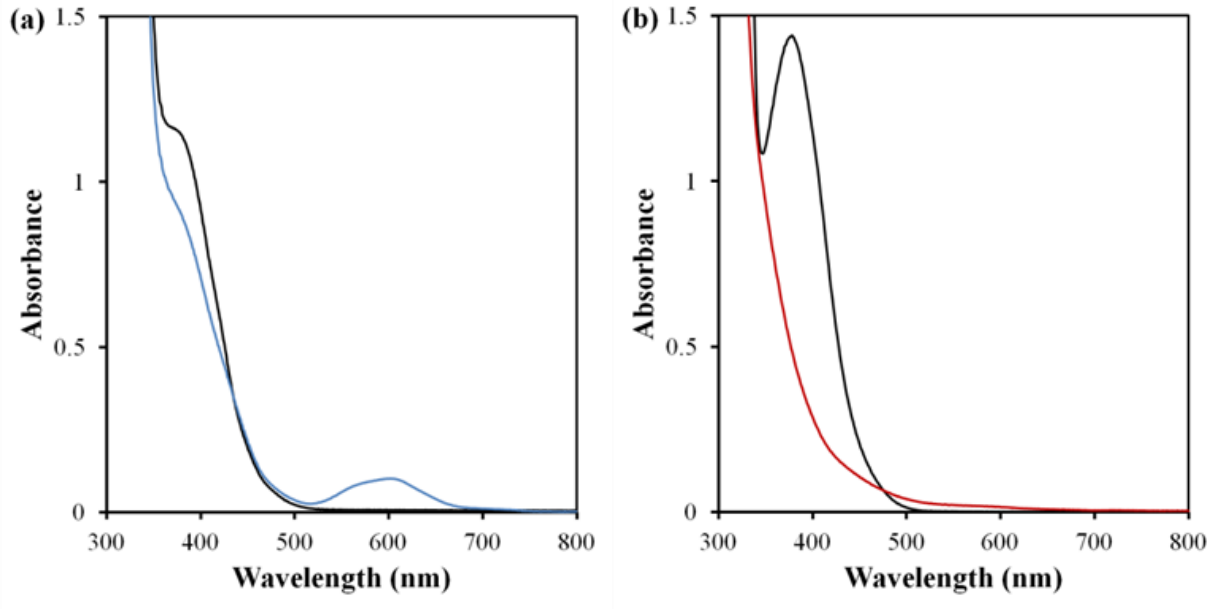

Figure 19. Transmission UV-Vis of Re-5 (a) and Re-4 (b) in the presence of TEOA and CO_2 after light irradiation. Spectra before light irradiation are included (black lines). Re(I) catalyst concentration was 0.45 mM for both samples.

Compiling the transmission UV-Vis results for both the hybrid and homogeneous Re(I) samples, they clearly demonstrate that derivatization of the bipyridine ligand influences the photochemical properties of the catalyst. For a typical parent Re(I) complex, photoexcitation leads to a reduced species where the MLCT is reductively quenched by an electron donor (TEOA). Then Cl^- dissociates and CO_2 binds to this vacated site which undergoes further reduction. Ishitani and coworkers demonstrated that a CO_2-bound adduct with TEOA forms on Re which acts as the active species of CO_2 reduction. This demonstrates the importance of CO_2 binding for photocatalysis.[29] The green color observed for Re-D5-SBA-15 is likely a variation of electron density in the CO_2 bound Re(I) adduct versus the 4,4' substituted system. The difference is likely electron density is localized on the bipyridine ligand for the 5,5' substitution and on the Re(I) center for the 4,4' substitution. This difference is solely based on the change of substitution of electron withdrawing carboxylic acid or amide groups. By having the electron withdrawing groups in the 5,5'

substitution, electron density is “pulled” into the bipyridine ligand, whereas 4,4’ substitution does not have this effect.

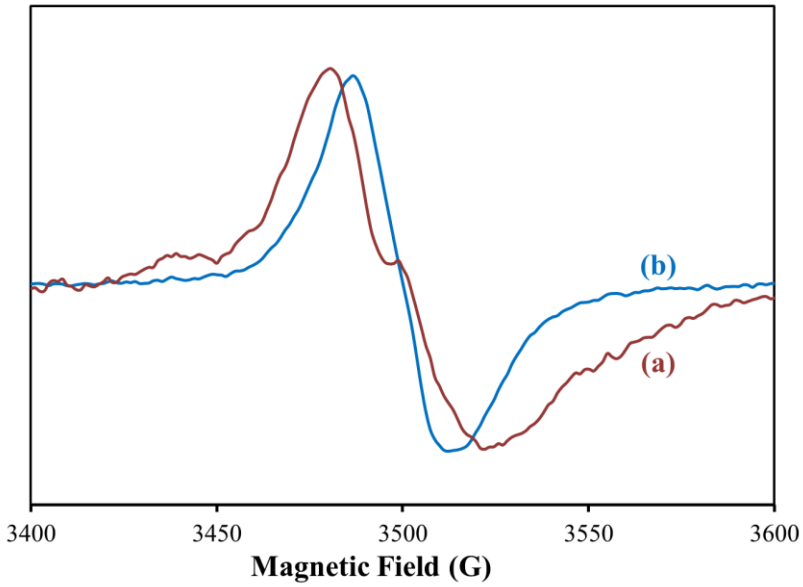

Figure 20. Room temperature EPR spectra of Re-D4-SBA-15 (a) and Re-D5-SBA-15 (b) under light irradiation. Powder samples used were mixed with KBr and TEOA and purged with CO_2 prior to light irradiation.

To help further probe electron localization for these complexes, room temperature EPR spectroscopy was employed. Typically, a small amount of catalyst was mixed with KBr and TEOA which was then purged with CO_2 and sealed to maintain CO_2 atmosphere during measurements. Figure 20 shows both Re-D4-SBA-15 and Re-D5-SBA-15 spectra under constant light irradiation. Both samples show a broad resonance centered at g = 2, which increases in intensity with further light irradiation. Without irradiation no signal was detected. This peak represents the paramagnetic one-electron reduced Re(I) species formed in the presence of an electron donor and CO_2. The stabilization and increasing intensity of this peak suggests the importance of CO_2 binding to help stabilize this one-electron reduced species.

Focusing on the Re-D4-SBA-15 trace (Fig. 20a), it shows resonance features from hyperfine interactions between the unpaired electrons within the Re(I) nuclei which has been previously seen in hybrid Re(I) studies.[72] These interactions however are not seen in the Re-D5-SBA-15 trace. This further supports the idea of electron localization for the 4,4' substitution being focused on the Re(I) center whereas for the 5,5' substitution it resides on the bipyridine ligand.

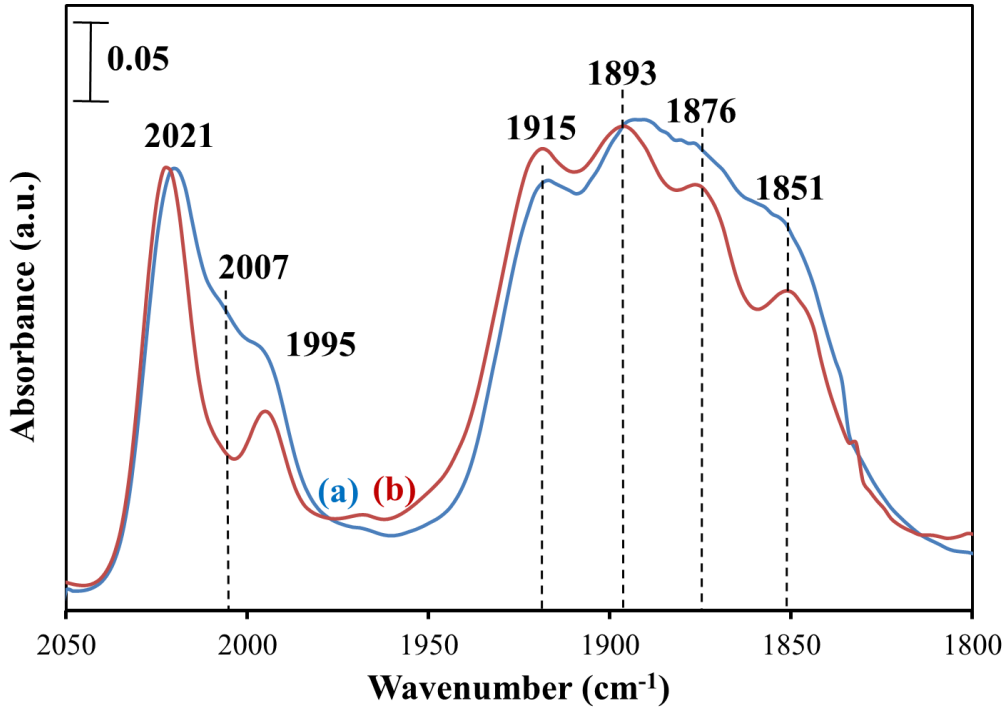

Figure 21. DRIFTS spectra of Re-D4-SBA-15 (a) and Re-D5-SBA-15 (b) in the presence of TEOA and CO_2. Each sample was ground with KBR. Spectra were collected prior to light irradiation.

To help probe the surface chemistry of this phenomenon for Re-D5-SBA-15, *in situ* DRIFTS spectroscopy experiments were employed in the presence of TEOA and CO_2. For the samples prior to light irradiation, six Re(I)-carbonyl bands are observed which indicate two different species coordinated to the Re(I) center (Fig. 21). Previous studies show the bands at 1995, 1876, and 1851 cm^{-1} are Re(I)-hydroxyl species, $Re(L\text{-}bpy)(CO)_3(OH)$.[73] Bands at 2021, 1919 and 1897 cm^{-1}

indicate a CO_2 adduct bound with the electron donor TEOA, $Re(L\text{-}bpy)(CO)_3(CO_2\text{-}OCH_2CH_2NR_2)$. It should be noted that this species has been previously investigated as an active component of the CO_2 reduction cycle.[29]

One immediate difference that is apparent is the band at 2007 cm^{-1} which is seen for Re-D5-SBA-15 but is not observed for Re-D4-SBA-15. It is not immediately apparent which species this corresponds to due to the lack of two other carbonyl bands which are associated with Re(I) bound species. To investigate the occurrence of this species and why Re-D5-SBA-15 promotes its formation was further probed via difference spectra from *in situ* irradiation. These spectra are obtained by subtracting the spectra prior to light irradiation from the corresponding spectra after light irradiation. A peak that is growing upward represents an infrared active species that is growing over time, and vice versa for a peak that is decreasing downward. For each experiment, catalyst was mixed with KBr and TEOA then loaded into the DRIFTS cell. The atmosphere was purged with Ar and CO_2 then sealed under CO_2. Solar simulated light via a fiber optic cable was then placed on the cell and irradiated samples, where scans were taken over a time.

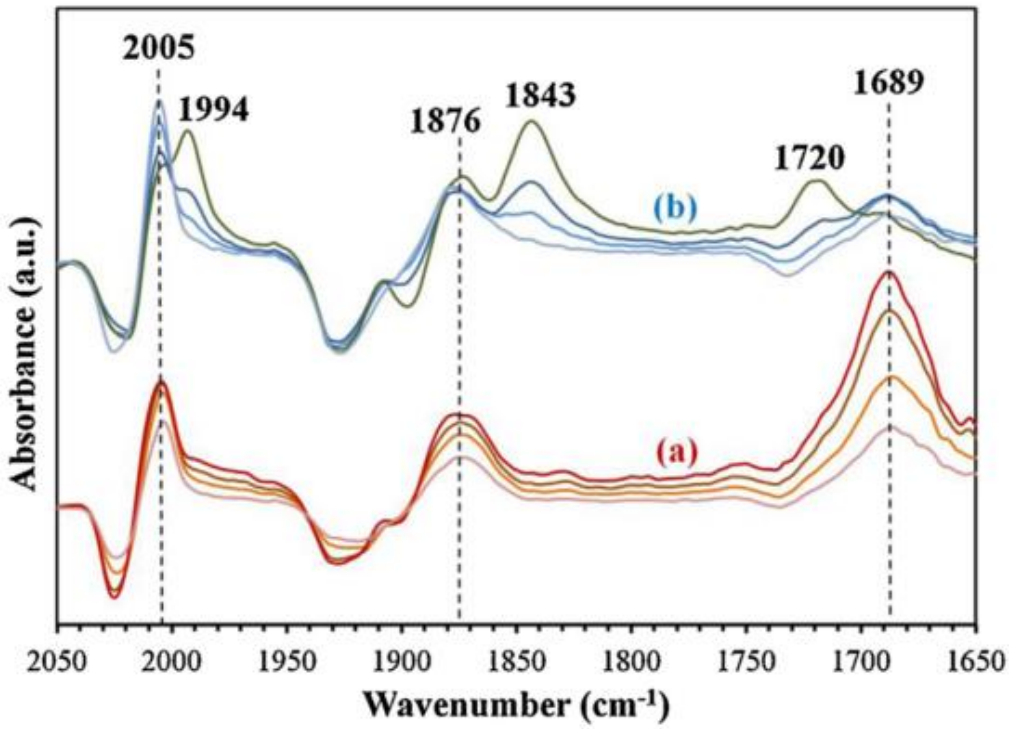

Figure 22. DRIFTS difference spectra of Re-D4-SBA-15 (a) and Re-D5-SBA-15 (b) in the presence of CO_2 and TEOA. Spectra were obtained by subtracting spectra collected before light irradiation (t=0) from spectra collected after light irradiation for different times (5, 15, 30 and 60 min).

Figure 22 shows the difference spectra of Re-D5-SBA-15 and Re-D4-SBA-15 after being irradiated for 1 hour. Negative peaks of 2025, 1920 and 1900 cm^{-1} (not labeled) represent the previously discussed CO_2 bound active species $Re(L\text{-}bpy)(CO)_3(CO_2\text{-}OCH_2CH_2NR_2)$ being photochemically converted over time. This supports previous literature stating that the Re(I) adduct is the real catalyst in CO_2 reduction systems using this type of ligand structure. Peaks at 2005 and 1876 cm^{-1} can be seen growing in both samples with continued light irradiation. These peaks are attributed to the reduced CO_2 bound Re(I) adduct which forms a formyl, $Re(L\text{-}bpy)(CO)_3(COH)$.[85-86] Interestingly over time, Re-D5-SBA-15 shows a large increase at 1994 and 1843 cm^{-1} towards later light irradiation times, which indicates a large growth of the hydroxyl

species Re(L-bpy)$(CO)_3$(OH). This species has been previously attributed as a deactivating species to CO_2 reduction and could possibly explain the lower TON seen for Re-D5-SBA-15 in photocatalysis experiments versus Re-D4-SBA-15.[73] It is not immediately apparent why the change in substitution would favor the formation of this deactivating species. An additional broad band is seen growing at 1689 cm^{-1} for both samples which is attributed to the formation of a tertiary carbamate on the surface.[87] This is a result of a reaction of excess CO_2 and TEOA on the surface of the catalyst in photochemical conditions.

It can be noticed that for Re-D5-SBA-15 the peak around 2025 cm^{-1} corresponding to the catalytically active adduct becomes less negative after 5 minutes of irradiation. This can represent the formation of a different species under the continued irradiation. Additionally, peaks at 1994, 1843, and 1720 cm^{-1} in the Re-D5-SBA-15 spectrum only appear after 5 minutes of irradiation. To help further probe this, a different set of subtraction data was obtained by subtracting spectra at the 5 minute mark from ones collected at 15, 30 and 60 minutes. These new difference spectra are shown in Figure 23.

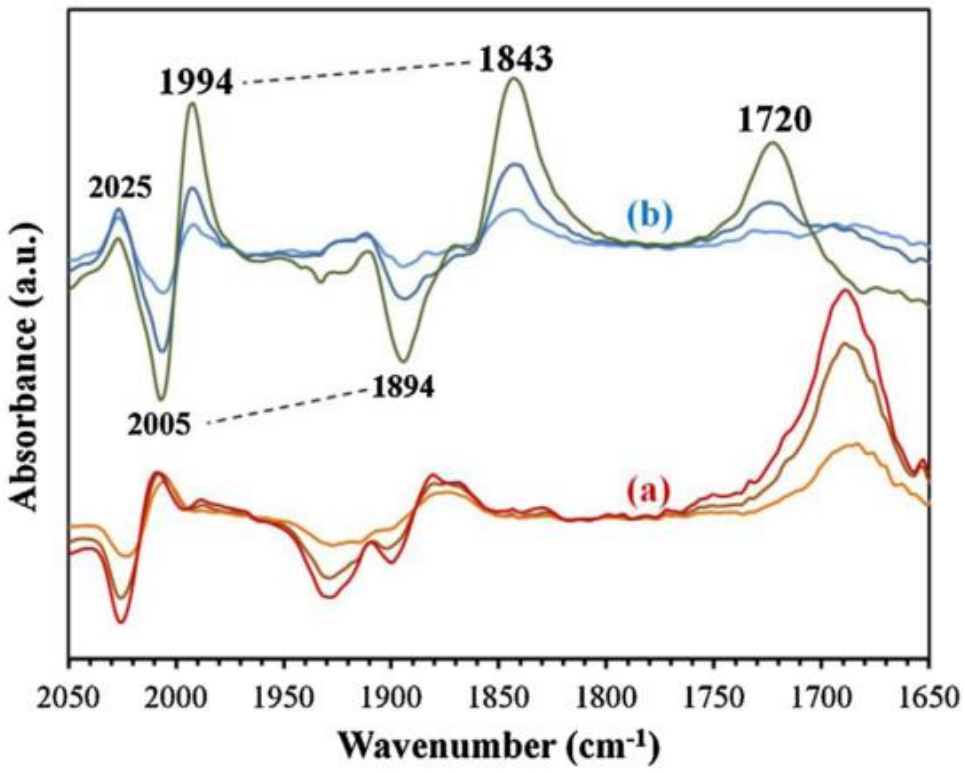

Figure 23. DRIFTS difference spectra of Re-D4-SBA-15 (a) and Re-D5-SBA-15 (b) in the presence of CO_2 and TEOA. Spectra were obtained by subtracting spectra collected at 5 min of light irradiation (t=5) from spectra collected at t=15, 30, and 60 min.

For these spectra there are not any significant differences for Re-D4-SBA-15 from the subtraction spectra in Figure 22. Negative peaks at 2025, 1920 and 1900 cm^{-1} (not labeled) are still observed indicating the photochemical conversion of the catalytically active species $Re(L\text{-}bpy)(CO)_3(CO_2\text{-}OCH_2CH_2NR_2)$. It is clearer for Re-D5-SBA-15 the formation of the deactivation pathway species, Re-OH. Peaks at 2005 and 1894 cm^{-1} that are decreasing are attributed to the disappearance of the photo reduced CO_2 adduct, $Re(L\text{-}bpy)(CO)_3(COH)$. Whereas peaks at 1994 and 1843 cm^{-1} continue to increase representing the deactivating hydroxyl species, $Re(L\text{-}bpy)(CO)_3(OH)$. Why this deactivation pathway is not present for the Re-D4-SBA-15 system is still not apparent. Additionally, for Re-D5-SBA-15 the appearance of two infrared bands around 2025 and 1720 cm^{-}

^{1} are also observed in the spectra shown in Figure 23b. It should be noted that the peak at 2025 cm^{-1} should be more intense upward but is buried by the concurrent decrease of the photochemical active species of Re(L-bpy)$(CO)_3(CO_2\text{-}OCH_2CH_2NR_2)$. These two additional bands are attributed to the formation of a possible carbonate-bridge binuclear Re(I) complex, $(CO)_3$(L-bpy)Re-OCO_2-Re(L-bpy)$(CO)_3$.[86] The absorption at 1720 cm^{-1} represents the C=O stretching mode of the carbonate bridge. Two additional bands associated with the binuclear complex are expected at 1893 and 1852 cm^{-1} but are not clearly seen in this spectrum. This is likely due to the overlapping and subtraction of multiple carbonyl bands in this region. This species has been previously proposed as an intermediate for this system by Agarwal and coworkers.[26] A carbonate-bridged Re(I) dimer is active in a binuclear mechanism of CO_2 reduction where one CO molecule is produced from the reduction of the carbonate bridged structure. This species could be supported by the substitution of the Re-D5-SBA-15 complex where two Re(I) centers on a dipodal ligand are forced to have close proximity. This proximity could help facilitate this carbonate dimer formed during photocatalysis.

2.1.4 Summary

In summary, Re(I) hybrid catalysts were successfully synthesized and characterized using DRIFTS, UV-Vis and EPR spectroscopies. Building upon previous work, a dipodal coupling agent was implemented in tandem to help force proximity of Re(I) centers. Additionally, the derivatization of the bipyridine ligands were altered to the 5,5' positions to compare to the 4,4' derivatization previously studied. This change in substitution for 5,5' resulted in an interesting color change of the hybrid photocatalyst upon light irradiation which was determined to be a shift in electron localization on the bipyridine ring. This shift in electron density likely explains the species that are observed for each sample in infrared studies. Formation of a possible carbonate

Re(I) dimer for the 5,5' substituted species correlate with a change in geometry and sterics allowing for this binuclear species to form. The increased formation of Re(I) hydroxyl as a deactivating pathway for the 5,5' substituted catalyst is not apparent versus the 4,4' substitution.

The results in this section are published in *J. Mol. Catal. A* **2016**, 411, 272-278.

2.2 Utilization of a light absorbing coupling agent and variation of substitution on hybrid Re(I) complexes

2.2.1 Introduction

Deposition of homogeneous Re(I) catalysts onto heterogeneous surfaces can be beneficial in studying the mechanism of CO_2 reduction. Changes in ligand substitution showed drastic effects on the photocatalytic properties of these catalysts and help further the understanding of their properties. Many researchers have not only studied the effects of substitution, but also the light absorbing characteristics of the materials on which they are deposited. Mesoporous silica simply acts as an inert support material for the ligand structure and does not participate in catalytic activity. However light absorbing surface materials or semiconductors can be utilized as support materials to help further the photocatalytic efficiency by participating in the catalytic cycle.

One example is MOF's where the framework of the ligand acts as a support material that can be active in photocatalysis. A bipyridine ligand with 5,5' carboxylic derivatization was utilized by Wang and coworkers to form their MOF material.[83] This material showed greater CO_2 reduction activity versus the parent Re(I)-bpy complex. Additionally, Fei and coworkers developed a similar Mn(I) system that incorporated Zr(IV) to improve robustness of the material.[88] Their MOF system showed increased efficiency to previous homogeneous systems in reduction of CO_2 to formate under visible light conditions.

More relevant to our approach, Takeda and co-workers synthesized a biphenyl bridged structure incorporated into a mesoporous silica.[74] A Re(I) complex was then covalently immobilized onto this mesoporous organosilica (PMO) material. During photocatalysis, UV light was absorbed by the biphenyl network and was able to transfer that resonance energy to the Re(I) catalyst. This in turn increased the CO_2-to-CO conversion as compared to direct photoexcitation of the Re(I) complex, demonstrating the surface involvement of CO_2 reduction. This allowed the support material to not only be a site to help reduce catalyst degradation but improve efficiency as well. These researchers then further built upon this work by utilizing different PMO materials to deposit supramolecular Ru(II)-Re(I) complexes.[75] To a similar effect, catalytic efficiency was increased under visible light using a PMO material versus direct excitation of the catalyst center.

We not only aim to use a coupling agent that acts like the PMO's discussed, but additionally vary the substituents of the bipyridine ring to study their effects. Previously, an aminopropyltrimethoxysilane (APTMS) was utilized to help anchor the Re(I) catalyst to the mesoporous surface. This anchor has no resonance properties and thus does not aid in catalysis. By introducing the coupling agent, aminophenyltrimethoxysilane, where a phenyl ring incorporated into our coupling agent can act as a light absorber, similar to the work shown by Takeda et al. It also has the advantage where the position of the amine can be varied from meta or para, to study the effect of substitution for that coupling agent. The Re(I) complexes deposited will also be varied between carboxylic and alkyl substituted bipyridines. By using a carboxylic functionalized bipyridine, conjugation will be carried from the Re(I) center to the light absorbing coupling agent, whereas the alkyl functionalization breaks that conjugation. For this study a silica nanoparticle will be utilized versus a mesoporous structure to prevent diffusion effects on the

photocatalysts. We aim to study if conjugation between the bipyridine ring and surface-linker influences photocatalysis efficiency, as well as if substitution of the light absorber has any effect.

2.2.2 Experimental

a. Materials

All chemicals were used as received without any further purification. Aerosil 200 silica, hydrochloric acid, triethylamine (TEA), triethanolamine (TEOA), toluene, diethyl ether, dichloromethane (DCM), dimethylformamide (DMF), thionyl chloride, 2,2'-bipyridine-4,4'-dicarboxylic acid, pentacarbonyl chlororhenium (I) (98%), tris(2,2'-bipyridine) dichlororuthenium(II) hexahydrate (99%, denoted "$Ru(bpy)_3^{2+}$") were obtained from Sigma-Aldrich. m-aminophenyltrimethoxysilane, and p-aminophenyltrimethoxysilane were obtained from Gelest.

b. Synthesis

Synthesis of Meta-Aminophenyl Functionalized SiO_2 Materials

100 mg of Aerosil 200 silica (SiO_2) was dried at 100^oC for 2 hours before being dispersed in 50 mL dry toluene under inert atmosphere. 154 µL of m-aminophenyltrimethoxysilane was added and the solution was refluxed for 24 hours under nitrogen atmosphere. The product was recovered via centrifugation and washed three times with toluene, diethyl ether and DCM respectively. The resulting cream colored powder was then dried under vacuum.

Synthesis of Para-Aminophenyl Functionalized SiO_2 Materials

100 mg of Aerosil 200 silica (SiO_2) was dried at 100^oC for 2 hours before being dispersed in 50 mL dry toluene under inert atmosphere. 0.189 g of p-aminophenyltrimethoxysilane was added and the solution was refluxed for 24 hours under nitrogen atmosphere. The product was recovered via

centrifugation and washed three times with toluene, diethyl ether and DCM respectively. The resulting brown powder was then dried under vacuum.

Synthesis of 4,4'-Acylated Bipyridines

In a typical synthesis, 100 mg of 4,4'-dicarboxylic-2,2'-bipyridine was dispersed in 15 mL of thionyl chloride. This solution was heated to 85^{o}C under inert atmosphere and refluxed overnight. Rotary evaporation was used to isolate the acylated yellow powder.

Synthesis of 4,4'-dicarboxylicbipyridine-meta-aminophenyl Functionalized SiO_2

100 mg of m-aminophenyl functionalized SiO_2 was dispersed in 40 mL DCM under N_2 flow. Then, freshly synthesized 4,4'-dichloro-2,2'-bipyridine was then dispersed in 15 mL DCM and added dropwise to the stirring silica solution under continued N_2 flow. The solution was then heated to 70^{o}C and stirred overnight. The product was retrieved via centrifugation and washed three times with DCM, diethyl ether and DCM again respectively. A yellow powder was isolated via drying under vacuum.

Synthesis of 4,4'-dicarboxylicbipyridine-para-aminophenyl Functionalized SiO_2

100 mg of p-aminophenyl functionalized SiO_2 was dispersed in 40 mL DCM under N_2 flow. Then, freshly synthesized 4,4'-dichloro-2,2'-bipyridine was then dispersed in 15 mL DCM and added dropwise to the stirring silica solution under continued N_2 flow. The solution was then heated to 70^{o}C and stirred overnight. The product was retrieved via centrifugation and washed three times with DCM, diethyl ether and DCM again respectively. A light yellow powder was isolated via drying under vacuum.

Synthesis of 4,4'-dialkylbipyridine-para/meta-aminophenyl Functionalized SiO_2

150 mg of m-aminophenyl functionalized SiO_2 was dispersed in 40 mL chloroform under N_2 flow. Then, 25 mg synthesized 4-bromo-4'-methyl-2,2'-bipyridine was then added slowly to the stirring

silica solution under continued N_2 flow. The solution was then refluxed and stirred overnight. The product was retrieved via centrifugation and washed three times with chloroform, diethyl ether and DCM again respectively. A brown powder was isolated via drying under vacuum.

Synthesis of 4,4'-dialkylbipyridine-para-aminophenyl Functionalized SiO_2

150 mg of p-aminophenyl functionalized SiO_2 was dispersed in 40 mL chloroform under N_2 flow. Then, 25 mg synthesized 4-bromo-4'-methyl-2,2'-bipyridine was added slowly to the stirring silica solution under continued N_2 flow. The solution was then refluxed and stirred overnight. The product was retrieved via centrifugation and washed three times with chloroform, diethyl ether and repeated DCM respectively. A brown powder was isolated via drying under vacuum.

Synthesis of $Re(CO)_3Cl$-4,4'-dicarboxylicbipyridine-meta-aminophenyl Functionalized Silica (Re-CM-SiO_2)

150 mg of 4,4'-bipyridine-m-aminophenyl functionalized SiO_2 was dispersed in 50 mL dry toluene. 50 mg of pentacarbonyl chlororhenium(I) was added to the solution under stirring. The solution was then heated to 95^{o}C under inert atmosphere and was stirred overnight while covered with foil to reduce light exposure. The product was then retrieved via centrifugation and washed three times with toulene, diethyl ether and repeated DCM respectively. A orange-brown powder was isolated and dried under vacuum.

Synthesis of $Re(CO)_3Cl$-4,4'-dicarboxylicbipyridine-para-aminophenyl Functionalized Silica (Re-CP-SiO_2)

150 mg of 4,4'-bipyridine-p-aminophenyl functionalized SiO_2 was dispersed in 50 mL dry toluene. 50 mg of pentacarbonyl chlororhenium(I) was added to the solution under stirring. The solution was then heated to 95^{o}C under inert atmosphere and was stirred overnight while covered with foil to reduce light exposure. The product was then retrieved via centrifugation and washed three times

with toulene, diethyl ether and repeated DCM respectively. A brown powder was isolated and dried under vacuum.

Synthesis of $Re(CO)_3Cl$-4,4'-dialkylbipyridine-meta-aminophenyl Functionalized Silica (Re-AM-SiO_2)

150 mg of 4,4'-dialkylbipyridine-m-aminophenyl functionalized SiO_2 was dispersed in 50 mL dry toluene. 50 mg of pentacarbonyl chlororhenium(I) was added to the solution under stirring. The solution was then refluxed under inert atmosphere and was stirred overnight while covered with foil to reduce light exposure. The product was then retrieved via centrifugation and washed three times with toulene, diethyl ether and repeated DCM respectively. A brown powder was isolated and dried under vacuum.

Synthesis of $Re(CO)_3Cl$-4,4'-dialkylbipyridine-para-aminophenyl Functionalized Silica (Re-AP-SiO_2)

150 mg of 4,4'-dialkylbipyridine-p-aminophenyl functionalized SiO_2 was dispersed in 50 mL dry toluene. 50 mg of pentacarbonyl chlororhenium(I) was added to the solution under stirring. The solution was then refluxed under inert atmosphere and was stirred overnight while covered with foil to reduce light exposure. The product was then retrieved via centrifugation and washed three times with toulene, diethyl ether and repeated DCM respectively. A brown powder was isolated and dried under vacuum.

c. Characterization

Elemental analysis of the metal content of synthesized materials was performed post acid digestion using a Varian Vista AX inductively coupled plasma atomic emission spectrometer (ICP-AES). Optical spectra of hybrid silica samples were obtained using a Cary 50 Bio spectrophotometer outfitted with a Barrelino diffuse reflectance probe. Diffuse reflectance infrared Fourier-transform

spectroscopy (DRIFTS) were collected on a Nicolet 6700 FTIR spectrometer equipped with a Harrick Praying Mantis diffuse reflectance accessory.

d. Photocatalytic Testing

For a typical photocatalytic CO_2 reduction test, 10 mg of sample was dispersed in 4 mL of a 3:1 DMF:TEOA solution in a quartz test tube with a mini stir bar. The sample tube was sealed with a septum and parafilm, then bubbled with CO_2 (99.999% Airgas) for 30 minutes in dark. Once bubbling was completed, the sample was irradiated with a 300-W Xe Arc lamp with an attached water filter and an AM 1.5 optical filter. For visible light experiments, a Fiber-Light series 180 lamp was utilized with a water filter. The light intensity for both was fixed at 100 mW/cm^2. While the reaction solution was stirred under light, the head space was sampled using a gas tight syringe for analysis using an Agilent 7820 GC equipped with a Thermal Conductivity Detector (TCD) and a 60/80 Carboxen 1000 column.

2.2.3 Results and Discussion

For this study, a light absorbing coupling agent was introduced. This acts as an active participant in photocatalytic CO_2 reduction as well as serving the role to covalently link the Re(I) complex to the SiO_2 surface. Introduction of this phenyl unit as a light absorber can lead to greater harnessing of energy from light and transfer via conjugation to the Re(I) complex. Addtionally, these phenyl based linkers can help absorb visible radiation, which can allow photocatalytic reduction under visible light conditions (as opposed to strictly UV). Additional investigation of the meta versus para configuration of these coupling agents provide clues to the effects of substitution at the linker level towards catalyst performance in regards to sterics or electronic interactions.

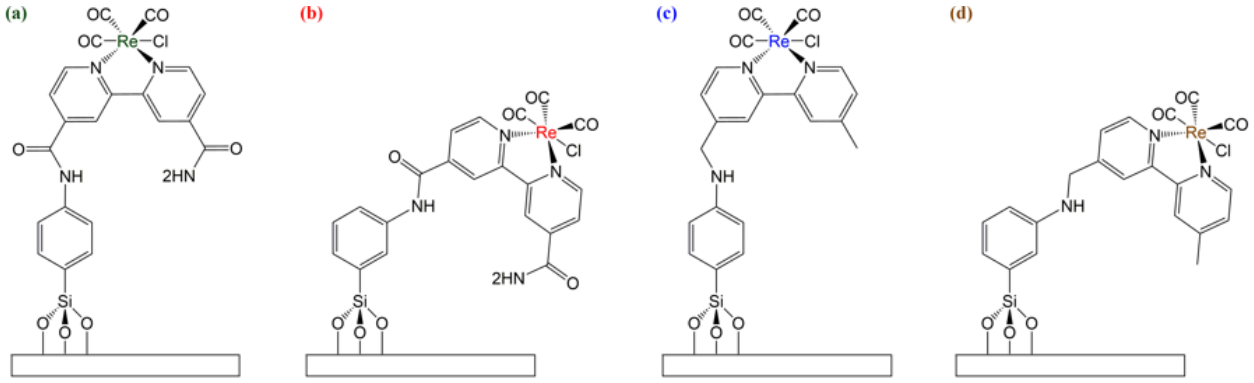

Figure 24. Structures for para and meta phenyl functionalized Re(I) complexes with both carboxylic and alkyl substituted bipyridines. a) Re-CP-SiO_2 b) Re-CM-SiO_2 c) Re-AP-SiO_2 d) Re-AM-SiO_2

Each sample synthesized had a brown to orange color upon isolation indicating a greater range of absorbance in the visible region. The use of the light absorbing coupling agent is the reason for this greater absorbance and demonstrates its possible utility in harnessing more visible light for photocatalytic reduction. To evaluate this, DRUV's was used to determine the extent of the increased photoabsorption (Fig. 25). Each sample has a band around 410 nm which represents the MLCT of the Re(I) complex.[72] Additionally, there is band broadening from the 400-700 nm visible region. This broadening is attributed to the light absorbing nature of the phenyl coupling agent utilized. For the amide derivatized samples, Re-CP-SiO_2 and Re-CM-SiO_2 the broadening is more significant as conjugation from the bipyridine ring to the phenyl ring is maintained through the amide bond. This is not the case for the alkyl samples due to the lack of similar conjugation.

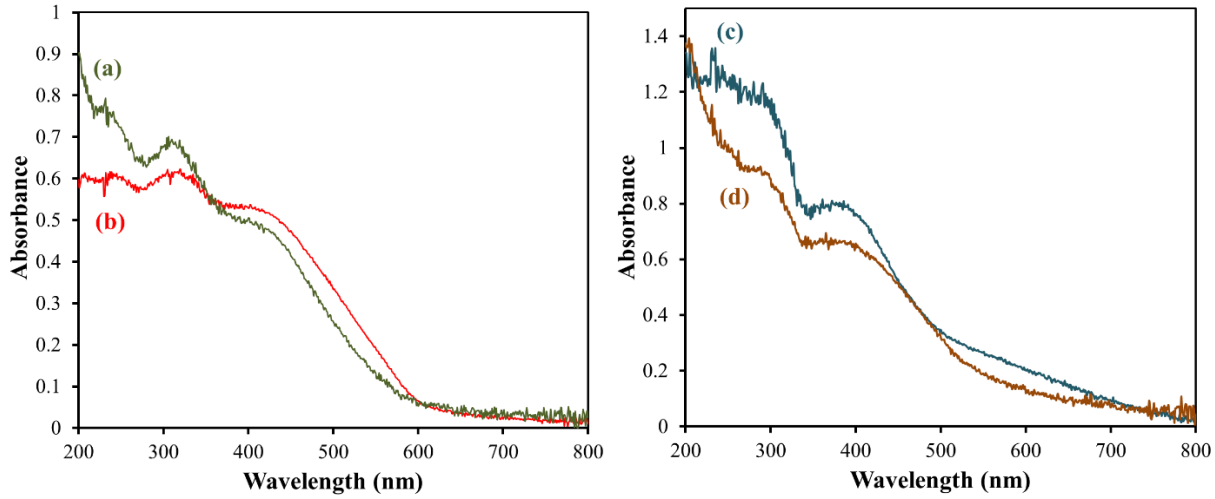

Figure 25. Diffuse reflectance UV-visible spectra (DRUV) of Re-CP-SiO_2 (a) Re-CM-SiO_2 (b) Re-AP-SiO_2 (c) and Re-AM-SiO_2 (d) in powder form. Barium sulfate was used as the background.

Using DRIFTS spectroscopy, Fig. 26 shows spectra all four Re(I) samples mixed with KBr as a background. All four samples show Re(I)-carbonyl bands at 2022 cm^{-1} and 1920 cm^{-1} as well as fingerprint region absorptions that are not labeled. These carbonyl bands indicate the presence of the dimine-tricarbonyl Re(I) catalyst on the surface, indicating successful coordination of the Re(I) complex.[71-73] For the amide derivatized samples there is a small peak around 1700 cm^{-1} indicating the carbonyl present in the amide bond, which is not present in the alkyl samples.

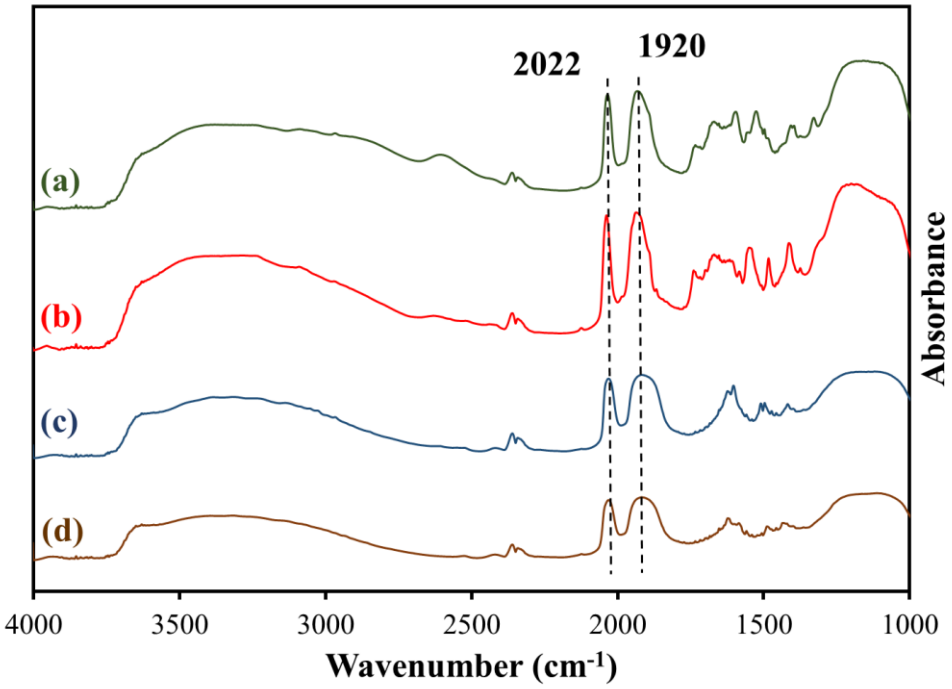

Figure 26. DRIFTS spectra Re-CP-SiO_2 (a) Re-CM-SiO_2 (b) Re-AP-SiO_2 (c) and Re- AM-SiO_2 (d) in powder form. KBr was mixed with each sample and served as the background.

To determine the loading of Re(I) for each sample, elemental analysis was performed via ICP-AES after acid digestion. Each sample was dissolved in HF for 24 hours and diluted 300-fold with milli-Q water before analysis. The Re loading for each sample is shown in Table 1 below. Unfortunately, loadings do not seem to show a trend between samples and vary from sample to sample. The reason for differences is not trivial and some factors could include experimental or measurement error.

Sample Name	Rhenium Loading (μmol/10mg)
Re-CM-SiO_2	2.75
Re-CP-SiO_2	1.79
Re-AM-SiO_2	4.12
Re-AP-SiO_2	3.39

Table 1. Elemental loadings for silica samples. Re content is reported as μmol/10 mg.

Each sample was tested for photocatalytic reduction of CO_2 under two different light conditions. Initially each sample was tested under UV irradiation without the presence of a photosensitizer, then tested again under visible irradiation with the presence of $Ru(bpy)_3^{2+}$ as a photosensitizer. TEOA was used as a sacrificial electron donor and CO was the only observed product of CO_2 reduction. Figure 27 shows the results from both experiments, where under UV light, Re-AM-SiO_2 and Re-CM-SiO_2 showed slightly increased performance than Re-CP-SiO_2 and Re-AP-SiO_2. However, these TON are quite low for all samples compared to hybrid Re(I) catalysts previously studied, where TON's in the 60s were obtained. It is not immediately obvious why a meta configuration would perform more efficiently in CO_2 reduction versus a para configuration. When performed under visible light, Re-CP-SiO_2 and Re-CM-SiO_2 with the continued conjugation through the amide bond showed increased TON than Re-AP-SiO_2 and Re-AM-SiO_2 respectively. This indicates the importance of this continued conjugation and enhancement of absorption in the visible region as shown by UV-Vis experiments. This suggests the ability to absorb more light in

the visible region led to increased CO_2 reduction efficiencies from the addition of the phenyl light absorber.

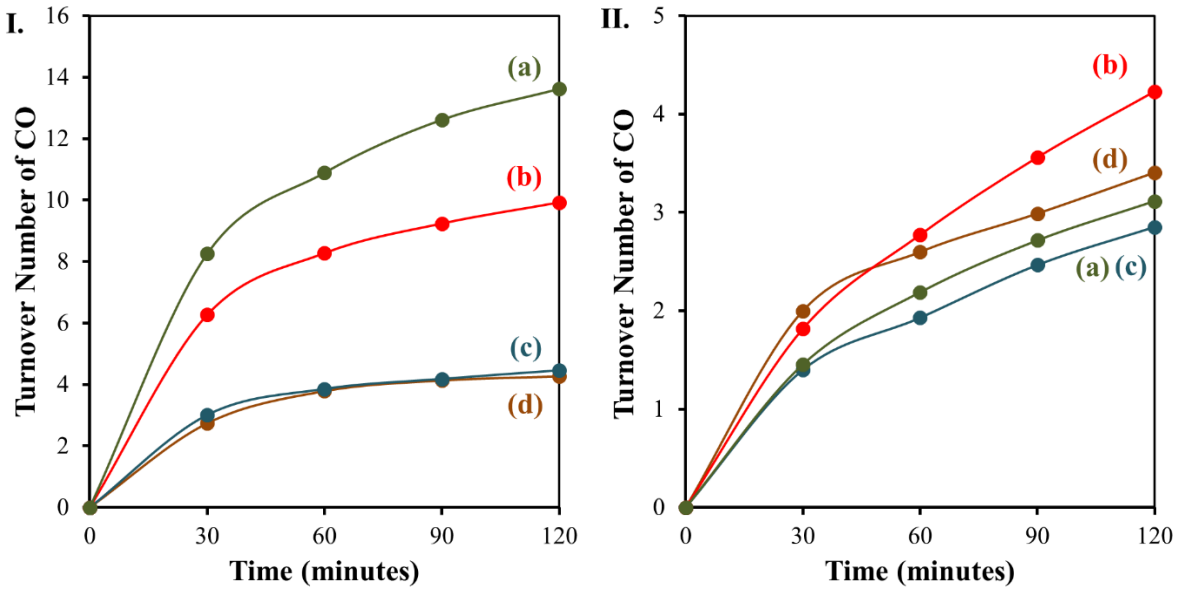

Figure 27. CO production in photocatalytic CO_2 reduction using Re-CP-SiO_2 (a) Re-CM-SiO_2 (b) Re-AP-SiO_2 (c) and Re- AM-SiO_2 (d) under simulated solar irradiation (I) and visible light (II). In visible light testing, $Ru(bpy)_3^{2+}$ was used as a photosensitizer. Light intensity was 100 mW/cm^2 for all photocatalytic testing.

To help understand the difference in photocatalytic performance, *in situ* DRIFTS experiments were performed with Hg light under the presence of CO_2 and TEOA. Prior to light irradiation, three Re(I)-carbonyl bands are observed for Re-CP-SiO_2 and Re-CM-SiO_2 whereas six Re(I)-carbonyl bands are observed for Re-AP-SiO_2 and Re-AM-SiO_2 (Fig. 28). Bands are observed for all 4 complexes at around 2021, 1919 and 1897 cm^{-1} which represent a CO_2 adduct bound with the electron donor TEOA, $Re(L\text{-}bpy)(CO)_3(CO_2\text{-}OCH_2CH_2NR_2)$.[29] Any variations in wavenumber could be attributed to the slightly different environments for each sample based on structural orientation. For Re-AP-SiO_2 and Re- AM-SiO_2, they show the bands at 1995, 1875, and 1851 cm^{-1} which correspond to a Re(I)-hydroxyl species, $Re(L\text{-}bpy)(CO)_3(OH)$.[73] These results indicate

that the alkyl substitution on the bipyridine ring supports the formation of Re(I)-hydroxyl species before light irradiation.

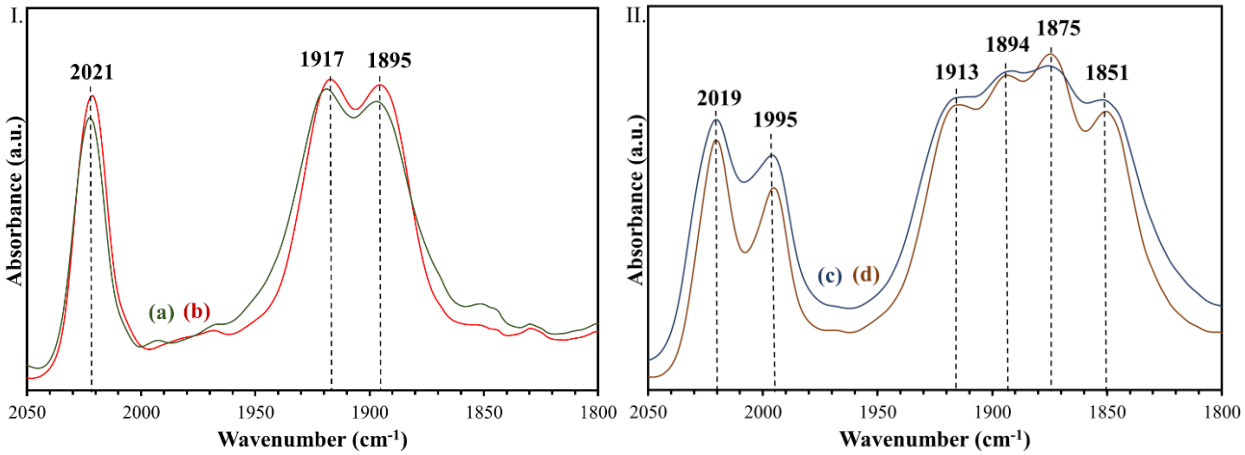

Figure 28. DRIFTS spectra of (I) Re-CP-SiO_2 (a) Re-CM-SiO_2 (b) (II) Re-AP-SiO_2 (c) and Re-AM-SiO_2 (d) in the presence of TEOA and CO_2. Each sample was ground with KBr. Spectra were collected prior to light irradiation.

Each sample was irradiated with light for one hour using an Hg lamp and a fiber optic cable. Spectra were collected over the time course and are subtracted from the initial spectrum prior to irradiation. Figures 29 a and b show difference spectra for each complex at t=2, 10, 30 and 60 min. For Re-CP-SiO_2 and Re-CM-SiO_2 peaks at 2025 and 1921 cm^{-1} correspond to the disappearance of the active bound species of TEOA, Re(L-bpy)$(CO)_3(CO_2$-$OCH_2CH_2NR_2)$. Increasing are peaks at 2003 and 1873 cm^{-1}, which correspond to the formyl bound species, Re(L-bpy)$(CO)_3$(COH).[25] The peak at 1697 cm^{-1} is attributed to the formation of a carbamate from oxidation of TEOA as seen in previous studies.[89] Both Re(I) species present are active intermediates for CO_2 reduction. This suggests that the higher productivity seen in visible light photocatalysis could be attributed to the lack of deactivating species pathways such as Re(I)-hydroxyl, which are seen in alkyl

substituted samples prior to light irradiation. Once the hydroxyl is bound to the Re(I) center, it is a poor leaving group thus hindering further catalysis.[73]

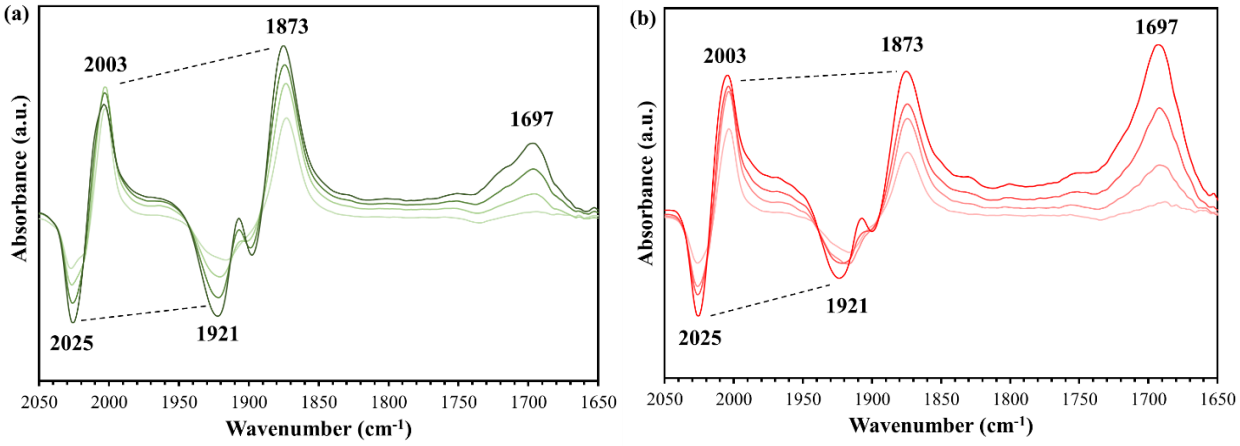

Figure 29. DRIFTS difference spectra of Re-CP-SiO_2 (a) and Re-CM-SiO_2 (b) in the presence of CO_2 and TEOA. Spectra were obtained by subtracting spectra collected before light irradiation (t=0) from spectra collected after light irradiation for different times (2, 10, 30, and 60 min).

In Figure 30, difference spectra are shown for alkyl substituted samples Re-AP-SiO_2 and Re-AM-SiO_2. Similar to the amide substituted samples, decreasing peaks at 2027 and 1925 cm^{-1} are attributed to the active bound species of TEOA, Re(L-bpy)$(CO)_3(CO_2$-$OCH_2CH_2NR_2)$. However, peaks increasing at 2013 and 1884 cm^{-1} are unique to these samples. These peaks correspond to a carboxylic acid bound Re(I) complex, Re(L-bpy)$(CO)_3(CO_2H)$.[85-86] This species is known as a possible intermediate of CO_2 reduction for this system, however requires a proton source to be catalytic.[16, 86] Re(I) can dimerize in the presence of CO_2 to form a carboxylate dimer, Re(L-bpy)$(CO)_3(CO_2)$-Re(L-bpy)$(CO)_3$ although its formation is slow and has been identified as an intermediate.[25] However, Re(L-bpy)$(CO)_3(CO_2H)$ accumulates over time suggesting that it is a deactivating pathway due to the lack of HCl in this system. This indicates that it is a contributor to the lower photocatalytic activity of Re-AP-SiO_2 and Re-AM-SiO_2 under visible light conditions.

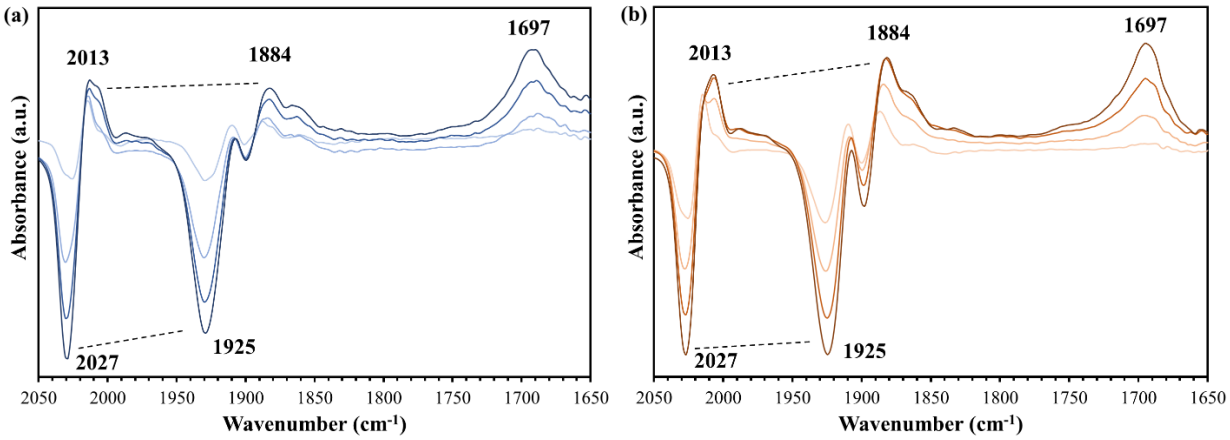

Figure 30. DRIFTS difference spectra of Re-AP-SiO_2 (a) and Re-AM-SiO_2 (b) in the presence of CO_2 and TEOA. Spectra were obtained by subtracting spectra collected before light irradiation (t=0) from spectra collected after light irradiation for different times (2, 10, 30, and 60).

However, what is not immediately clear is why the alkyl substitution under the same conditions as the amide generates more deactivating Re(I)-OH species to CO_2 reduction. There seems to be no effect from the change in orientation of how the bipyridine is binding covalently to the surface. Direct substitution of the bipyridine ring seems to have the greatest effect on species that form on the Re(I) center. The formation of a Re(I)-OH prior to light irradiation can be a component of the Re(I)-CO_2H species that is generated as photocatalysis is occurring. It's possible that there is CO insertion into the Re(I)-OH. In this case, it cannot be protonated and sequentially reduce, thus accumulating and decreasing CO turnover. Why exactly the alkyl substitution favors hydroxyl formation is still not clear.

With the formation of Re(I) species being dependent on the type of direct substitution on the bipyridine ring, it doesn't explain the effect of the light absorbing coupling agent that was utilized. For Re-CP-SiO_2 and Re-CM-SiO_2, which both show increased productivity versus Re-AP-SiO_2 and Re-AM-SiO_2 under visible irradiation (whereas all samples were comparable under UV

conditions). Why under UV conditions, DRIFTS showed the continued formation of deactivating species for Re-AP-SiO_2 and Re-AM-SiO_2 where it did not affect their TON as compared to Re-CP-SiO_2 and Re-CM-SiO_2 is not clear. Based upon DRIFTS results of Re(I) species observed, Re-CP-SiO_2 and Re-CM-SiO_2 should have a much higher TON due to the lack of deactivating species present.

For visible light experiments however, it can be suggested that continued conjugation through the amide for Re-CP-SiO_2 and Re-CM-SiO_2 had a positive effect on CO_2 reduction. Both showed increased TON whereas the meta configuration showed only slightly higher results. Orientation towards the surface could be important as CO_2 and TEOA can bind with the surface as suggested by the carbamate formation in all samples observed. Being oriented towards the surface could perhaps assist in the formation of the active Re(I)-(CO_2-$OCH_2CH_2NR_2$) species.

2.2.4 Summary

In summary, Re(I) hybrid catalysts were successfully synthesized using a light absorbing aminophenyl functionalized coupling agent. The orientation of the coupling agent as well as the effect of bipyridine substitution of amide versus alkyl ligands on the bipyridine ring was studied. Although no substantial differences were observed for samples under UV photocatalytic conditions, visible light irradiation showed increased CO TON for samples with continued conjugation through an amide bond. This suggests that the light absorbing character of the coupling agent can be utilized to increase CO reduction productivity. Infrared species showed the generation of deactivating Re(I) species for alkyl substituted samples which were absent for amide. This demonstrates the strong effect of derivatization of the bipyridine ring on catalysis and the formation of Re(I) catalytic intermediate species.

III. PHOTOCHEMICAL REDUCTION OF CO_2 USING COBALT MACROCYCLIC HYBRID MATERIALS

3.1 Introduction

Cobalt macrocycles are a class of homogeneous catalysts that have been studied for their role in CO_2 reduction.[16-17, 69, 90-92] Their electrochemical and photochemical properties have been extensively studied in different solvent systems, photosensitizers and macrocycles.[38-40, 93] However, the mechanism of CO_2 reduction is not completely understood, and efforts have been made to investigate the multiple intermediates that are formed during photocatalysis.

Co(cyclam) is of interest due to the simple ligand structure of the macrocyclic ring. Previous studies determined that adduct formation of the Co complex with CO_2 through hydrogen bonding interactions of the amine N-H with CO_2 is a crucial step in catalysis. [40, 94] Cyclam as a ligand has more amine protons available and less steric hinderance than complexes that were previously studied. A simple ligand structure also allows ligand modification to help promote adduct formation or enhance visible light absorption.

Co(cyclam) has previously been investigated by our group as a hybrid catalyst through deposition on P25 TiO_2.[95-96] Efforts were made to derivatize the structure through the amines on the ring, however attempts were unsuccessful. Instead, the Co(cyclam) when deposited formed an oxo bridge with TiO_2 through surface titanol groups. This oxo-bridged complex was more catalytically active than the parent complex mixed with TiO_2 physically, indicating successful electron transfer from the TiO_2 surface into the Co center. This in turn eliminated the need for a photosensitizer for photochemistry. Catalytic activity proceeds via the photosensitizer and they often degrade during

reaction conditions causing TON to level off over time. P25 TiO_2 will not degrade under these conditions, thus offers longer lifetime for catalysts.

Building upon this work, we aim to study Co(cyclam) and Co(HMD) both deposited on mesoporous silica, SBA-15. Two different macrocycles will be utilized to study the effect of sterics on the formation of CO_2 adduct. Co(HMD) has two less free amine protons than Co(cyclam) as well as additional methyl units, acting as a sterically hindered analogue. Additionally, SBA-15 is an inert support compared to TiO_2 so the primary focus will be on the interaction between CO_2 and the catalytic site rather than the electronic interactions between catalyst and surface.

3.2 Experimental

a. Materials

Triethylamine (TEA, ≥99%), triethanolamine (TEOA, ≥99%), hydrochloric acid (37%), acetonitrile (99.999%), p-terphenyl (≥99.5%), and 1,4,8,11-tetraazacyclotetradecane (cyclam, 98%), perchloric acid (70%) were obtained from Sigma-Aldrich. Methanol (99.9%) and mesityl oxide (90%) was purchased from Fisher Scientific. Cobalt(II) chloride hexahydrate (Analytical Reagent) was obtained from J. T. Baker. Ethanol (95.0%) and chloroform (99.8%) were purchased from Parmo Products Inc. All reagents were used without further purification. Non-porous fumed silica (Aerosil 200, specific surface area ~200 $m^2\ g^{-1}$, average primary particle size ~12 nm) was obtained from Evonik and used as received.

b. Synthesis

Synthesis of Co(cyclam)Co(cyclam)

Co(cyclam)Co(cyclam) was synthesized according to previously established literature.[95-97] In a typical synthesis, cobalt(II) chloride hexahydrate was added to a solution of cyclam dissolved in methanol. While stirring, air was bubbled to the brown solution for 1 hour. Concentrated

hydrochloric acid was added dropwise to the stirring solution changing its color to green. The solution was then further stirred for an hour then vacuum filtered to obtain a green solid. The solid was recrystallized from water at 80^{o}C and washed with acetone. Green needle-like crystals were obtained as Co(cyclam)Co(cyclam).

Microwave-assisted deposition of Co(cyclam) onto SBA-15 (Co(cyclam)/SBA-15)

To deposit the Co(cyclam) via microwave synthesis, 100 mg SBA-15 was initially dried at 100^{o}C in an oven one hour before use. The dried material was then mixed with 10 mg Co(cyclam) and 65 µL triethylamine in 15 mL acetonitrile. The mixture was sealed in a capped reaction vessel, which was then placed in a CEM Discover single-mode microwave reactor and underwent reaction at 80^{o}C for 2 hours. After the microwave reaction, the mixture remained green in color. The resulting precipitate was recovered by centrifugation in acetonitrile and washed twice with chloroform and twice with ethanol. After drying at room temperature, the Co(III) catalyst deposited on SBA-15 was obtained as a green powder and was denoted as "Co(cyclam)/SBA-15".

Synthesis of Co(HMD)

Co(HMD) was synthesized according to previously established literature.[98-99] To synthesize the 5,7,7,12,14,14-hexamethyl-1,4,8,11-tetra-azacyclotetradeca-4,11-diene (HMD) ligand, monohydroperchlorate diethylamine is dissolved in excess of mesityl oxide under heat. Crystals of HMD form in several minutes and it is isolated via filtration. To coordinate Co(III), methanol is refluxed for 30 min under N_2 initially. Cobalt(II) chloride is then slowly added to the hot solution, turning light purple. HMD ligand is added to the mixture, and the solution is refluxed for an additional 2 hrs. Orange crystals are formed and are isolated via filtration and washed will ethanol. The dried dark orange crystals isolated are denoted as Co(HMD).

Microwave-assisted deposition of Co(HMD) onto SBA-15 (Co(HMD)/SBA-15)

To deposit Co(HMD) via microwave synthesis, 100 mg SBA-15 was initially dried at 100^{o}C one hour before use. The dried material was then mixed with 10 mg Co(HMD) and 65 µL triethylamine in 15 mL acetonitrile. The mixture was sealed in a capped reaction vessel, which was then placed in a CEM Discover single-mode microwave reactor and underwent reaction at 80^{o}C for 2 hours. After the microwave reaction, the mixture remained brown in color. The resulting precipitate was recovered by centrifugation in acetonitrile and washed 2 times with chloroform and 2 times with ethanol. After drying at room temperature, the Co(III) catalyst deposited on SBA-15 was obtained as a brown powder and was denoted as "Co(HMD)/SBA-15".

c. Characterization

A Cary 50 Bio spectrophotometer equipped with a Barrelino diffuse reflectance probe was used to obtain the UV–visible spectra of powder samples using $BaSO_4$ as a background. The surface area, pore size distribution and total pore volume of mesoporous materials were measured on a NOVA 2200s Surface Area and Pore Size Analyzer. Scanning electron microscopy (SEM) images were obtained on an Amray 3300FE field emission SEM with a PGT Imix-PC microanalysis system. Infrared spectra were collected on a Thermo Nicolet 6700 FTIR spectrometer equipped with a Harrick Praying Mantis diffuse reflectance accessory. Elemental analysis was conducted by acid digestion of the synthesized catalysts, followed by quantification using a Varian Vista AX inductively coupled plasma atomic emission spectrometer.

d. Photocatalytic CO_2 Reduction

In photochemical CO_2 reduction, p-terphenyl was employed as a molecular photosensitizer while a mixture of TEOA and methanol was used as sacrificial electron donors. In a typical photocatalysis experiment, 10 mg catalyst was dispersed in a 4.0 mL acetonitrile solution containing 1.8 mg p-terphenyl, TEOA and methanol (acetonitrile: TEOA: methanol 4:1:1 v/v) in a quartz test tube. Prior to photocatalytic testing, the reaction suspension was bubbled with CO_2 (99.999%, Airgas) in the dark for 20 min, and then irradiated with a 200 W mercury lamp equipped with a water filter. The light intensity of the reaction solution was fixed at 100 mW cm^2. The head space above the reaction solution was sampled with a gas-tight syringe at different time intervals for product analysis using an Agilent 7820 GC equipped with a TCD detector and a 60/80 Carboxen-1000 packed column (Supelco).

3.3 Results and Discussion

To investigate the properties of Co(cyclam)/SBA-15 and Co(HMD)/SBA-15 on a surface, both Co(III) macrocyclic catalysts were successfully synthesized and deposited via microwave method onto mesoporous silica. Utilization of an inert surface prevents electronic interactions between the catalyst complex and the surface. This facilitates the study of the hybrid catalyst more like previous homogeneous literature, where electron transfer exclusively is provided via photosensitizer and not a support material. Additionally, the use of a sterically hindered macrocycle on a surface hinders CO_2 binding and thus photocatalytic activity. It is also possible the methyl units will hinder diffusion of reactants through the mesoporous silica network. This gives the ability to investigate the advantage of using a non-bulky macrocycle for CO_2 reduction on a surface.

The integrity of SBA-15 during microwave method was studied for Co(cyclam)/SBA-15 before and after deposition. Microwave heating is a more intense method than previous reflux methods where heating is rapid and pressurized, which could possibly damage the porous network. For

deposition and photocatalysis, the pore network must be unhindered to prevent diffusion issues with reactants or catalysts flowing through the network. This could lead to false trends during photocatalysis purely from this phenomenon. Fig. 31 shows the SEM images of SBA-15 before and after microwave deposition of Co(cyclam). Upon inspection, there is no significant change in structure or particle size of SBA-15 after microwave heating. Preservation of the "corn" like structure is maintained after treatment, and no significant deformations are seen.

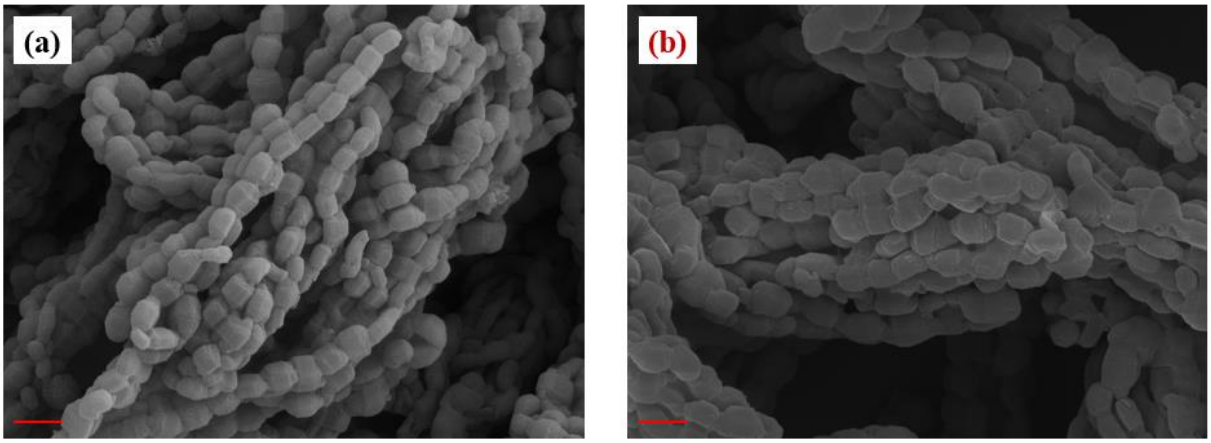

Figure 31. SEM images of SBA-15 (a) and Co(cyclam)/SBA-15 (b). Scale bars are 1 µm.

To evaluate the integrity of surface area and pore size-distribution, BET utilized was for both samples. As seen in Fig. 32, deposition of the Co(cyclam)/SBA-15 complex reduced the surface area and pore volume of SBA-15, due to catalyst being present throughout the network. SBA-15 was measured to have a surface area of 569 m^2g^{-1} and a pore volume of 0.685 cm^3 g^{-1}, whereas Co(cyclam)/SBA-15 was 408 m^2g^{-1} and a pore volume of 0.584 cm^3g^{-1}. Additionally, the pore size distribution remained essentially unchanged after reaction. This further indicates that SBA-15 during microwave heating did not undergo degradation and the uniformity of the porous network is maintained.

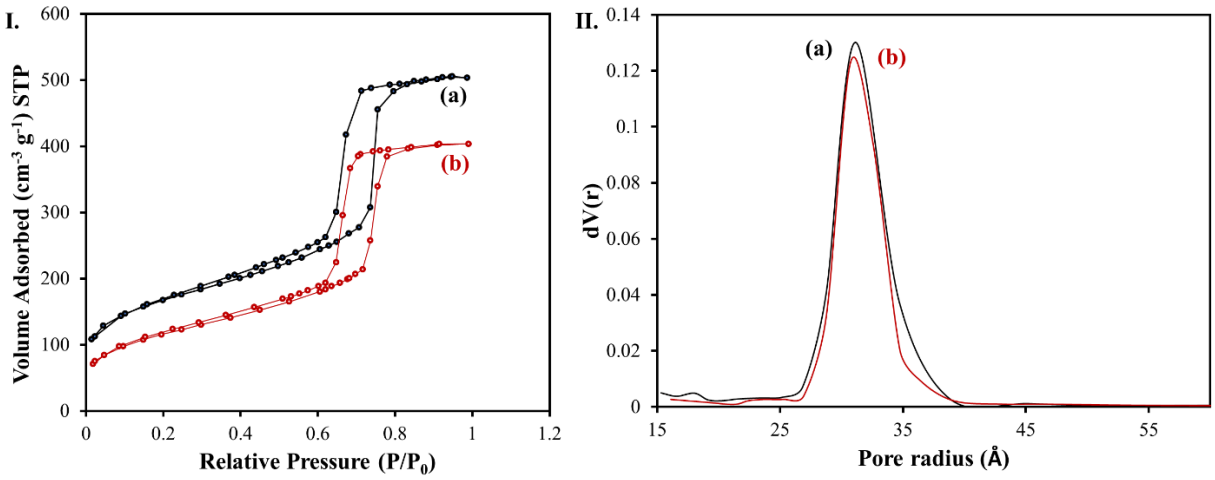

Figure 32. BET isotherms (I) of SBA-15 (a) and Co(cyclam)/SBA-15 (b). Pore-size distrubtion (II) shows uniform distribution.

However, upon recovery of Co(cyclam)/SBA-15 from the BET cell, the color of the material changed from a light green to brown. This change occurred during the degassing process, where the sample is dried at 200^{o}C for 4 hours under vacuum prior to analysis. Initially assuming the color was from a degraded complex on the surface, DRIFTS was employed to evaluate the integrity of the catalyst. This process was also repeated for Co(HMD)/SBA-15 however no obvious color change was observed due to the catalyst being brown in color after microwave deposition. Samples that underwent BET heating will be denoted as H-Co(HMD)/SBA-15 and H-Co(cyclam)/SBA-15.

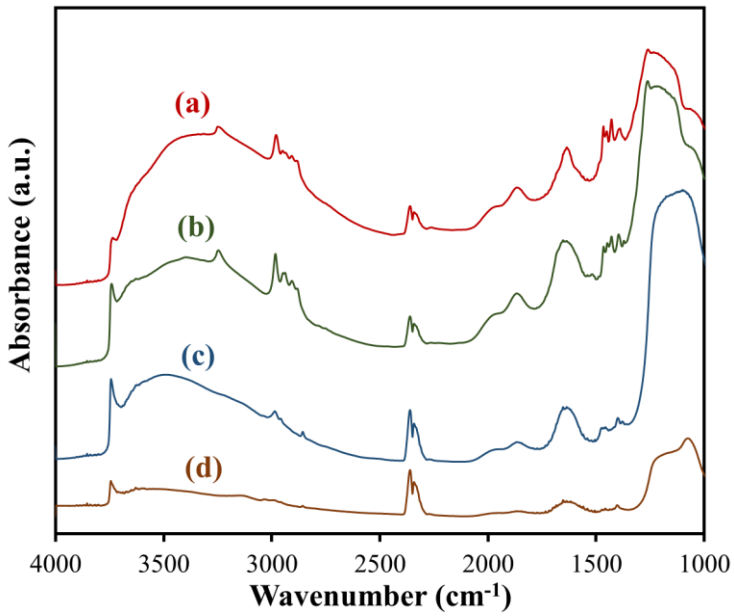

Figure 33. DRIFTS spectra of Co(cyclam)/SBA-15 (a) H-Co(cyclam)/SBA-15 (b) Co(HMD)/SBA-15 (c) and H-Co(HMD)/SBA-15 (d) in powder form. KBr was mixed with each sample and served as the background.

Interestingly, infrared spectra of catalysts before and after BET heating showed very few changes in peaks and peak shapes (Fig. 33). For both samples, sharp peaks around 3740 cm^{-1} represent silanols present on the surface. For Co(cyclam)/SBA-15, these peaks increase in intensity after heating, indicating desorption of the Co(cyclam) complex during the heating process. Additionally, characteristic structural peaks of cyclam are seen at 3300 cm^{-1} (N-H), 3000-2850 cm^{-1} (C-H) and 1500-1350 cm^{-1} (C-C).[95-96] For Co(HMD)/SBA-15, the change in silanol peak height is not as obvious due to the presence of a peak at 3740 cm^{-1} before heating. The presence of these silanol peaks indicates poor surface coverage of catalyst during microwave deposition. Additionally, a reduction in the large absorption peak from 3600-3000 cm^{-1} indicates the loss of surface adsorbed water during heating which in turn also decreases the intensity of the silanol peak. This can be misleading as to if Co(HMD) is desorbing from the surface like Co(cyclam)/SBA-15.

However, structural peaks for both samples are maintained after heating which implies that the catalyst has not degraded. This indicates that the color change may derive from an orientation change of the catalyst on the surface. An orientation change would not show an obvious difference in infrared spectra since structural characteristics are maintained. This is suggested by the lack of new peaks after heating, where degradation would cause the evolution of new species on the surface.

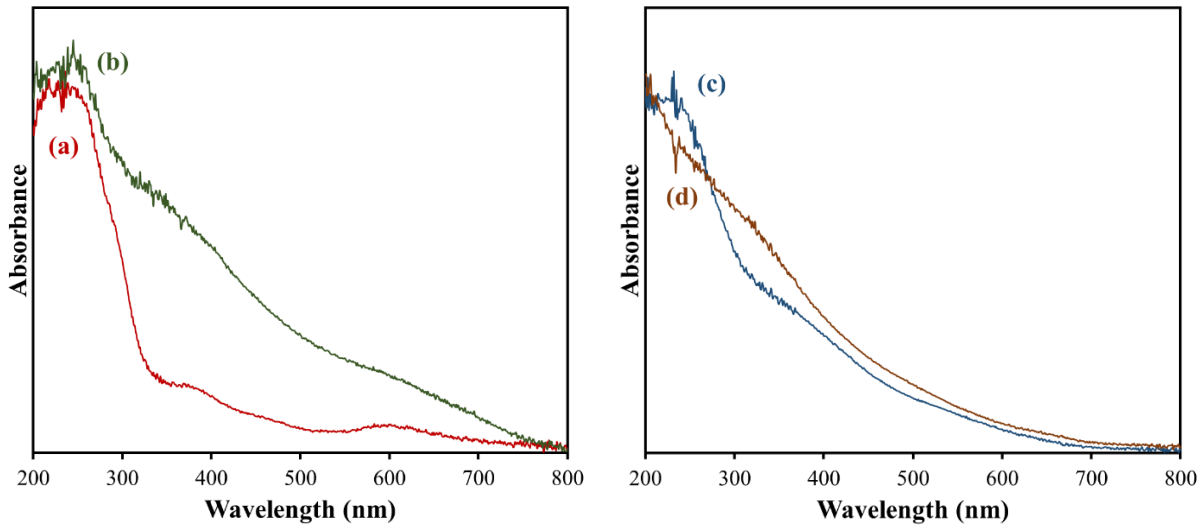

Figure 34. DRUV spectra of Co(cyclam)/SBA-15 (a) H-Co(cyclam)/SBA-15 (b) Co(HMD)/SBA-15 (c) and H-Co(HMD)/SBA-15 (d) in powder form. Barium sulfate served as the background.

DRUV spectra of each sample after heating show an increased absorption in the visible range. The band broadening in this region is associated with the brown color (Fig. 34). Co(cyclam)/SBA-15 shows electron absorption bands around 600 nm and 395 nm associated with d-d transitions in the Co(III) metal ion (Fig. 34 a).[95-96] Upon heating however, these features are covered by the large broad absorption peak between 300-700 nm. This indicates that there are a multitude of structures and configurations of Co(cyclam) throughout the SBA-15 material. This change is not as obvious

for Co(HMD)/SBA-15, where the ligand is initially brown in color, however the same broadening phenomena is seen.

To further confirm that the phenomena are due to configurational changes, ICP-AES was implemented to evaluate cobalt content for each sample. Samples were dissolved in HF for 24 hours and diluted 300-fold prior to analysis. Co(III) content before and after heating did not change substantially, where Co(cyclam)/SBA-15 and H-Co(cyclam)/SBA-15 had loadings of 1.970 and 1.926 µmol/ 10 mg respectively. Co(HMD)/SBA-15 and H-Co(HMD)/SBA-15 had loadings of 1.605 and 1.266 µmol/ 10 mg respectively. This indicates that desorption of Co from the surface is not substantial. Though silanol peaks increased in infrared spectra for heated samples, it was not a direct result of desorbing catalyst. This further supports a configurational change of catalyst complexes on the surface, where possible migration and aggregation is occurring. As complexes aggregate, they would leave behind silanol groups on the surface, which is supported by infrared measurements.

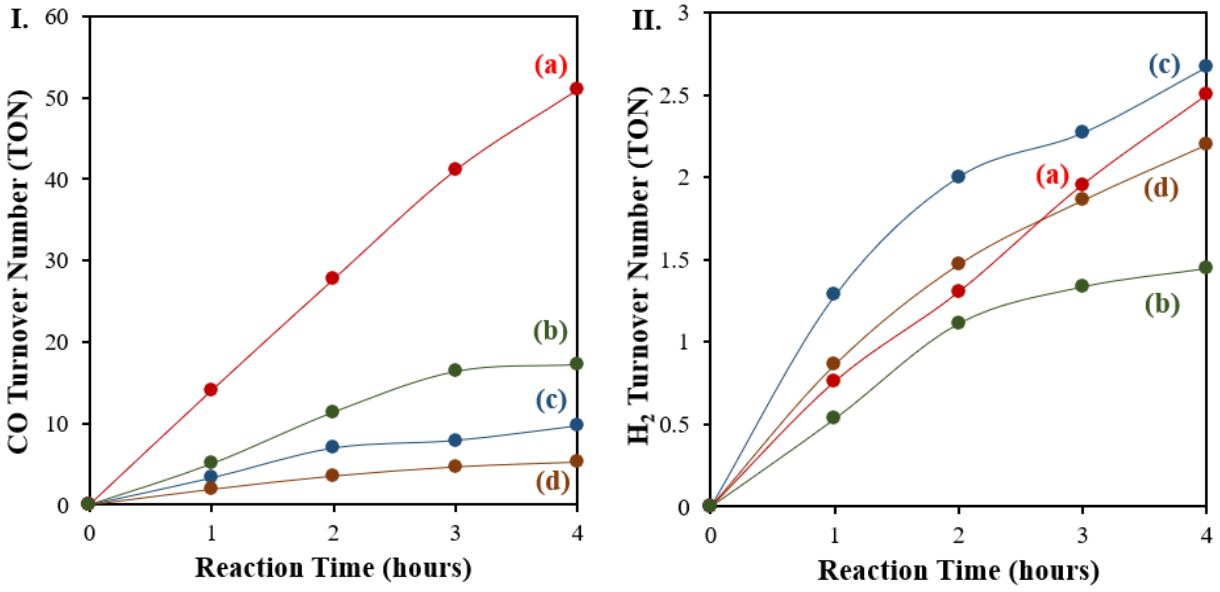

Figure 35. Turnover numbers for CO_2 (I) and H_2 (II) performed with Co(cyclam)/SBA-15 (a) H-Co(cyclam)/SBA-15 (b) Co(HMD)/SBA-15 (c) and H-Co(HMD)/SBA-15 (d). p-terphenyl was used as a photosensitizer and TEOA as an electron donor. Light intensity was 100 mW/cm^2 for all photocatalytic testing.

To evaluate the effect of heating on the photocatalytic activity, each material was irridiated with UV light using TEOA as an sacrificial electron donor and methanol as a proton source (Fig. 35). P-terphenyl was also added as a photosensitizer. CO and H_2 were observed as products for all materials tested. H-Co(cyclam)/SBA-15 and H-Co(HMD)/SBA-15 both showed decreased activity in production for products, suggesting the change in configuration is detrimental to CO_2 reduction efficiency. If heating causes catalytic sites to aggregate, steric hinderance is introduced to the key step of CO_2 binding, thus decreasing CO production. CO produced by Co(cyclam)/SBA-15 decreased by 67% and H_2 TON decreased by 44% after heating. Co(HMD)/SBA-15 activity is decreased more comparatively, most likely due to the sterics from the ligand preventing CO_2 adduct formation which is estabilished in literature.

In order to help understand the configuration of the Co(III) complexes on the surface, a non-porous silica was implemented which has a surface area of 200 m^2/g. This is much lower than SBA-15 and thus during microwave deposition, aggregation or multiple configurational structures are possible using the same amount of Co(III) catalyst. Also a non-porous surface eliminates any diffusion effects, so as catalyst deposits on the surface, aggregation is much more likely. Deposition experiments were repeated using 10 mg of Co(cyclam) and 100 mg of SiO_2. Upon recovery via centrifugation, a brown powder was isolated which are labeled Co(cyclam)/SiO_2. This color was similar to H-Co(cyclam)/SBA-15 further indicating that aggregation or a configurational structure is responsible for the color, not degradation from intense heating.

UV-Vis and infrared spectra are similar between Co(cyclam)/SiO_2 and H-Co(cyclam)/SBA-15 where characteristic peaks of cyclam are obvious (Fig. 36). For UV-Vis spectra of Co(cyclam)/SiO_2, bands associated around 400 and 620 nm which correspond to the d-d transition of Co(III) are visible even through band broadening is present. These features are not as apparent in H-Co(cyclam)/SBA-15 where intense heating could have caused a greater multitude of configurational changes or aggregation versus simply deposition on a small surface. DRIFTS spectra show little differences between the two materials where peaks at 3300 cm^{-1} (N-H), 3000-2850 cm^{-1} (C-H) and 1500-1350 cm^{-1} (C-C) are present (Fig. 36, II).[96] This further asserts the brown coloration is due to configurational changes versus degradation.

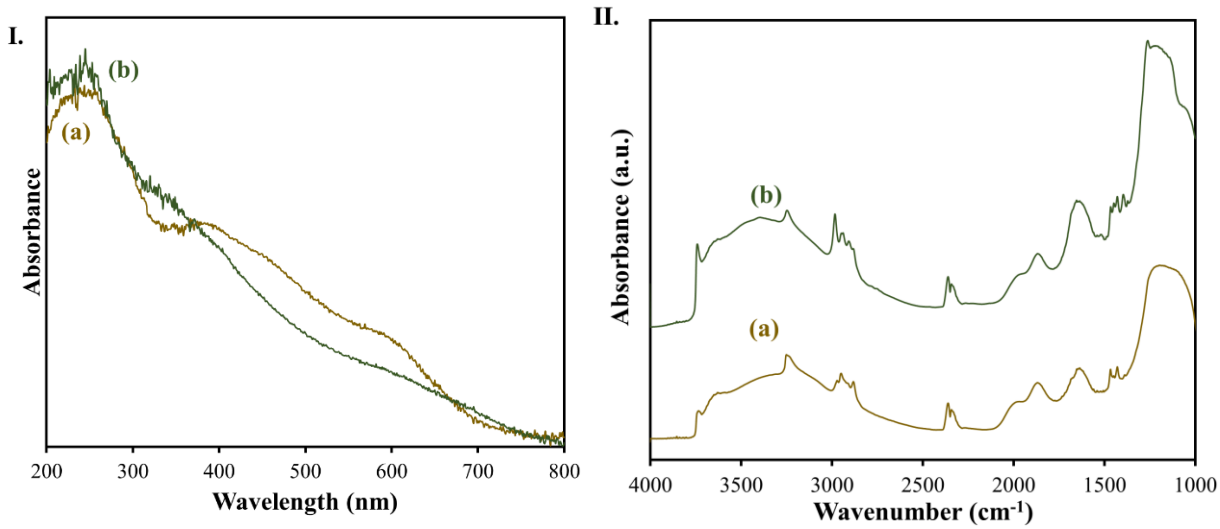

Figure 36. UV-Vis (I) and DRIFTS (II) spectra of Co(cyclam)/SiO_2 (a) and H-Co(cyclam)/SBA-15 (b). For UV-Vis, barium sulfate was used as a background and for infrared, KBr was used.

The Co content of Co(cyclam)/SiO_2 was also tested via ICP-AES to assess the comparability of Co loading on the surface between samples. Co(cyclam)/SiO_2 had a loading of 1.364 µmol/10mg which is a difference of about 0.6 µmol/10 mg from H-Co(cyclam)/SBA-15. This difference is not significant enough to accredit the color to a difference in Co loading. Photocatalysis experiments were then performed with Co(cyclam)/SiO_2 to evaluate the effect on configuration from heating or smaller surface area had on TON. Upon comparison with H-Co(cyclam)/SBA-15, Co(cyclam)/SiO_2 had a much higher TON in CO production and only a slight increase in H_2 TON (Fig. 37). It is not initially clear why there is such a large difference.

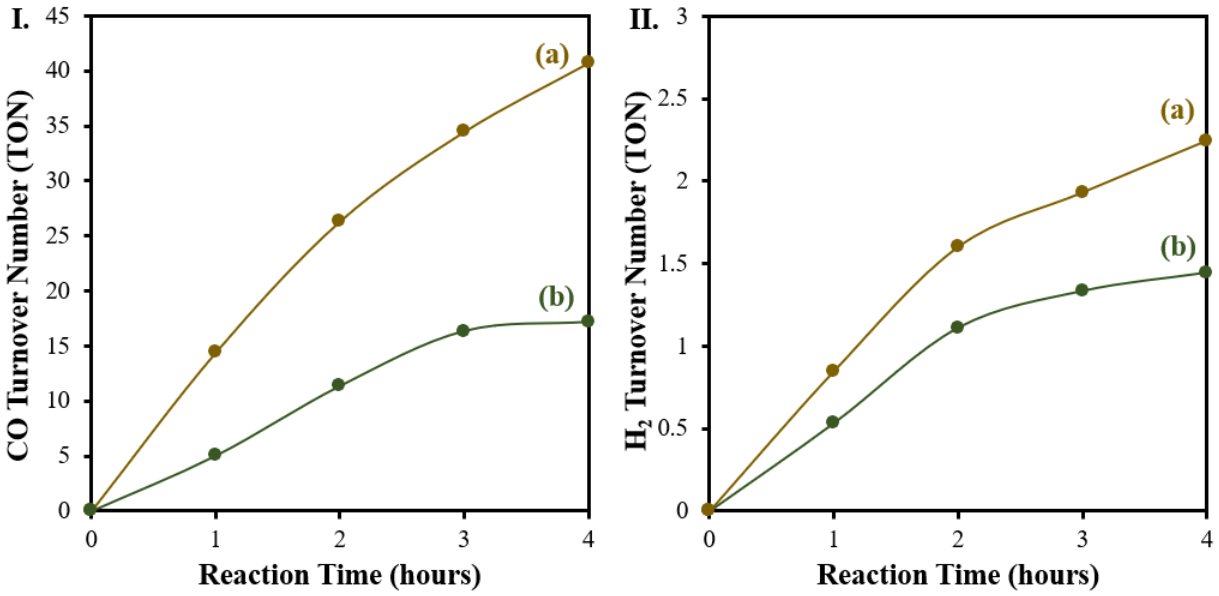

Figure 37. Turnover numbers for CO_2 (I) and H_2 (II) performed with Co(cyclam)/SiO_2 (a) H-Co(cyclam)/SBA-15 (b). P-terphenyl was used as a photosensitizer and TEOA as an electron donor. Light intensity was 100 mW/cm^2 for all photocatalytic testing.

One reason for this difference could be the non-porous structure of the silica, where diffusion of reactants is not an issue leading to a higher TON through diffusion kinetics. Heated samples show a smaller SiO_2 pore size distribution after deposition, thus blocking of pores by aggregated catalyst is likely. Another reason for the difference could result from the heating of the H-Co(cyclam)/SBA-15. Although infrared does not show any structural change, the high temperature could result in a change of oxidation state of the metal. Co(III) is maintained after microwave deposition due to UV-Vis spectra showing characteristic d-d transition bands associated with Co(III). These bands are not seen in UV-Vis spectra of heated samples due to broadening. It is possible Co(III) or Co(II) transition bands are present however they are buried underneath. This change in oxidation state could account for the differences in photocatalytic activity where Co(III) showed the superior product formation.

The uniformity of the Co(cyclam) dispersed on the surface is important to the photocatalytic activity. Co(cyclam)/SBA-15 and Co(cyclam)/SiO_2 both showed superior activity to other samples where uniformity of catalyst deposition on the surface is greater without heating. Any thermal treatment of these catalysts is detrimental. Additionally, the high surface area of SBA-15 versus SiO_2 showed an increased TON of around 10, further demonstrating the importance of uniformity. Heterogeneity caused by heating is detrimental to catalyst performance due to aggregation or polymerization, but the exact configuration on the surface is not obvious. Literature has investigated bridged organic and dimeric Co(cyclam) complex configurations, however characteristics of both do not show similarities to the heated samples.[100-103] Future studies such as XPS could be used to evaluate if oxidation state of Co(III) is maintained after heating to explain why Co(cyclam)/SiO_2 has a brown color, but superior activity to heated samples.

3.4 Summary

Building upon previous work, the deposition of macrocyclic Co(III) was performed via microwave on SBA-15 and non-porous silica. A bulky macrocycle was implemented to observe the negative effects of sterics on photocatalytic activity. All samples were spectroscopically investigated using different techniques and compared. In photocatalysis, Co(cyclam) showed superior activity to Co(HMD) due to the lack of bulky groups preventing CO_2 binding. Through serendipity, it was observed that heating of the catalyst caused a color change. This change is associated with the heterogeneity of the catalyst on the surface where it undergoes configurational changes that are not clear. This heterogeneity is detrimental to catalytic performance and decreases selectivity for CO versus H_2. Low surface area non-porous silica was used as a comparison and showed similar properties however was much more proficient in catalysts. This suggests that heating disrupts

catalyst uniformity to a stronger degree. The presence of uniform catalytic sites on the surface is desirable for superior activity in CO_2 reduction.

The results in this section are published in *Dalton Trans.* **2017**, 46, 10721-10726.

IV. PHOTOCHEMICAL REDUCTION OF CO_2 USING COBALT OXIDE DEPOSITED ON SILICA

4.1 Introduction

Although Co(III) macrocylic complexes have been extensively studied for CO_2 reduction, cobalt oxide (CoOx) materials have not. Instead, CoOx catalysts have been heavily studied for photo water oxidation to convert solar energy into chemical energy.[104-109] Products of solar fuel combustion are CO_2 and water; thus, water is desirable as an electron donor towards CO_2 reduction.[107, 110] A catalyst that can efficiently oxidize water is then inherently needed. CoOx catalysts are attractive for this process due to their robustness in acidic or basic solution and relative abundancy. For example, Iwase and co-workers utilized CoOx loaded BiVO combined in tandem with metal sulfides in a z-scheme catalyst.[111] CoOx was able to successfully generate available electrons from water oxidation and transfer them to the metal sulfide photocathode.

An advantage of this system is the possibility for both water oxidation and CO_2 reduction in tandem for one catalyst. Elimination of materials can save on costs and synthetic time required to make a multi-junction catalyst. The reductive properties of CoOx are not widely studied although studies have shown CO oxidation as a Fischer-Tropsch process.[112] Frei and co-workers have extensively studied CoOx as a photo-induced charge transfer agent in bridged binuclear species.[113-115] CO_2 reduction using this system was achieved utilizing a IrOx nanocluster as a water oxidation catatlyst.[82] CoOx acted as a donor center which then could undergo metal-metal charge transfer (MMCT) with ZrOx to reduce CO_2. Although CoOx was not directly responsible for CO_2 reduction, it is desirable to develop a catalyst that is.

To assist CoOx in CO_2 reduction, instead of coordinating a separate metal complex or nanocluster, cyclam will be added during the reaction. Co(cyclam) is a proven catalyst for CO_2 reduction and has been discussed.[45, 116] By adding cyclam to the reaction, this gives the possibility of *in situ* Co(III) catalyst generation. If small atomic CoOx sites are present, ligand coordination during reaction is possible thus generating an active catalyst like previously studied. Additionally, an *in situ* catalyst decreases the time and cost associated with synthesis. Only a simple microwave deposition of Co(III) is needed eliminating multiple synthetic steps with ligand coordination and purification. This will result in an Co(III) oxide on the surface, where catalysts will be exposed to oxidizing ambient conditions and will not be in reduced form. CoOx will work as a heterogeneous catalyst in tandem with cyclam ligand coordination during photocatalysis.

Additionally, we aim to investigate of the effects of aggregation of the Co(III) catalyst on a surface. CO_2 reduction can be affected by catalytic site depending if it is atomic or aggregated on the surface. Coordination of CO_2 to Co(III) is a key step in catalysis, thus binding differences in high or low loading Co(III) will be investigated. An array of samples will be prepared with varying Co(III) loadings to investigate these loading effects. Also, high and low surface area silica's will be utilized to additionally study the effect of aggregation on the surface. Lower surface area will lead to increased aggregation, due to the diminished amount of surface sites compared to high surface area.

4.2 Experimental

a. Materials

Triethylamine (TEA, ≥99%), triethanolamine (TEOA, ≥99%), acetonitrile (99.999%), p-terphenyl (≥99.5%), and 1,4,8,11-tetraazacyclotetradecane (cyclam, 98%) were obtained from Sigma-Aldrich. Methanol (99.9%) was purchased from Fisher Scientific. Cobalt(II) chloride hexahydrate

(Analytical Reagent) was obtained from J. T. Baker. Ethanol (95.0%) and chloroform (99.8%) were purchased from Parmo Products Inc. All reagents were used without further purification. Non-porous fumed silica (Aerosil 200, specific surface area ~200 $m^2 g^{-1}$, average primary particle size ~12 nm) was obtained from Evonik and used as received.

b. Synthesis

Microwave-assisted deposition of CoOx onto SBA-15/Silica

To deposit $CoCl_2$ via microwave synthesis, 100 mg SBA-15 was initially dried at 100°C for in an oven one hour before use. The dried material was then mixed with 1 mg $CoCl_2$ and 65 µL triethylamine in 7.5 mL acetonitrile. The mixture was sealed in a capped reaction vessel, which was then placed in a CEM Discover single-mode microwave reactor and underwent reaction at 80°C for 2 hours. After the microwave reaction, the mixture remained green in color. The resulting precipitate was recovered by centrifugation in acetonitrile and washed 2 times each with chloroform and ethanol. After drying at room temperature, the CoOx catalyst deposited on SBA-15 was obtained as a white powder denoted as "CoOx/SBA". This process was repeated for a varying amount of $CoCl_2$ loadings as well as utilizing non-porous silica as a support material. Non-porous silica materials are denoted as "CoOx/SiO_2". Loadings prepared for each silica support material include, 1 mg, 2 mg, 5 mg, 10 mg, and 20 mg of $CoCl_2$ used.

c. Characterization

A Cary 50 Bio spectrophotometer equipped with a Barrelino diffuse reflectance probe was used to obtain the UV–visible spectra of powder samples using $BaSO_4$ as a background. The surface area, pore size distribution and total pore volume of mesoporous materials were measured on a NOVA 2200s Surface Area and Pore Size Analyzer. Scanning electron microscopy (SEM) images were

obtained on an Amray 3300FE field emission SEM with a PGT Imix-PC microanalysis system. Infrared spectra were collected on a Thermo Nicolet 6700 FTIR spectrometer equipped with a Harrick Praying Mantis diffuse reflectance accessory. Elemental analysis was conducted by acid digestion of the synthesized catalysts, followed by quantification using a Varian Vista AX inductively coupled plasma atomic emission spectrometer.

d. Photocatalytic CO_2 Reduction

In photochemical CO_2 reduction, p-terphenyl was employed as a molecular photosensitizer while a mixture of TEOA and methanol was used as sacrificial electron donors. In a typical photocatalysis experiment, 1 mg of catalyst was dispersed in a 4.0 mL acetonitrile solution containing p-terphenyl, TEOA and methanol (acetonitrile: TEOA: methanol 4:1:1 v/v) in a quartz test tube. Prior to photocatalytic testing, the reaction suspension was bubbled with CO_2 (99.999%, Airgas) in the dark for 20 min, and then irradiated with a 200 W mercury lamp equipped with a water filter. The light intensity of the reaction solution was fixed at 100 mW/cm^2. The head space above the reaction solution was sampled with a gas-tight syringe at different time intervals for product analysis using an Agilent 7820 GC equipped with a TCD detector and a 60/80 Carboxen-1000 packed column (Supelco).

4.3 Results and Discussion

To study the possibility of *in situ* Co catalyst generation, CoOx/SBA-15 and CoOx/SiO_2 samples were successfully synthesized via microwave deposition. SiO_2 and SBA-15 are implemented as solid supports with varying surface area to investigate the effect of aggregated surface sites. Atomic catalytic sites are more desirable to help facilitate cyclam coordination like homogeneous Co(cyclam) analogues. Additionally, an array of sample loadings for both support materials are

investigated to further probe the effect of aggregation on the surface. Low loading Co samples on high surface area SBA-15 are the most likely to have atomic CoOx sites, whereas vice versa with SiO_2 for clusters.

Sample	Co Loading (µmol/mg)	Sample	Co Loading (µmol/mg)
1 mg CoOx/SBA-15	0.040	1 mg CoOx/SiO_2	0.071
2 mg CoOx/SBA-15	0.062	2 mg CoOx/SiO_2	0.107
5 mg CoOx/SBA-15	0.211	5 mg CoOx/SiO_2	0.242
10 mg CoOx/SBA-15	0.405	10 mg CoOx/SiO_2	0.336
20 mg CoOx/SBA-15	0.686	20 mg CoOx/SiO_2	0.330

Table 2. Elemental Analysis loadings for silica and SBA-15 samples. Elemental Co content is reported as µmol/mg.

ICP-AES was implemented to study the loadings of each support material and are shown in table 2. Samples with less $CoCl_2$ precursor used showed similar Co loadings regardless of the support material utilized. SBA-15 and SiO_2 only show a difference of 0.031 µmol/mg for 1 mg of precursor used, thus comparable. Interestingly as the amount of precursor used for SiO_2 samples, the amount of Co deposited levels off (Fig. 38). This indicates that the low surface area of the support is saturated for amounts after 10 mg of precursor is used. This also implies that the high loading SiO_2 sample will have more nanoclusters than other materials. Conversely, as precursor used amount increases for SBA-15 samples, Co content continues to increase.

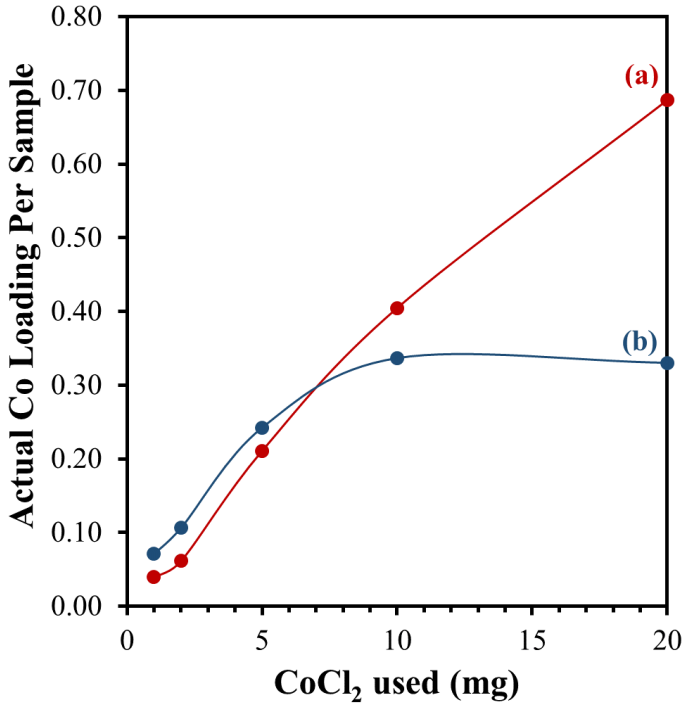

Figure 38. Co loadings of SBA-15 (a) and SiO_2 (b) materials versus the amount of precursor used. Actual loadings are in µmol/mg.

DRUV of each material shows as characteristic Co(III) d-d transition peaks around 400 and 600 nm (Fig. 39 and 40). These peaks are not as intense for lower loadings of Co material and increase in definition due to the concentration of Co(III) increase. As continued concentration increases, peak broadening also does where samples 10 – 20 mg of Co(II) precursor have the most broadening. Additionally, SiO_2 samples show broadening at lower loadings, indicating aggregation due to the lower surface area of the support material (Fig. 40). As continued Co(III) loading increases, definition of d-d transition bands decreases for both samples. Additionally, SiO_2 samples do not show d-d band definition indicating aggregation of Co(III) sites on the surface. The large porous network of SBA-15 prevents this aggregation, thus band definition is move visible.

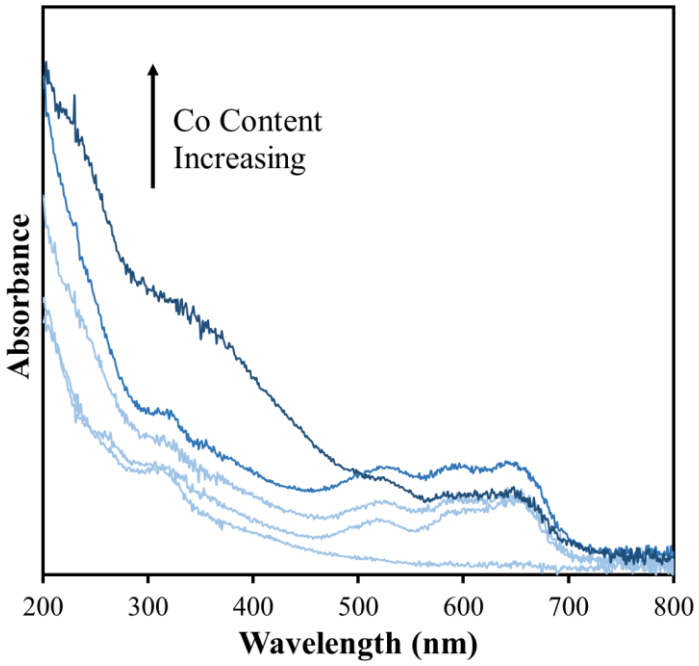

Figure 39. DRUV of 1 mg CoOx/SBA-15 (a) 2 mg CoOx/SBA-15 (b) 5 mg CoOx/SBA-15 (c) 10 mg CoOx/SBA-15 (d) and 20 mg CoOx/SBA-15 (e). Barium sulfate was used as the background.

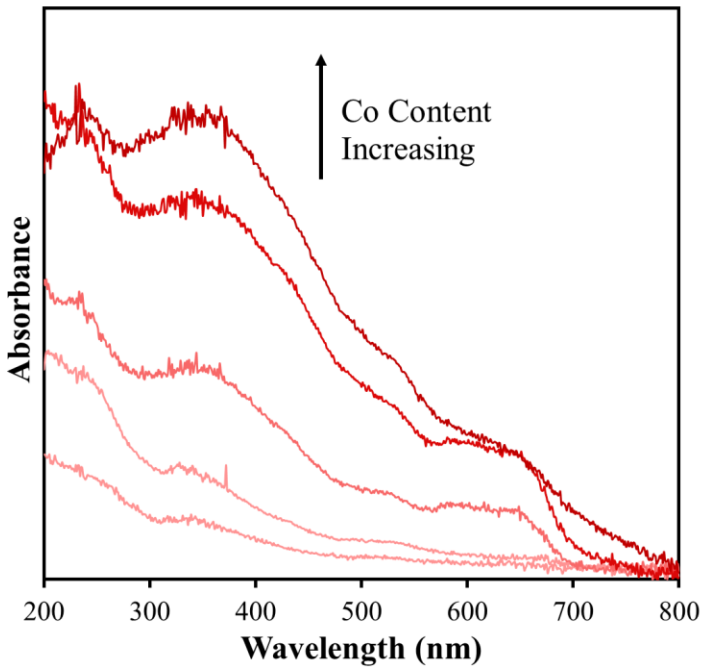

Figure 40. DRUV of 1 mg CoOx/SiO_2 (a) 2 mg CoOx/SiO_2 (b) 5 mg CoOx/SiO_2 (c) 10 mg CoOx/SiO_2 (d) and 20 mg CoOx/SiO_2 (e). Barium sulfate was used as the background.

The synthesized CoOx materials were tested in photocatalysis in the presence of CO_2 and TEOA as a sacrificial electron donor (Fig. 41). P-terphenyl was utilized as a photosensitizer. Cyclam was added to each photocatalytic reaction to generate the *in situ* active catalyst. Each experiment was performed in triplicate to establish trends and reduce variability. Note that plots show actual loading of each sample, not the amount of precursor used. For CoOx/SBA-15 materials, 1 mg CoOx/SBA-15 obtained a TON of 73 and decreased as loading increased to 8 for 20 mg CoOx/SBA-15. Conversely, $CoOx/SiO_2$ samples showed relatively poor performance with 1 mg $CoOx/SiO_2$ obtaining a TON of 8 and 20 mg $CoOx/SiO_2$ obtaining a TON of 15 respectively. This demonstrates that atomic sites are more efficient than aggregated sites due to low surface area or high loading. However, the large drop off for CoOx/SBA-15 materials in catalytic efficiency is not immediately clear but can be related to cluster formation as loadings increase. Additionally, $CoOx/SiO_2$ catalysts show no discernible trend and catalytic efficiency increases for higher loading. This most likely results from initial cluster formation at low loadings due to the low surface area. As the amount of Co increases, the TON in turn also increases due to more nanoclusters available as catalytic sites. Control experiments were performed in the absence of photosensitizer or cyclam and showed little to no CO production. Additionally, if CoOx catalyst is not present in the photoreaction, very little CO is produced.

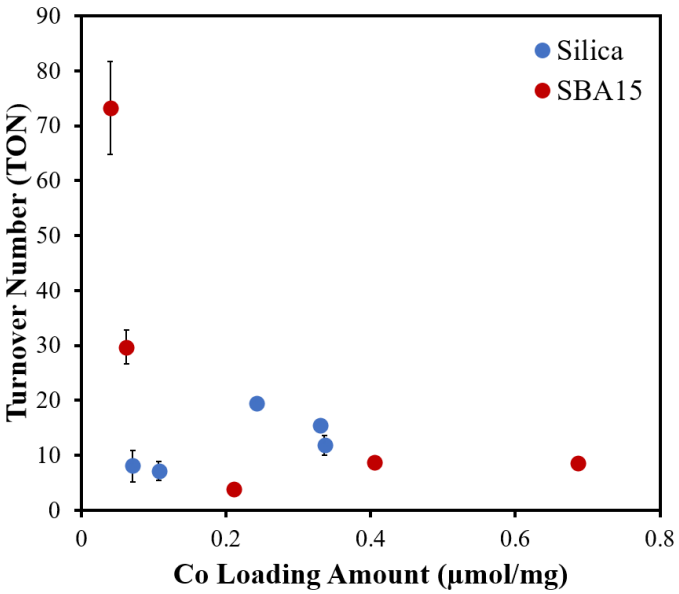

Figure 41. CO TON for CoOx SBA-15 and SiO_2 materials after 2 h of irradiation. P-terphenyl was used as a photosensitizer and TEOA as an electron donor. Light intensity was 100 mW/cm^2 for all photocatalytic testing.

The amount of CO produced for each sample is shown in Figure 42 to help evaluate trends reported. For CoOx/SBA-15, low loading samples show 1.8 – 2.2 µmol of CO produced which decreases as loading increases. As loading increases further however, the µmol of CO produced also increases. This indicates that initially low loading CoOx/SBA-15 samples are more active for CO_2 reduction and as Co loading increases, the amount of CO produced increases as well due to more available sites present. CoOx/SiO_2 shows a similar trend however with a lower amount of CO produced, 0.6 – 0.8 µmol. As loading increases so does CO produced increases like that of CoOx/SBA-15 samples. This indicates that surface area of support material is important in facilitating active Co sites where higher surface areas showed increased TON's and CO µmol produced.

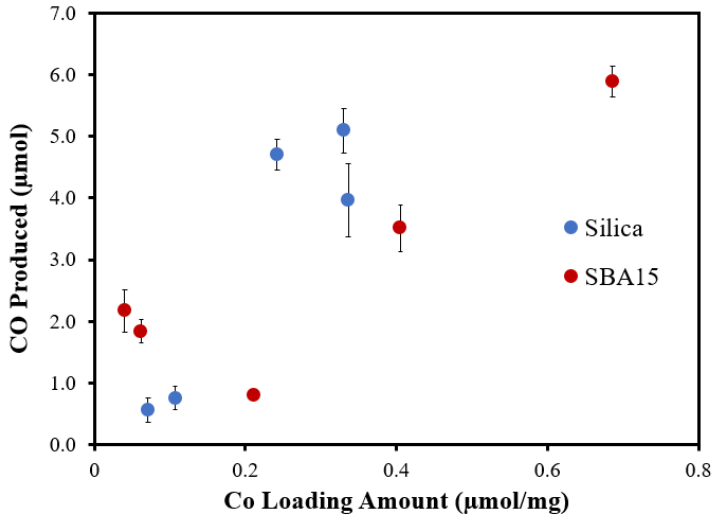

Figure 42. CO µmol produced for CoOx SBA-15 and SiO_2 materials after 2 h of irradiation.

Surprisingly, low loading CoOx/SBA-15 showed a higher TON than Co(cyclam)/SBA-15 studied previously which had a CO TON of 51. Cyclam coordination to a catalytic site requires kinetic steps whereas Co(cyclam) materials do not, which should comparatively increase catalytic efficiency. However higher TONs were achieved with 1 mg CoOx/SBA-15. One possible explanation is leaching of Co(III) from the surface of SBA-15 and coordination with cyclam in solution. This would prevent any surface steric interactions as well as adjacent aggregation from other Co(III) nanoclusters. To probe this, 1 mg CoOx/SBA-15 and 20 mg CoOx/SBA-15 were each dispersed in 4 mL acetonitrile with equivalent by weight cyclam. Each solution was stirred at room temperature in atmospheric gas headspace. Solids were recovered via centrifugation and supernatant of each were collected. Supernatants were tested in transmission UV-Vis utilizing acetonitrile as a background (Fig. 43). For 1 mg CoOx/SBA-15 only a slight absorbance around 300 nm is observed, whereas 20 mg CoOx/SBA-15 shows a strong absorbance around 315 nm. Additionally, closer inspection from 350 – 800 nm, two additional bands are present at 450. and 650 nm. These bands are attributed Co(cyclam) where Co leached from the surface coordinates to

cyclam *in situ*. It is possible that Co is also leaching for 1 mg CoOx/SBA-15 and has the same effect, however it is not observed due to the low loading.

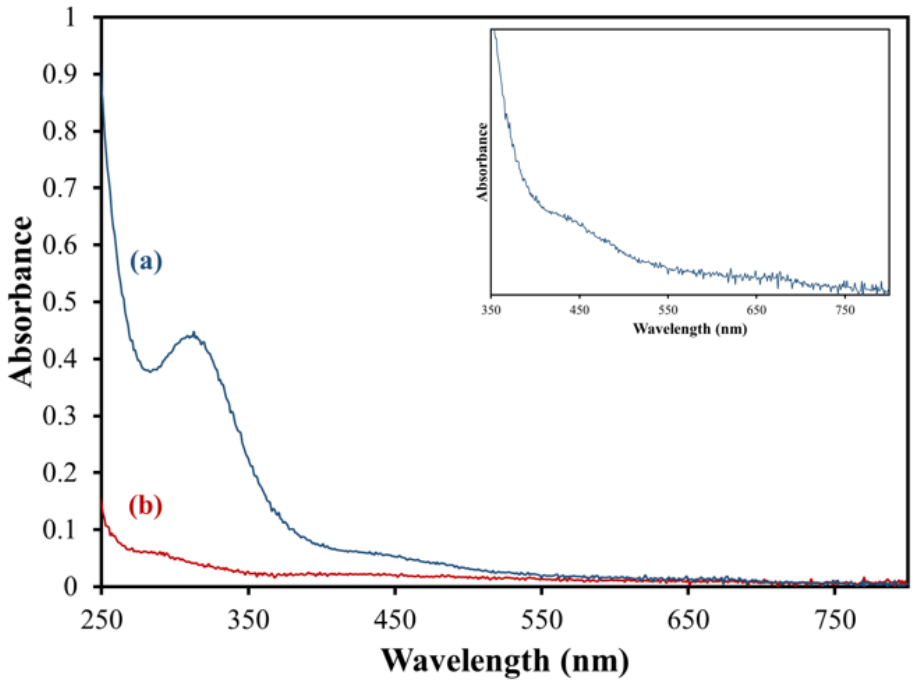

Figure 43. Transmission UV-Vis of supernatant from 20 mg CoOx/SBA-15 (a) and 1 mg CoOx/SBA-15 (b). Acetonitrile was used as a background.

Recovered powder samples also were analyzed via DRUV and optical spectra acquired (Fig. 44). For each sample the transition bands associated with Co(III) decreased in intensity comparatively. In particular, 20 mg CoOx/SBA-15 showed a decrease in intensity associated with the d-d transition bands from 600 – 700 nm. This further supports evidence that Co is desorbing from the silica support under photocatalytic conditions. This however does not explain the large difference in µmol of CO produced between the two samples. 20 mg CoOx/SBA-15 has a Co loading that is 17 times that of 1 mg CoOx/SBA-15 however only produced 3 times more µmol of CO. Leaching of Co is apparent but does not provide a complete explanation of efficiency differences.

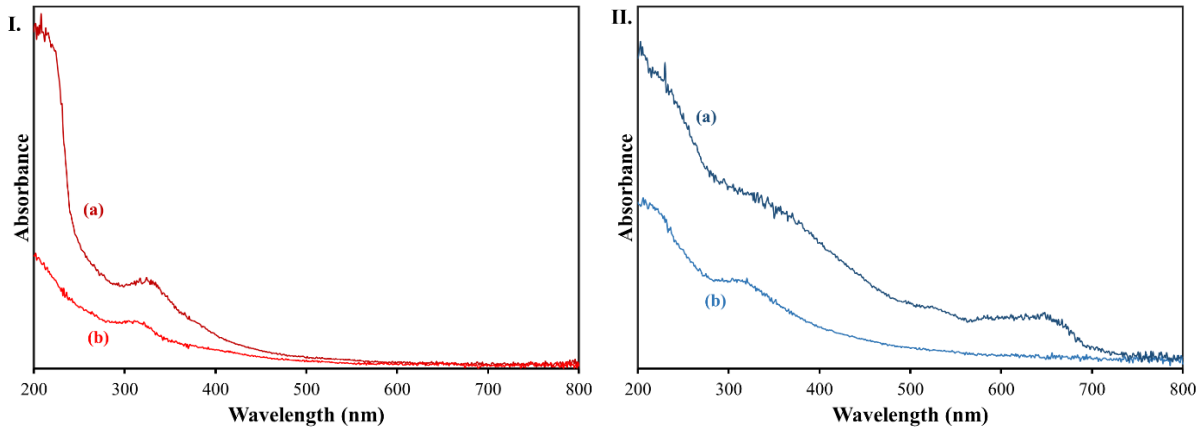

Figure 44. DRUV of 1 mg CoOx/SBA-15 (I) and 20 mg CoOx/SBA-15 (II). Before (a) and after (b) stirring with cyclam in acetonitrile. Barium sulfate was used as the background.

To probe surface coordination DRIFTS spectroscopy was also utilized to analyze samples before and after stirring with cyclam (Fig 45.). Before stirring each sample shows a peak around 3700 cm^{-1} corresponding to Si-OH groups on the surface, indicating incomplete surface coverage. This demonstrates the high surface area silica has more available sites for deposition, thus loading did not level off as precursor was used. For both samples after stirring, a large magnitude of organic peaks is seen in both. These peaks correspond to cyclam on the surface of the material, ranging from 3500 – 2700 cm^{-1} (C-H) and 1600 – 1000 cm^{-1} (C-C, N-H). They do not correspond to acetonitrile due to each sample being vacuumed dried extensively before analysis. It is not clear if these peaks however are indicative of cyclam coordination to Co(III) sites on the surface.

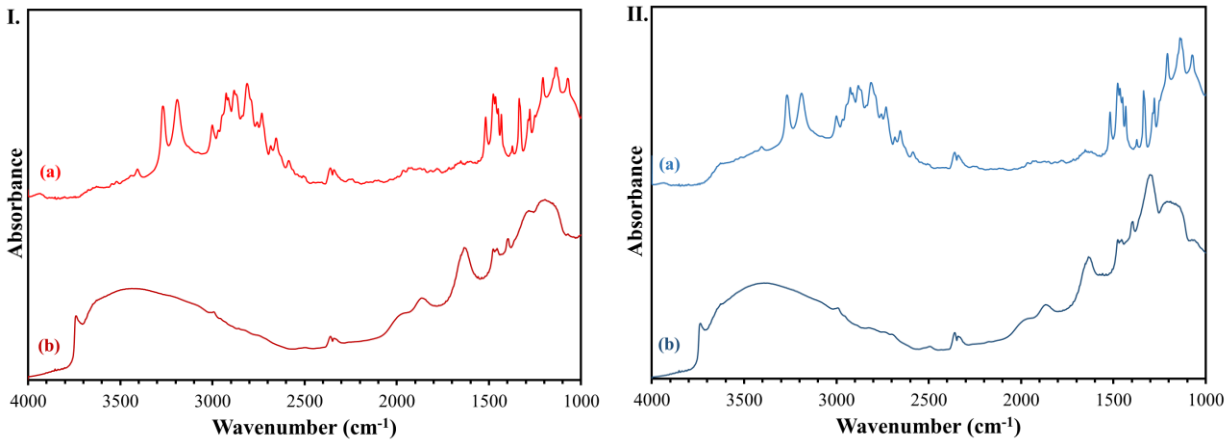

Figure 45. DRIFTS of 1 mg CoOx/SBA-15 (I) and 20 mg CoOx/SBA-15 (II). After (a) and before (b) stirring with cyclam in acetonitrile. KBr was used as the background.

During photocatalysis it is possible that there is a mixture of events occurring regarding cyclam and CoOx. First some Co(III) is desorbing from the surface under light irradiation and coordinating to cyclam in solution phase. Additionally, cyclam is coordinating to the surface to either CoOx or SiO_2. Silanol peaks are not observed after mixing with cyclam, indicating complete surface coverage with introduction of the ligand. In combination both active sites on the surface and in solution contribute to the reduction of CO_2. Surface coordination however appears to be the more active catalyst, where samples with low loadings still produce comparable µmol of CO to samples with high loadings.

CoOx clusters on SiO_2 have been investigated for water oxidation catalysis where the desorption of clusters did not occur.[104, 117] Frei et al. attributed this to support stabilizing cluster formation, however deposition methods are different from this work.[104] It is possible their cluster synthesis method generates a more stable surface cluster. CoOx/SiO_2 shell structures also demonstrated excellent stability in water and high temperature.[118-120] Future studies could investigate different deposition methods of CoOx for smaller nanoclusters to improve stability. Additionally, future

studies such as XPS or EDX could be utilized to evaluate the oxidation state of Co on the surface before and after photoreaction. These studies could help elucidate if cyclam is coordinating to Co sites on the surface versus SiO_2.

4.4 Summary

CoOx was successfully deposited on both high and low surface area SiO_2 supports. Elemental loading of CoOx was shown to be dependent on the amount of surface area available for deposition. Introduction of cyclam during photocatalysis demonstrated excellent production of CO with *in situ* catalyst generation. Low loading materials of CoOx showed increased photoactivity versus high loading. Unfortunately, Co desorption from the support material is apparent and is counter-productive to catalyst design. Additionally, the coordination of cyclam to clusters is not well understood and future efforts are required.

V. INFRARED STUDIES OF CO/CO_2 ADSORPTION ON Cu/TiO_2 AND Sn/TiO_2

5.1 Introduction

Cu as a co-catalyst with TiO_2 has been investigated due to its promise and ability for CO_2 reduction. The loading and morphology of Cu on TiO_2 however has significant effect on the catalytic properties of the material.[63-64] This also has been observed for Cu/ TiO_2 catalysts in other experiments such as organic molecule degradation.[121-122] To evaluate loading effects, Deskins and co-workers utilized DFT studies to investigate the effect of CO_2 activation over TiO_2-supported Cu clusters ranging in size of 1-4 atoms. For CO_2 to be activated, transition from linear to bent is required, and all Cu clusters stabilized bent CO_2 adsorption where the Cu dimer was the most stable. Demonstrating that lower loading and smaller clusters of Cu are more active for CO_2 reduction.[123] The active sites for bent CO_2 adsorption also predominantly had oxidation states of 0 and +1. Also indicating that Cu(II) synthesis methods may be undesirable in catalyst design.

Sn has also been studied as a co-catalyst with Cu for CO_2 reduction. The synergistic effects are not completely understood between Cu and Sn. Li and co-workers investigated a core/shell structure of Sn and Cu while varying thickness of SnO_2 on Cu nanoparticles.[124] The thickness of Sn affected selectivity of products where thicker layers (1.8 nm) produced formate and thinner layers (0.8 nm) produced CO. DFT studies showed thinner shells of SnO_2 alloying with Cu, compressing the lattice structure of SnO_2. This further demonstrates the strong influence of surface structure on catalysis.

Previously, our group has studied CO_2 reduction utilizing a Sn reduction method to deposit Cu on TiO_2.[125] This procedure allows for high dispersity of Cu sites, where aggregation and layered Cu

is prevented through atomic substitution. These composites demonstrated significantly higher activity than TiO_2 alone, attributed to stabilization of CO_2 on the surface by Cu. Computational studies additionally supported this enhancement where CO_2 binding without Cu present has a much weaker binding energy. CO was also found to bind strongly to Cu^+ sites; however their binding properties between interfacial sites were not investigated. Additionally, Sn was used in excess for deposition of Cu and most likely played a role in CO_2 reduction however it was not investigated.

In this study we aim to help understand the mechanism of CO_2 reduction on Cu(Sn)/TiO_2 through CO adsorption studies with H_2 and Ar heating, where Cu(Sn) indicates Cu deposition via Sn substitution. Composites of Sn/TiO_2 and Cu/TiO_2 will also be studied for comparison. CO adsorption studies can indicate the type of bonding character CO has when adsorbed the surface with characteristic infrared absorptions. This information can elucidate possible intermediates of CO_2 reduction. Previously it was shown that low loadings of Cu on TiO_2 have greater TON efficiency, thus CO_2 reduction likely is occurring at an interfacial site. CO adsorption studies can probe possible dimeric or trimeric interactions to support this hypothesis. Additionally, the role of Sn will be investigated in order to probe if CO/CO_2 binding is occurring between metal sites during catalysis.

5.2 Experimental

a. Materials

A commercial TiO_2 material, Aeroxide P25 (specific surface area 57 m^2/g, average particle size ~25 nm, phase composition ~80% anatase and 20% rutile) was obtained from Evonik. Tin(II) chloride dihydrate ($SnCl_2 \cdot 2H_2O$, ACS reagent) and copper(II) chloride ($CuCl_2$, 99.999% trace metals basis) were obtained from Sigma-Aldrich. Ar (Ultra High Purity), CO (99.999%) and CO_2 (99.999%) were obtained from Airgas.

b. Synthesis

Preparation of Sn^{2+} nanocomposite (Sn/TiO_2)

In a typical synthesis, 400 mg P25 TiO_2 was initially dried at 100^oC two hours before use. The dried P25 TiO_2 was then dispersed in 20 mL milli-q water and was mixed with a 20 mL solution of 0.09 M HCl and 400 mg of $SnCl_2 \cdot 2H_2O$. The mixture turned yellow immediately upon mixing with the acidic Sn^{2+} solution. This mixture is then stirred for 10 minutes under ambient conditions. The Sn/TiO_2 nanocomposite is then isolated via centrifugation and washing with water. The product was dried at 80^oC for several hours and the yellow powder acquired was denoted Sn/TiO_2.

Preparation of Cu^0 nanocomposite ($Cu(Sn)/TiO_2$)

To remove water from the surface, 200 mg Sn/TiO_2 was initially dried at 100^oC one hour before use. The dried Sn/TiO_2 was then dispersed in 20 mL milli-q water and 10 mg $CuCl_2$ was added. The mixture turns light blue immediately upon addition of the Cu precursor. This mixture is then stirred for 5 hr covered with parafilm under ambient conditions. The $Cu(Sn)/TiO_2$ nanocomposite is then isolated via centrifugation and washing with water. The product was dried at 80^oC for several hours and the light blue powder acquired was denoted $Cu(Sn)/TiO_2$.

Preparation of Cu/TiO_2 nanocomposite

In a typical synthesis, 200 mg P25 TiO_2 was initially dried at 100^oC one hour before use. The dried P25 TiO_2 was then dispersed in 20 mL milli-q water and 10 mg $CuCl_2$ was added. The mixture turns light blue immediately upon addition of the Cu precursor. This mixture is then stirred for 5 hr covered with parafilm under ambient conditions. The Cu/TiO_2 physiosorbed nanocomposite is then isolated via centrifugation and washing with water. The product was dried at 80^oC for several hours and the light blue powder acquired was denoted Cu/TiO_2.

c. Characterization

A Cary 50 Bio spectrophotometer equipped with a Barrelino diffuse reflectance probe was used to obtain the UV–visible spectra of powder samples using $BaSO_4$ as a background. Infrared spectra were collected on a Thermo Nicolet 6700 FTIR spectrometer equipped with a Harrick Praying Mantis diffuse reflectance accessory.

d. Infrared Studies

For a typical infrared adsorption study, the sample is loaded in the DRIFTS cell with KBr as a background. Samples are pressed on top of a KBr pellet and not ground with the background material. The cell is then covered from ambient light conditions and purged with Ar for 20 min. The cell is then heated to 200^{o}C for 1 hr under H_2 or Ar flow. The sample is cooled to room temperature, then CO_2 or CO is purged through the cell for 30 min. Ar is then again purged to evacuate any gaseous CO or CO_2 in the headspace. At each point infrared scans are performed.

5.3 Results and Discussion

For this study, Cu(Sn)/TiO_2 and Sn/TiO_2 nanocomposites were successfully synthesized to probe the mechanism of CO_2 reduction via infrared studies. Sn is deposited onto P25 TiO_2 to form the Sn/TiO_2 nanocomposite. Cu^{2+} is added to Sn/TiO_2 and undergoes reductive substitution with Sn^{2+} sites to form Cu^0/TiO_2 nanocomposites. Cu/TiO_2 from physisorption of Cu onto the TiO_2 acts as a comparison to evaluate the effect of Sn presence for the Cu(Sn)/TiO_2 nanocomposite. The presence of Cu and Sn for these nanomaterials was confirmed with DRUV (Fig. 46). P25 TiO_2 does not absorb light in the visible region and this is consistent with its large bandgap. Sn/TiO_2 shows broadening from 350 to 550 nm, corresponding to the charge transfer between the valence band of TiO_2 to Sn^{2+}. Cu/ TiO_2 shows a similar band broadening from the TiO_2 indicating similar electron transfer. Additionally, there is a large absorption from 600-800 nm which is attributed to the d-d

transition of Cu^{2+}. These absorption bands indicate that the deposited Cu is oxidized from the expected reaction with Sn^{2+}. TiO_2 has oxidizing properties and it is possible upon deposition Cu exists as CuO on the surface rather than atomic Cu^0.

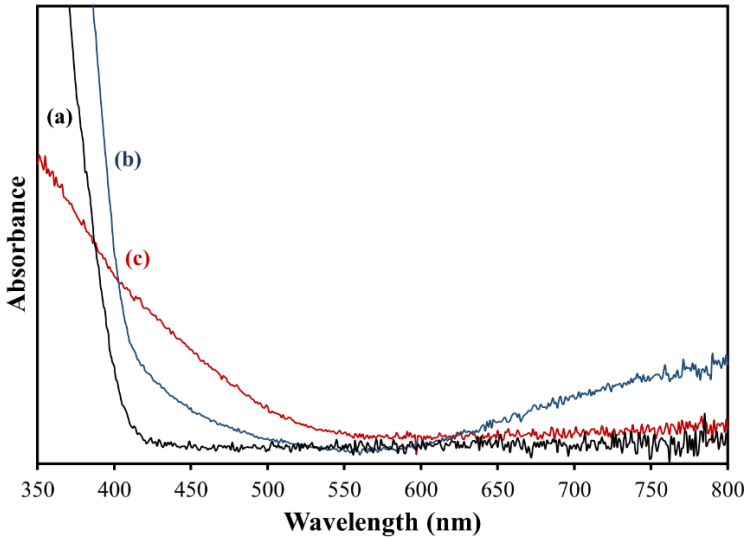

Figure 46. DRUV spectra of P25 TiO_2 (a) Cu(Sn)/TiO_2 (b) and Sn/ TiO_2 (c) in powder form. Barium sulfate served as the background.

To evaluate surface coverage and purity of material, infrared spectra of each sample were acquired using DRIFTS (Fig. 47). Each sample shows the lack of characteristic carbon stretches both in the 3000 cm^{-1} and 1600 cm^{-1} region, indicating pure metal oxide samples without organics. A characteristic Ti-OH peak appears around 3600 cm^{-1} but disappears for the nanocomposite materials indicating surface coverage of the Cu and Sn material on TiO_2. The adsorption at 1600 cm^{-1} represents the bending mode of Ti-H_2O on the surface where atmospheric water is adsorbed onto each surface.[126] These materials are not calcined to prevent surface catalyst aggregation; thus the presence of water adsorbed is expected.

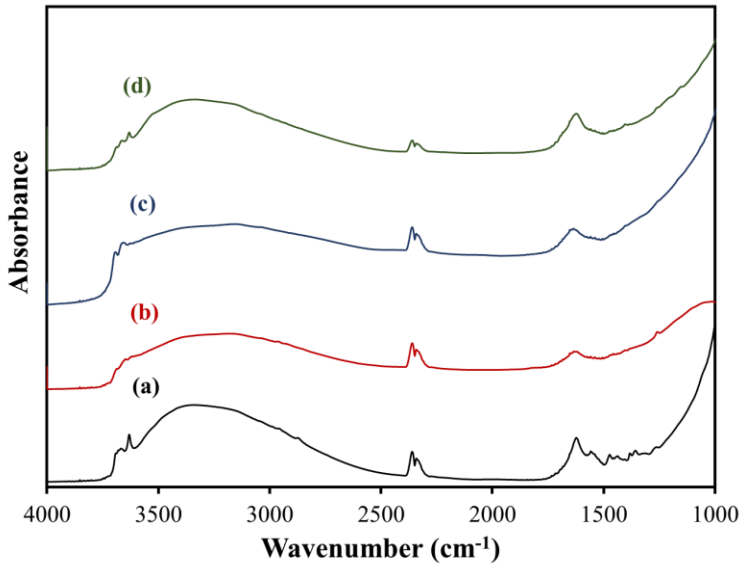

Figure 47. DRIFTS spectra of P25 TiO_2 (a) Sn/TiO_2 (b) $Cu(Sn)/TiO_2$ (c) and Cu/TiO_2 (d) in powder form. KBr was mixed with each sample and served as the background.

Since each sample is likely oxidized upon deposition onto P25 TiO_2, samples were heated under H_2 flow as a reducing environment to counteract the oxidation of materials before introduction of CO. Additionally, since atmospheric water is seen in infrared spectra, samples will also be heated under Ar and compared to see the effect of water or H_2. Each infrared trace is taken after samples have returned to room temperature. Figure 48 shows the subtraction spectra for samples heated under the reducing atmosphere of H_2. P25 TiO_2 shows no adsorption of material however all other samples have multiple adsorbed species. Cu/TiO_2 nanocomposites show peaks at 2120 cm^{-1} which is attributed to CO bound to Cu^+ sites, however slightly shifted from literature values, most likely due to interaction with one or multiple Cu^+ sites. This also demonstrates the strong oxidizing nature of the TiO_2 surface, where CO-Cu^0 was not observed even under reductive treatment. Interestingly, Sn/TiO_2 shows multiple adsorbed species that have not been observed before in literature. These species are all attributed to CO bound to Sn on the surface, however their adsorbed structure is not clear. These peaks are only present when Sn/TiO_2 is exposed to CO, thus their assignment. It is

possible that CO and dicarbonyl species adsorbed both exist as well as CO species bonded to multiple Sn^{2+} or Sn^{1+} sites. These species do not exist for Cu/TiO_2 nanocomposite where Sn is absent further asserting them as CO bound to Sn^{+}. Additionally, these peaks are shifted upon the introduction of Cu for the $Cu(Sn)/TiO_2$ nanocomposite. This demonstrates that Sn is not removed upon Cu coordination and can have possible binuclear interactions between the catalytic sites. This is further supported by shifting in CO-Sn peaks such as 2048 cm^{-1} demonstrating the influence of Cu towards Sn on the surface. New peaks that form on this nanocomposite could be attributed to CO bound to both Sn and Cu.

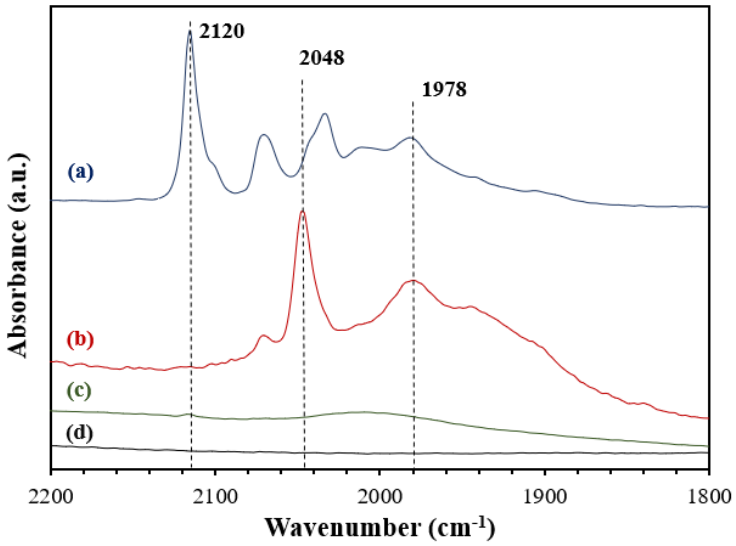

Figure 48. Differencespectra of CO adsorbed on H_2 heated $Cu(Sn)/TiO_2$ (a) Sn/TiO_2 (b) Cu/TiO_2 (c) and P25 TiO_2 (d) in powder form. KBr was mixed with each sample and served as the background. CO was flowed over each sample for 30 min then the cell was sealed.

To help evaluate the assignments to the $CO\text{-}Sn/TiO_2$ species, infrared temperature programmed desorption (IR-TPD) studies were employed (Fig. 49). CO adsorption with H_2 heating was performed then the cell was sealed and incrementally heated to 50°C, 100°C and 150°C for 30 min. After each temperature ramp, the cell was cooled to room temperature and spectra were acquired.

Initial spectra show multiple CO-Sn species present however decrease over as temperature increases. The peak at 2071 cm^{-1} disappears almost completely after 50°C temperature atmosphere indicating weakly bound CO species. Other indistinguishable peaks disappear at 50°C leaving only bound species at 2048 and 1978 cm^{-1}. These species correspond to more strongly bond CO leading to possible assignments as CO bound to multiple Sn^{2+} sites. Dicarbonyl Sn is much less likely to exist at high temperature conditions thus could represent the early disappearance of 2071 cm^{-1}. Still the exact assignment of these species is not clear.

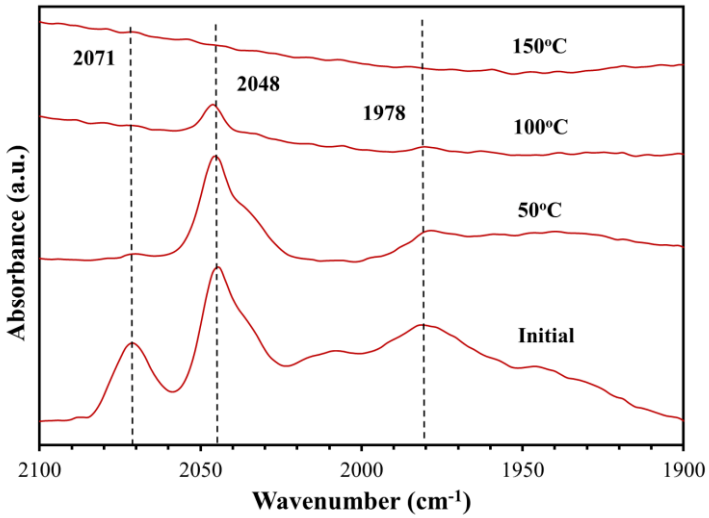

Figure 49. DRIFTS TPD study of Sn/TiO_2. CO was adsorbed on the sample for 20 min. then heated to varying temperatures. Scans were taken once sample returned to room temperature.

TPD studies with $Cu(Sn)/TiO_2$ showed similar results to Sn/TiO_2 where CO adsorbed on Sn sites are more stabilized than Cu (Fig.50). The peak at 2115 cm^{-1} corresponds to $CO\text{-}Cu^{+}$ species. Disappearance of this species is immediate with introduction of heat. This is favorable to Cu as a CO_2 reduction catalyst because strongly bound CO would act as poison deactivating catalysis. This also indicates the strong CO binding to Sn sites, Sn would not be suitable as a catalyst. TPD studies

with Cu/TiO_2 were not performed due to the weak appearance of a single peak corresponding to $CO\text{-}Cu^+$.

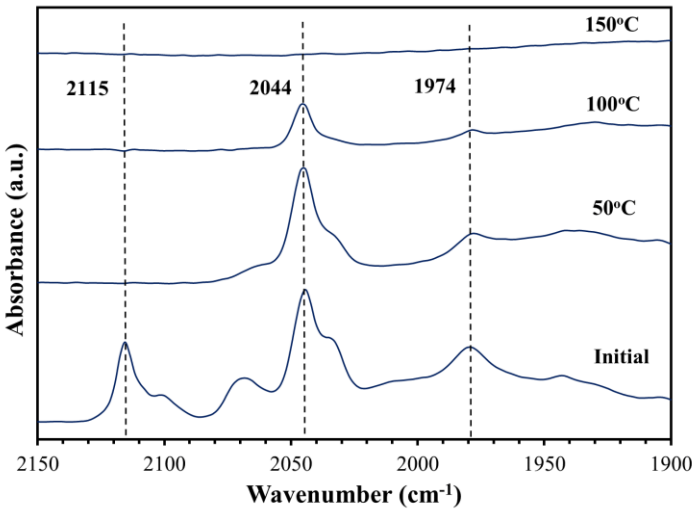

Figure 50. DRIFTS TPD study of $Cu(Sn)/TiO_2$. CO was adsorbed on the sample for 20 min. then heated to varying temperatures. Scans were taken once sample returned to room temperature.

Each experiment was repeated but samples were heated under Ar. Infrared shows similar spectra for Sn/TiO_2 and Cu/TiO_2. However $Cu(Sn)/TiO_2$ shows significant differences (Fig. 51). A new peak at 2098 cm^{-1} is present (not labeled). This new peak is also attributed to $CO\text{-}Cu^+$ however most likely shifted to a lower wavenumber due to adsorption on an aggregated site. Additionally, peaks associated with CO on Sn species are broadened indicating possible aggregation with Sn or Cu. It is not clear why heating under H_2 did not have the same aggregation effect. Cu deposited on SiO_2 has previously been studied for CO adsorption studies where bridging CO can be converted to linear CO over time.[127] It was suggested that more intense infrared peaks for CO adsorbed on Cu are linear species. This same principle can be applied to $Cu(Sn)/TiO_2$ and Sn/TiO_2 where bridged structures are not as likely for peak assignments. For peak assignments of Sn, SnO_2 has

also been studied in literature with CO adsorption studies. However, SnO_2 did not show infrared peaks from 2000 – 1800 cm^{-1}, only carbonate species.[128-129] Sn has also be doped on TiO_2 previously for solar cells and organic transformations, but CO adsorption studies have not been performed for comparison.[130-132]

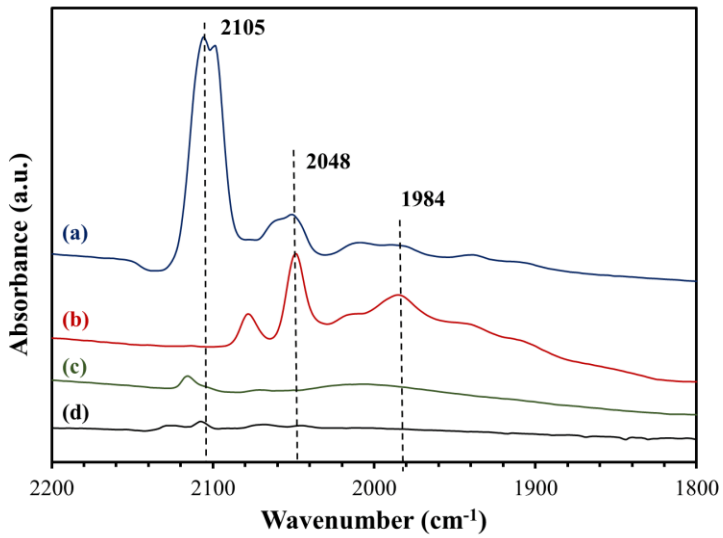

Figure 51. Difference spectra of CO adsorbed on Ar heated Cu(Sn)/TiO_2 (a) Sn/TiO_2 (b) Cu/TiO_2 (c) and P25 TiO_2 (d) in powder form. KBr was mixed with each sample and served as the background. CO was flown over each sample for 30 min then sealed.

One possibility of the strong difference in heating methods is the generation of oxygen vacancies (V_o) from H_2 heating. Reduction of TiO_2 surface and generation of V_o has been previously observed to increase photocatalytic activity.[133] It is possible that V_o present affect CO binding to Cu and Sn materials, explaining the broadness of adsorbed CO peaks and the appearance of a new CO-Cu^+ peak. To evaluate this phenomenon, new Cu/TiO_2 samples are prepared without the presence of Sn. CO bound strongly to Sn and did not desorb at high temperatures, thus is not of interest for catalyst studies. Each Cu/TiO_2 was annealed under H_2 (reducing) or O_2 (oxidizing) atmosphere at high temperature in the infrared cell prior to adsorption. CO adsorption for these

composites did not show a discernible difference in infrared spectra (Fig. 52). A singular peak at 2112 cm^{-1} corresponding to CO-Cu^{+} present further indicating the stabilization of Cu^{+} on TiO_2. It is slightly shifted from untreated Cu/TiO_2 most likely due to surface structural changes from annealing.

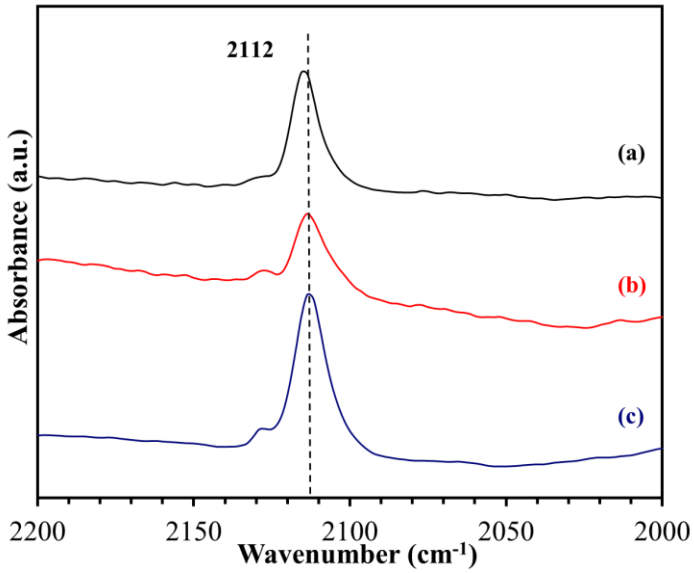

Figure 52. Difference spectra of CO adsorption on untreated Cu/TiO_2 (a) H_2-Cu/TiO_2 (b) and O_2-Cu/TiO_2 (c). KBr served as the background.

Since CO adsorption was not successful in observing changes with V_o present, CO_2 was used as an adsorption molecule. CO_2 atmosphere was introduced in the same procedure as before and infrared subtractions are seen in Figure 53. Multiple carbonate peaks are present for each sample however a band at 1638 cm^{-1} is clearly changing between samples. This band corresponds to bent CO_2 adsorption on TiO_2.[133] It is present for H_2-TiO_2 however it increases in intensity for H_2-Cu/TiO_2 as shown by Lorentzian line-shapes. This indicates that H_2 treatment generates additional V_o which in turn increases binding of bent CO_2. The presence of Cu additionally stabilizes bent

CO_2 adsorption thus increasing the intensity of the associated peak. O_2-Cu/TiO_2 also does not show this peak due to the oxidizing atmosphere decreasing the concentration of V_o on TiO_2.

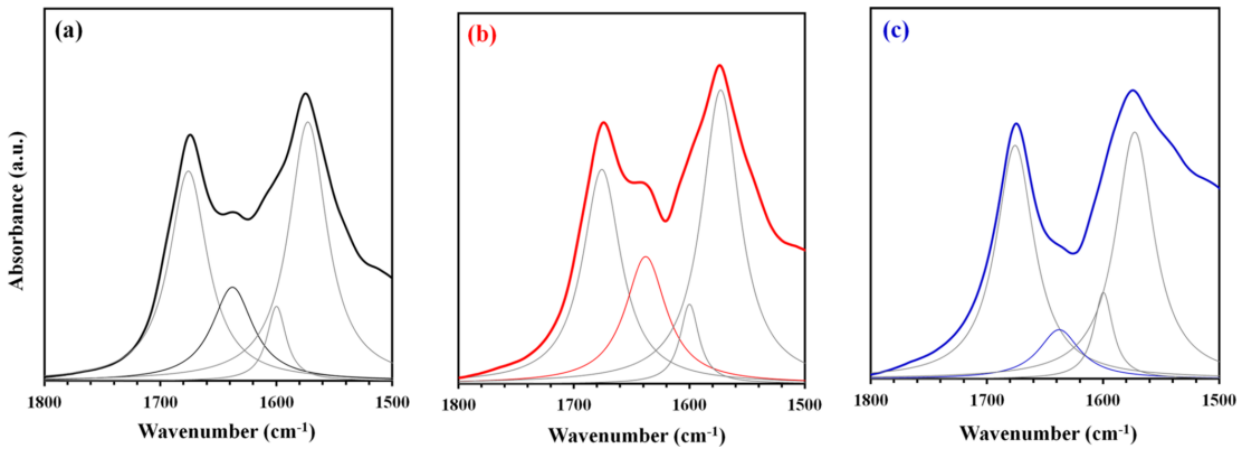

Figure 53. Difference spectra of CO_2 adsorbed on H_2-TiO_2 (a) H_2-Cu/TiO_2 (b) and O_2-Cu/TiO_2 (c). The spectra bands were fitted with Lorentzian line-shapes. The peak at 1638 cm^{-1} is indicated by coloring for each.

To evaluate the effect of V_o on photocatalytic activity CO_2 adsorption experiments were repeated (Fig. 54). Once the CO_2 was adsorbed, each sample was irradiated with UV light for 1 hr. Subtraction spectra are shown where the characteristic peak of CO-Cu^+ is observed at 2111 cm^{-1} as well as other carbonate species (not labeled). This peak is observed in H_2-Cu/TiO_2 and O_2-Cu/TiO_2 however it is more intense for H_2-Cu/TiO_2. This further suggests CO_2 reduction was more efficient for samples with increased V_o. This is due to the increased adsorption of photochemically active bent CO_2 to form CO promoted by V_o. This indicates the photocatalytic enhancement of composite materials for CO_2 reduction with increased V_o sites and the importance of their role. The presence of CO was not detected for H_2-TiO_2 however formation is likely due to the presence of increased V_o. Cu was not present thus strong CO adsorption on the surface was absent in spectra.

Repeated experiments under dark conditions also did not generate CO, indicating photoinduced dissociation of CO_2 is required.

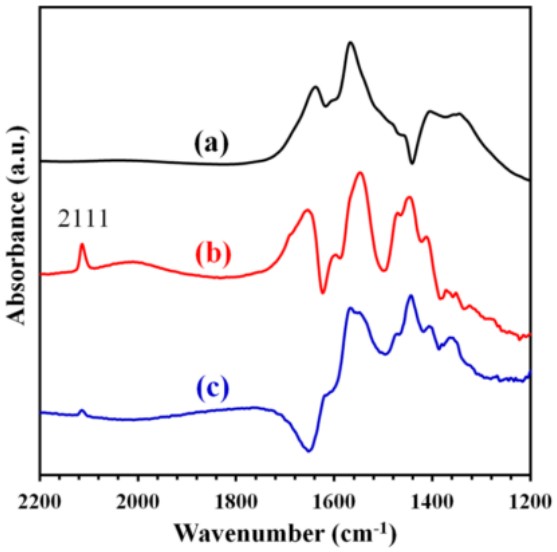

Figure 54. Difference spectra of H_2-TiO_2 (a) H_2-Cu/TiO_2 (b) and O_2-Cu/TiO_2 (c) after irradiation with UV light for 1 hr in the presence of CO_2.

One major issue of the need for V_o to enhance catalytic activity is the regeneration of V_o sites once consumed. As CO_2 disassociates, the V_o is filled by the O leaving as CO binds to Cu. After photoreaction with H_2-Cu/TiO_2, the cell was evacuated and refilled with CO_2 and irradiated with UV light again. The peak associated with CO-Cu^+ present decreased greatly, further supporting the requirement of V_o site regeneration. Future work is required to modify the composite surface where V_o can readily be regenerated during the catalytic cycle. Additionally, different synthetic methods are required to use the Sn method of Cu deposition. Sn is used in excess coating the surface for coordination sites, thus V_o are not possible. It may not be viable as a method to deposit small atomic Cu with V_o.

5.4 Summary

Atomic Cu sites were successfully deposited on TiO_2 via Sn substitution method. CO adsorption studies for all samples showed previously unseen CO adsorption species on Sn sites. TPD studies showed strong CO binding under heated conditions for Sn and weak binding on Cu^+ sites. Differences in Ar and H_2 samples led to investigation of the effect of V_o sites on TiO_2. The photocatalytic enhancement of V_o was apparent in H_2 treated samples where adsorption of bent CO_2 increased. A bent configuration is required to promote CO_2 reduction to CO. This in turn led to increased presence of CO-Cu^+ for samples treated with H_2, demonstrating the importance of bent CO_2 needed for photodissociation.

The results in this section are published in *ACS Catal*. **2018**, 8, 10464-10478.

VI. CONCLUDING REMARKS

The use of solar energy as an energy input for CO_2 reduction is highly favorable as a renewable resource. The transformation of CO_2 to solar fuels via artificial photosynthesis is crucial in the completion of the carbon cycle. Finding a suitable catalyst for this process is under investigation. This present dissertation studied several systems, ranging from hybrid to heterogeneous photocatalysts. The work focused on developing an understanding of the catalytic mechanism for each class of complexes.

Highly efficient homogeneous catalysts such as $Re(bpy)(CO)_3Cl$ have been extensively studied. A dimeric mechanism of CO_2 reduction has previously been proposed, but not thoroughly proven. Hybrid Re(I) systems have been developed to improve catalyst stability and probe this mechanism through infrared studies. Several Re(I) hybrid complexes were prepared with coupling agents forcing proximity between Re(I) centers and observed CO production in photocatalysis. The effect of derivatization and substitution of these complexes on CO_2 reduction intermediates was investigated utilizing DRIFTS. This study found the large impact of electron localization by substitution changes in turn influencing intermediate formation. Additionally, a light absorbing coupling agent was introduced in a similar study assisting light scavenging in the visible region.

Expanding upon hybrid systems, this work also investigated Co(cyclam) and Co(HMD) catalysts immobilized on mesoporous and non-porous silica. A phenomenon was discovered where heating or surface aggregation cause a color variance in the deposited Co(III) complexes. This color was associated with complex configurational changes as aggregation increased. This caused a change in catalytic selectivity and efficiency in CO_2 reduction. Additionally, previous studies were confirmed where high steric hindrance, as per HMD ligand, decreased catalytic efficiency.

Heterogeneous catalysts have also been investigated due to their promise in combination of water oxidation with CO_2 reduction as well as their stability. CoOx deposited on mesoporous and non-porous silica were investigated as a possible heterogeneous catalyst in this study. Varying loadings of CoOx were prepared; however none were successful in CO_2 reduction. Introduction of cyclam during photocatalysis however demonstrated excellent CO production with generation of an active macrocyclic catalyst *in situ*. Leaching of CoOx during photoreaction however was observed and remains a problem in future studies.

The mechanism of CO_2 reduction for Cu/TiO_2 catalysts was also investigated in this work via CO and CO_2 adsorption studies. A Sn reduction method was used to deposit reduced atomic Cu sites on TiO_2 and the role of Sn was also investigated. CO adsorbs on Sn sites strongly and in multiple configurations as determined by infrared TPD studies. Cu sites do not adsorb CO as strongly, indicating CO poisoning on possible Sn catalytic sites. Samples were also heated under reducing and oxidizing conditions to probe the role of V_o for both CO and CO_2. There was little effect observed for CO production, however a reducing atmosphere promoting formation of V_o also promoted adsorption of bent CO_2. This bent species is active for CO_2 reduction, thus aiding in knowledge of importance V_o have towards future catalyst design.

VII. LIST OF REFERENCES

1. Girishkumar, G.; McCloskey, B.; Luntz, A. C.; Swanson, S.; Wilcke, W., Lithium−Air Battery: Promise and Challenges. *J Phys Chem Lett* **2010,** *1* (14), 2193-2203.

2. Richter, B.; Goldston, D.; Crabtree, G.; Glicksman, L.; Goldstein, D.; Greene, D.; Kammen, D.; Levine, M.; Lubell, M.; Savitz, M.; D., S., Energy Future: Think Efficiency. *Am Phys Soc* **2008**.

3. Owusu, P. A.; Asumadu-Sarkodie, S., A review of renewable energy sources, sustainability issues and climate change mitigation. *Cogent Engineering* **2016,** *3* (1), 1167990.

4. Panwar, N. L.; Kaushik, S. C.; Kothari, S., Role of renewable energy sources in environmental protection: A review. *Renew Sust Energ Rev* **2011,** *15* (3), 1513-1524.

5. Goyal, H. B.; Seal, D.; Saxena, R. C., Bio-fuels from thermochemical conversion of renewable resources: A review. *Renew Sust Energ Rev* **2008,** *12* (2), 504-517.

6. Gust, D.; Moore, T. A.; Moore, A. L., Solar Fuels via Artificial Photosynthesis. *Acc Chem Res* **2009,** *42* (12), 1890-1898.

7. Hammarström, L.; Hammes-Schiffer, S., Artificial Photosynthesis and Solar Fuels. *Acc Chem Res* **2009,** *42* (12), 1859-1860.

8. Steinfeld, A., Solar thermochemical production of hydrogen—a review. *Solar Energy* **2005,** *78* (5), 603-615.

9. Kerry, Y. K. M.; Igor, C.; Joseph, G.; Edman, T. S. C., Recent Advances in CO_2 Capture and Utilization. *Chem Sus Chem* **2008,** *1* (11), 893-899.

10. Roy, S. C.; Varghese, O. K.; Paulose, M.; Grimes, C. A., Toward Solar Fuels: Photocatalytic Conversion of Carbon Dioxide to Hydrocarbons. *ACS Nano* **2010,** *4* (3), 1259-1278.

11. Smestad, G. P.; Steinfeld, A., Review: Photochemical and Thermochemical Production of Solar Fuels from H_2O and CO_2 Using Metal Oxide Catalysts. *Ind Eng Chem Res* **2012,** *51* (37), 11828-11840.

12. Grant, J.; Goswami, K.; Spreer, L.; Otvos, J.; Calvin, M., Photochemical Reduction of Carbon Dioxide to Carbon Monoxide in Water using a Nickel(II) Tetra-azamacrocycle Complex as Catalyst. *J Chem Soc, Dalton T* **1987,** (9), 2105-2109.

13. Tran, P. D.; Wong, L. H.; Barber, J.; Loo, J. S. C., Recent advances in hybrid photocatalysts for solar fuel production. *Energ Environ Sci* **2012,** *5* (3), 5902-5918.

14. Dobbek, H.; Svetlitchnyi, V.; Gremer, L.; Huber, R.; Meyer, O., Crystal Structure of a Carbon Monoxide Dehydrogenase Reveals a [Ni-4Fe-5S] Cluster. *Science* **2001,** *293* (5533), 1281-1285.

15. Ragsdale, S. W.; Kumar, M., Nickel-Containing Carbon Monoxide Dehydrogenase/Acetyl-CoA Synthase. *Chem Rev* **1996,** *96* (7), 2515-2540.

16. Kumar, B.; Llorente, M.; Froehlich, J.; Dang, T.; Sathrum, A.; Kubiak, C. P., Photochemical and Photoelectrochemical Reduction of CO_2. *Annu Rev Phys Chem* **2012,** *63* (1), 541-569.

17. Morris, A. J.; Meyer, G. J.; Fujita, E., Molecular Approaches to the Photocatalytic Reduction of Carbon Dioxide for Solar Fuels. *Accounts Chem Res* **2009,** *42* (12), 1983-1994.

18. Hawecker, J.; Lehn, J.-M.; Ziessel, R., Efficient photochemical reduction of CO_2 to CO by visible light irradiation of systems containing $Re(bipy)(CO)_3X$ or $Ru(bipy)_3^{2+}$-Co^{2+} combinations as homogeneous catalysts. *J Chem Soc, Chem Commun* **1983,** (9), 536-538.

19. Hawecker, J.; Lehn, J.-M.; Ziessel, R., Photochemical and electrochemical reduction of carbon dioxide to carbon monoxide mediated by (2,2'-bipyridine)tricarbonylchlororhenium(I) and related complexes as homogeneous catalysts. *Helv Chim Acta* **1986,** *69*, 1990-2012.

20. Sullivan, B. P.; Meyer, T. J., Photoinduced irreversible insertion of CO_2 into a metal-hydride bond. *J Chem Soc, Chem Commun* **1984,** (18), 1244-1245.

21. Sullivan, B. P.; Bolinger, C. M.; Conrad, D.; Vining, W. J.; Meyer, T. J., One- and two-electron pathways in the electrocatalytic reduction of CO_2 by fac-$Re(bpy)(CO)_3Cl$ (bpy = 2,2[prime or minute]-bipyridine). *J Chem Soc, Chem Commun* **1985,** (20), 1414-1416.

22. Kutal, C.; Weber, M. A.; Ferraudi, G.; Geiger, D., A mechanistic investigation of the photoinduced reduction of carbon dioxide mediated by tricarbonylbromo(2,2'-bipyridine)rhenium(I). *Organometallics* **1985,** *4* (12), 2161-2166.

23. Johnson, F. P. A.; George, M. W.; Hartl, F.; Turner, J. J., Electrocatalytic Reduction of CO_2 Using the Complexes $[Re(bpy)(CO)_3L]n$ (n = +1, L = $P(OEt)_3$, CH_3CN; n = 0, L = Cl^-, Otf^-; bpy = 2,2‘-Bipyridine; Otf- = CF3SO3) as Catalyst Precursors: Infrared Spectroelectrochemical Investigation. *Organometallics* **1996,** *15* (15), 3374-3387.

24. Koike, K.; Hori, H.; Ishizuka, M.; Westwell, J. R.; Takeuchi, K.; Ibusuki, T.; Enjouji, K.; Konno, H.; Sakamoto, K.; Ishitani, O., Key Process of the Photocatalytic Reduction of CO_2 Using $[Re(4,4‘-X_2\text{-bipyridine})(CO)_3PR_3]^+$ (X = CH_3, H, CF_3; PR_3 = Phosphorus Ligands): Dark Reaction of the One-Electron-Reduced Complexes with CO_2. *Organometallics* **1997,** *16* (26), 5724-5729.

25. Hayashi, Y.; Kita, S.; Brunschwig, B. S.; Fujita, E., Involvement of a Binuclear Species with the Re−C(O)O−Re Moiety in CO_2 Reduction Catalyzed by Tricarbonyl Rhenium(I) Complexes with Diimine Ligands: Strikingly Slow Formation of the Re−Re and Re−C(O)O−Re Species from Re(dmb)$(CO)_3$S (dmb = 4,4‘-Dimethyl-2,2‘-bipyridine, S = Solvent). *J Am Chem Soc* **2003,** *125* (39), 11976-11987.

26. Agarwal, J.; Fujita, E.; Schaefer, H. F.; Muckerman, J. T., Mechanisms for CO Production from CO_2 Using Reduced Rhenium Tricarbonyl Catalysts. *J Am Chem Soc* **2012,** *134* (11), 5180-5186.

27. Agarwal, J.; Johnson, R. P.; Li, G., Reduction of CO_2 on a Tricarbonyl Rhenium(I) Complex: Modeling a Catalytic Cycle. *J Phys Chem A* **2011,** *115* (13), 2877-2881.

28. Agarwal, J.; Sanders, B. C.; Fujita, E.; Schaefer Iii, H. F.; Harrop, T. C.; Muckerman, J. T., Exploring the intermediates of photochemical CO_2 reduction: reaction of Re(dmb)$(CO)_3$ COOH with CO_2. *Chem Commun* **2012,** *48* (54), 6797-6799.

29. Morimoto, T.; Nakajima, T.; Sawa, S.; Nakanishi, R.; Imori, D.; Ishitani, O., CO_2 Capture by a Rhenium(I) Complex with the Aid of Triethanolamine. *J Am Chem Soc* **2013,** *135* (45), 16825-16828.

30. Machan, C. W.; Chabolla, S. A.; Kubiak, C. P., Reductive Disproportionation of Carbon Dioxide by an Alkyl-Functionalized Pyridine Monoimine Re(I) fac-Tricarbonyl Electrocatalyst. *Organometallics* **2015,** *34* (19), 4678-4683.

31. Machan, C. W.; Chabolla, S. A.; Yin, J.; Gilson, M. K.; Tezcan, F. A.; Kubiak, C. P., Supramolecular Assembly Promotes the Electrocatalytic Reduction of Carbon Dioxide by Re(I) Bipyridine Catalysts at a Lower Overpotential. *J Am Chem Soc* **2014,** *136* (41), 14598-14607.

32. Smieja, J. M.; Kubiak, C. P., Re(bipy-tBu)$(CO)_3$Cl−improved Catalytic Activity for Reduction of Carbon Dioxide: IR-Spectroelectrochemical and Mechanistic Studies. *Inorg Chem* **2010,** *49* (20), 9283-9289.

33. Stanton, C. J.; Machan, C. W.; Vandezande, J. E.; Jin, T.; Majetich, G. F.; Schaefer, H. F.; Kubiak, C. P.; Li, G.; Agarwal, J., Re(I) NHC Complexes for Electrocatalytic Conversion of CO_2. *Inorg Chem* **2016,** *55* (6), 3136-3144.

34. Fisher, B. J.; Eisenberg, R., Electrocatalytic reduction of carbon dioxide by using macrocycles of nickel and cobalt. *J Am Chem Soc* **1980,** *102* (24), 7361-7363.

35. A., T. A. H.; M., K. T. P.; W., T. D. H. M.; A., M., Tetraaza-macrocyclic cobalt(II) and nickel(II) complexes as electron-transfer agents in the photo(electro)chemical and electrochemical reduction of carbon dioxide. *Recueil des Travaux Chimiques des Pays-Bas* **1984,** *103* (10), 288-295.

36. Fujita, E.; Szalda, D. J.; Creutz, C.; Sutin, N., Carbon dioxide activation: thermodynamics of carbon dioxide binding and the involvement of two cobalt centers in the reduction of carbon dioxide by a cobalt(I) macrocycle. *J Am Chem Soc* **1988,** *110* (14), 4870-4871.

37. Fujita, E.; Szalda, D. J., Crystallization and structure of a binuclear species containing the Co-C(OH)-O-Co moiety. *Inorg Chim Acta* **2000,** *297* (1), 139-144.

38. Schmidt, M. H.; Miskelly, G. M.; Lewis, N. S., Effects of redox potential, steric configuration, solvent, and alkali metal cations on the binding of carbon dioxide to cobalt(I) and nickel(I) macrocycles. *J Am Chem Soc* **1990,** *112* (9), 3420-3426.

39. Fujita, E.; Creutz, C.; Sutin, N.; Szalda, D. J., Carbon dioxide activation by cobalt(I) macrocycles: factors affecting carbon dioxide and carbon monoxide binding. *J Am Chem Soc* **1991,** *113* (1), 343-353.

40. Fujita, E.; Creutz, C.; Sutin, N.; Brunschwig, B. S., Carbon dioxide activation by cobalt macrocycles: evidence of hydrogen bonding between bound CO_2 and the macrocycle in solution. *Inorg Chem* **1993,** *32* (12), 2657-2662.

41. Matsuoka, S.; Yamamoto, K.; Pac, C.; Yanagida, S., Enhanced p-Terphenyl-Catalyzed Photoreduction of CO_2 to CO through the Mediation of Co(III)–Cyclam Complex. *Chem Lett* **1991,** *20* (12), 2099-2100.

42. Matsuoka, S.; Yamamoto, K.; Ogata, T.; Kusaba, M.; Nakashima, N.; Fujita, E.; Yanagida, S., Efficient and selective electron mediation of cobalt complexes with cyclam and related macrocycles in the p-terphenyl-catalyzed photoreduction of carbon dioxide. *J Am Chem Soc* **1993,** *115* (2), 601-609.

43. Ogata, T.; Yanagida, S.; Brunschwig, B. S.; Fujita, E., Mechanistic and Kinetic Studies of Cobalt Macrocycles in a Photochemical CO_2 Reduction System: Evidence of Co-CO_2 Adducts as Intermediates. *J Am Chem Soc* **1995,** *117* (25), 6708-6716.

44. Chang, X.; Wang, T.; Gong, J., CO_2 photo-reduction: insights into CO_2 activation and reaction on surfaces of photocatalysts. *Energ Environ Sci* **2016,** *9* (7), 2177-2196.

45. White, J. L.; Baruch, M. F.; Pander Iii, J. E.; Hu, Y.; Fortmeyer, I. C.; Park, J. E.; Zhang, T.; Liao, K.; Gu, J.; Yan, Y.; Shaw, T. W.; Abelev, E.; Bocarsly, A. B., Light-Driven Heterogeneous Reduction of Carbon Dioxide: Photocatalysts and Photoelectrodes. *Chem Rev* **2015,** *115* (23), 12888-12935.

46. Zhu, D. D.; Liu, J. L.; Qiao, S. Z., Recent Advances in Inorganic Heterogeneous Electrocatalysts for Reduction of Carbon Dioxide. *Adv Mater* **2016,** *28* (18), 3423-3452.

47. Fujishima, A.; Honda, K., *Nature* **1972,** *238*, 37-38.

48. Halmann, M., Photoelectrochemical Reduction of Aqueous Carbon Dioxide on P-Type Gallium Phosphide in Liquid Junction Solar Cells. *Nature* **1978,** *275* (5676), 115-116.

49. Inoue, T.; Fujishima, A. K., S.; Honda, K., *Nature* **1979,** *277*, 637-638.

50. Russell, P. G.; Kovac, N.; Srinivasan, S.; Steinberg, M., The Electrochemical Reduction of Carbon Dioxide, Formic Acid, and Formaldehyde. *J Electro Soc* **1977,** *124* (9), 1329-1338.

51. Habisreutinger, S. N.; Schmidt-Mende, L.; Stolarczyk, J. K., Photocatalytic Reduction of CO_2 on TiO_2 and Other Semiconductors. *Angew Chem Int Edit* **2013,** *52* (29), 7372-7408.

52. Ola, O.; Maroto-Valer, M. M., Review of material design and reactor engineering on TiO_2 photocatalysis for CO_2 reduction. *J Photoch Photobio C: Photoch Rev* **2015,** *24*, 16-42.

53. Low, J.; Cheng, B.; Yu, J., Surface modification and enhanced photocatalytic CO_2 reduction performance of TiO_2: a review. *Appl Surf Sci* **2017,** *392*, 658-686.

54. Zhou, X.; Liu, N.; Schmuki, P., Photocatalysis with TiO_2 Nanotubes: "Colorful" Reactivity and Designing Site-Specific Photocatalytic Centers into TiO_2 Nanotubes. *ACS Catal* **2017**, 3210-3235.

55. Park, J. H.; Kim, S.; Bard, A. J., Novel Carbon-Doped TiO_2 Nanotube Arrays with High Aspect Ratios for Efficient Solar Water Splitting. *Nano Lett* **2006,** *6* (1), 24-28.

56. Ni, M.; Leung, M. K. H.; Leung, D. Y. C.; Sumathy, K., A review and recent developments in photocatalytic water-splitting using TiO_2 for hydrogen production. *Renew Sust Energ Rev* **2007,** *11* (3), 401-425.

57. Wang, G.; Wang, H.; Ling, Y.; Tang, Y.; Yang, X.; Fitzmorris, R. C.; Wang, C.; Zhang, J. Z.; Li, Y., Hydrogen-Treated TiO_2 Nanowire Arrays for Photoelectrochemical Water Splitting. *Nano Lett* **2011,** *11* (7), 3026-3033.

58. Rauf, M. A.; Meetani, M. A.; Hisaindee, S., An overview on the photocatalytic degradation of azo dyes in the presence of TiO_2 doped with selective transition metals. *Desalination* **2011,** *276* (1), 13-27.

59. Stewart, B.; Huang, P.; He, H.; Fenton, T.; Li, G., Visible-light degradation of Orange II using an Fe(II)–terpyridine complex grafted onto TiO_2 surface. *Can J Chem* **2018,** *96* (9), 890-895.

60. Zhang, Z.; Yuan; Shi, G.; Fang, Y.; Liang, L.; Ding, H.; Jin, L., Photoelectrocatalytic Activity of Highly Ordered TiO_2 Nanotube Arrays Electrode for Azo Dye Degradation. *Environ Sci Tech* **2007,** *41* (17), 6259-6263.

61. Hirano, K.; Inoue, K.; Yatsu, T., Photocatalysed reduction of CO_2 in aqueous TiO_2 suspension mixed with copper powder. *J Photoch Photobio A: Chem* **1992,** *64* (2), 255-258.

62. Adachi, K.; Ohta, K.; Mizuno, T., Photocatalytic reduction of carbon dioxide to hydrocarbon using copper-loaded titanium dioxide. *Solar Energy* **1994,** *53* (2), 187-190.

63. Boccuzzi, F.; Chiorino, A.; Martra, G.; Gargano, M.; Ravasio, N.; Carrozzini, B., Preparation, Characterization, and Activity of Cu/TiO_2 Catalysts. I. Influence of the Preparation Method on the Dispersion of Copper in Cu/TiO_2. *J Catal* **1997,** *165* (2), 129-139.

64. Slamet; Nasution, H. W.; Purnama, E.; Kosela, S.; Gunlazuardi, J., Photocatalytic reduction of CO_2 on copper-doped Titania catalysts prepared by improved-impregnation method. *Catal Commun* **2005,** *6* (5), 313-319.

65. Nowotny, M. K.; Sheppard, L. R.; Bak, T.; Nowotny, J., Defect Chemistry of Titanium Dioxide. Application of Defect Engineering in Processing of TiO_2-Based Photocatalysts. *J Physl Chem C* **2008,** *112* (14), 5275-5300.

66. Liu, L.; Zhao, C.; Li, Y., Spontaneous Dissociation of CO_2 to CO on Defective Surface of $Cu(I)/TiO_{2-x}$ Nanoparticles at Room Temperature. *J Phys Chem C* **2012,** *116* (14), 7904-7912.

67. Liu, L.; Zhao, C.; Miller, J. T.; Li, Y., Mechanistic Study of CO_2 Photoreduction with H_2O on Cu/TiO_2 Nanocomposites by in Situ X-ray Absorption and Infrared Spectroscopies. *The J Phys Chem C* **2017,** *121* (1), 490-499.

68. Gao, C.; Wang, J.; Xu, H.; Xiong, Y., Coordination chemistry in the design of heterogeneous photocatalysts. *Chem Soc Rev* **2017**.

69. Louis, M. E.; Fenton, T. G.; Rondeau, J.; Jin, T.; Li, G., Solar CO_2 Reduction Using Surface-Immobilized Molecular Catalysts. *Comment Inorg Chem* **2016,** *36* (1), 38-60.

70. Zhao, J.; Wang, X.; Xu, Z.; Loo, J. S. C., Hybrid catalysts for photoelectrochemical reduction of carbon dioxide: a prospective review on semiconductor/metal complex co-catalyst systems. *J Mater Chem A* **2014,** *2*, 15228-15233.

71. Dubois, K. D.; He, H.; Liu, C.; Vorushilov, A. S.; Li, G., Covalent attachment of a molecular CO_2-reduction photocatalyst to mesoporous silica. *J Mol Catal A: Chem* **2012,** *363–364* (0), 208-213.

72. Liu, C.; Dubois, K. D.; Louis, M. E.; Vorushilov, A. S.; Li, G., Photocatalytic CO_2 Reduction and Surface Immobilization of a Tricarbonyl Re(I) Compound Modified with Amide Groups. *ACS Catal* **2013,** *3* (4), 655-662.

73. He, H.; Liu, C.; Louis, M. E.; Li, G., Infrared studies of a hybrid CO_2-reduction photocatalyst consisting of a molecular Re(I) complex grafted on Kaolin. *J Mol Catal A: Chem* **2014,** *395* (0), 145-150.

74. Takeda, H.; Ohashi, M.; Tani, T.; Ishitani, O.; Inagaki, S., Enhanced Photocatalysis of Rhenium(I) Complex by Light-Harvesting Periodic Mesoporous Organosilica. *Inorg Chem* **2010,** *49* (10), 4554-4559.

75. Ueda, Y.; Takeda, H.; Yui, T.; Koike, K.; Goto, Y.; Inagaki, S.; Ishitani, O., A Visible-Light Harvesting System for CO_2 Reduction Using a RuII–ReI Photocatalyst Adsorbed in Mesoporous Organosilica. *Chem Sus Chem* **2015,** *8* (3), 439-442.

76. Sekizawa, K.; Maeda, K.; Domen, K.; Koike, K.; Ishitani, O., Artificial Z-Scheme Constructed with a Supramolecular Metal Complex and Semiconductor for the Photocatalytic Reduction of CO_2. *J Am Chem Soc* **2013,** *135* (12), 4596-4599.

77. Sato, S.; Arai, T.; Morikawa, T.; Uemura, K.; Suzuki, T. M.; Tanaka, H.; Kajino, T., Selective CO_2 Conversion to Formate Conjugated with H_2O Oxidation Utilizing Semiconductor/Complex Hybrid Photocatalysts. *J Am Chem Soc* **2011,** *133* (39), 15240-15243.

78. Arai, T.; Sato, S.; Kajino, T.; Morikawa, T., Solar CO_2 reduction using H_2O by a semiconductor/metal-complex hybrid photocatalyst: enhanced efficiency and demonstration of a wireless system using $SrTiO_3$ photoanodes. *Energ Environ Sci* **2013,** *6* (4), 1274-1282.

79. Kuriki, R.; Sekizawa, K.; Ishitani, O.; Maeda, K., Visible-Light-Driven CO_2 Reduction with Carbon Nitride: Enhancing the Activity of Ruthenium Catalysts. *Ange Chem Int Edi* **2015,** *54* (8), 2406-2409.

80. Grice, K. A., Carbon dioxide reduction with homogeneous early transition metal complexes: Opportunities and challenges for developing CO_2 catalysis. *Coord Chem Rev* **2017,** *336*, 78-95.

81. Cabrera, C. R.; Abruña, H. D., Electrocatalysis of CO_2 reduction at surface modified metallic and semiconducting electrodes. *J Electroanal Chem Inter Electro Chem* **1986,** *209* (1), 101-107.

82. Kim, W.; Yuan, G.; McClure, B. A.; Frei, H., Light Induced Carbon Dioxide Reduction by Water at Binuclear ZrOCoII Unit Coupled to Ir Oxide Nanocluster Catalyst. *J Am Chem Soc* **2014,** *136* (31), 11034-11042.

83. Wang, C.; Xie, Z.; deKrafft, K. E.; Lin, W., Doping Metal–Organic Frameworks for Water Oxidation, Carbon Dioxide Reduction, and Organic Photocatalysis. *J Am Chem Soc* **2011,** *133* (34), 13445-13454.

84. Zhao, D.; Feng, J.; Huo, Q.; Melosh, N.; Fredrickson, G. H.; Chmelka, B. F.; Stucky, G. D., Triblock Copolymer Syntheses of Mesoporous Silica with Periodic 50 to 300 Angstrom Pores. *Science* **1998,** *279* (5350), 548-552.

85. Gibson, D. H.; He, H., Synthesis and properties of fac-Re(dmbpy)$(CO)_3$CHO (dmbpy = 4,4′-dimethyl-2,2′-bipyridine), a possible intermediate in reductions of CO_2 catalyzed by fac-Re(dmbpy)$(CO)_3$Cl. *Chem Commun* **2001,** (20), 2082-2083.

86. Gibson, D. H.; Yin, X.; He, H.; Mashuta, M. S., Synthesis and Reactions of fac-[Re(dmbpy)$(CO)_3$X] (dmbpy = 4,4‘-Dimethyl-2,2‘-bipyridine; X = COOH, CHO) and Their Derivatives. *Organometallics* **2003,** *22* (2), 337-346.

87. Pinchas, S.; Ben-Ishai, D., The Carbonyl Absorption of Carbamates and 2-Oxazolidones in the Infrared Region. *J Am Chem Soc* **1957,** *79* (15), 4099-4104.

88. Fei, H.; Sampson, M. D.; Lee, Y.; Kubiak, C. P.; Cohen, S. M., Photocatalytic CO_2 Reduction to Formate Using a Mn(I) Molecular Catalyst in a Robust Metal–Organic Framework. *Inorg Chem* **2015,** *54* (14), 6821-6828.

89. Fenton, T. G.; Louis, M. E.; Li, G., Effect of ligand derivatization at different positions on photochemical properties of hybrid Re(I) photocatalysts. *J Mol Catal A: Chem* **2016,** *411*, 272-278.

90. Appel, A. M.; Bercaw, J. E.; Bocarsly, A. B.; Dobbek, H.; DuBois, D. L.; Dupuis, M.; Ferry, J. G.; Fujita, E.; Hille, R.; Kenis, P. J. A.; Kerfeld, C. A.; Morris, R. H.; Peden, C. H. F.; Portis, A. R.; Ragsdale, S. W.; Rauchfuss, T. B.; Reek, J. N. H.; Seefeldt, L. C.; Thauer, R. K.; Waldrop, G. L., Frontiers, Opportunities, and Challenges in Biochemical and Chemical Catalysis of CO_2 Fixation. *Chem Rev* **2013,** *113* (8), 6621-6658.

91. Elgrishi, N.; Chambers, M. B.; Wang, X.; Fontecave, M., Molecular polypyridine-based metal complexes as catalysts for the reduction of CO_2. *Chem Soc Rev* **2017,** *46* (3), 761-796.

92. Takeda, H.; Cometto, C.; Ishitani, O.; Robert, M., Electrons, Photons, Protons and Earth-Abundant Metal Complexes for Molecular Catalysis of CO_2 Reduction. *ACS Catal* **2017,** *7* (1), 70-88.

93. Ogata, T.; Yamamoto, Y.; Wada, Y.; Murakoshi, K.; Kusaba, M.; Nakashima, N.; Ishida, A.; Takamuku, S.; Yanagida, S., Phenazine-Photosensitized Reduction of CO_2 Mediated by a Cobalt-Cyclam Complex through Electron and Hydrogen Transfer. *J Phys Chem* **1995,** *99* (31), 11916-11922.

94. Fujita, E.; Furenlid, L. R.; Renner, M. W., Direct XANES Evidence for Charge Transfer in Co−CO_2 Complexes. *J Am Chem Soc* **1997,** *119* (19), 4549-4550.

95. Jin, T.; Liu, C.; Li, G., Photocatalytic CO_2 reduction using a molecular cobalt complex deposited on TiO_2 nanoparticles. *Chem Commun* **2014,** *50* (47), 6221-6224.

96. Jin, T.; Liu, C.; Li, G., Heterogenization of a macrocyclic cobalt complex for photocatalytic CO_2 reduction. *J Coord Chem* **2016,** *69* (11-13), 1748-1758.

97. Bosnich, B.; Poon, C. K.; Tobe, M. L., Complexes of Cobalt(III) with a Cyclic Tetradentate Secondary Amine. *Inorg Chem* **1965,** *4* (8), 1102-1108.

98. Curtis, N. F.; Hay, R. W., A novel heterocycle synthesis. Formation of 5,7,7,12,14,14-hexamethyl-1,4,8,11-tetra-azacyclotetradeca-4,11-diene dihydroperchlorate by reaction of diaminoethane monohydroperchlorate with mesityl oxide or acetone. *Chem Commun (London)* **1966,** (15), 524-525.

99. Kildahl, N. K., A simple demonstration of reversible oxygenation. *J Chem Edu* **1983,** *60* (10), 898.

100. Cook, T. D.; Fanwick, P. E.; Ren, T., Unsymmetric Mononuclear and Bridged Dinuclear Co^{III}(cyclam) Acetylides. *Organometallics* **2014,** *33* (18), 4621-4624.

101. Cook, T. D.; Natoli, S. N.; Fanwick, P. E.; Ren, T., Dimeric Complexes of Co^{III}(cyclam) with a Polyynediyl Bridge. *Organometallics* **2015,** *34* (4), 686-689.

102. Natoli, S. N.; Cook, T. D.; Abraham, T. R.; Kiernicki, J. J.; Fanwick, P. E.; Ren, T., Cobalt(III) Bridged by gem-DEE: Facile Access to a New Type of Cross-Conjugated Organometallics. *Organometallics* **2015,** *34* (21), 5207-5209.

103. Sujandi; Han, S.-C.; Han, D.-S.; Jin, M.-J.; Park, S.-E., Catalytic oxidation of cycloolefins over Co(cyclam)-functionalized SBA-15 material with H_2O_2. *J Catal* **2006,** *243* (2), 410-419.

104. Jiao, F. F., Heinz, Nanostructured Cobalt and Manganese Oxide Clusters as Efficient Water Oxidation Catalysts. *Energ Environ Sci* **2010,** *3*, 1018-1027.

105. Wang, L.-P.; Van Voorhis, T., Direct-Coupling O_2 Bond Forming a Pathway in Cobalt Oxide Water Oxidation Catalysts. *J Phys Chem Lett* **2011,** *2* (17), 2200-2204.

106. Agiral, A.; Soo, H. S.; Frei, H., Visible Light Induced Hole Transport from Sensitizer to Co_3O_4 Water Oxidation Catalyst across Nanoscale Silica Barrier with Embedded Molecular Wires. *Chem Mater* **2013,** *25* (11), 2264-2273.

107. Deng, X.; Tüysüz, H., Cobalt-Oxide-Based Materials as Water Oxidation Catalyst: Recent Progress and Challenges. *ACS Catal* **2014,** *4* (10), 3701-3714.

108. Yang, J.; Walczak, K.; Anzenberg, E.; Toma, F. M.; Yuan, G.; Beeman, J.; Schwartzberg, A.; Lin, Y.; Hettick, M.; Javey, A.; Ager, J. W.; Yano, J.; Frei, H.; Sharp, I. D., Efficient and Sustained Photoelectrochemical Water Oxidation by Cobalt Oxide/Silicon Photoanodes with Nanotextured Interfaces. *J Am Chem Soc* **2014,** *136* (17), 6191-6194.

109. Zhang, M.; de Respinis, M.; Frei, H., Time-resolved observations of water oxidation intermediates on a cobalt oxide nanoparticle catalyst. *Nature Chem* **2014,** *6*, 362.

110. Kim, W.; McClure, B. A.; Edri, E.; Frei, H., Coupling carbon dioxide reduction with water oxidation in nanoscale photocatalytic assemblies. *Chem Soc Rev* **2016,** *45* (11), 3221-3243.

111. Iwase, A.; Yoshino, S.; Takayama, T.; Ng, Y. H.; Amal, R.; Kudo, A., Water Splitting and CO_2 Reduction under Visible Light Irradiation Using Z-Scheme Systems Consisting of Metal Sulfides, CoOx-Loaded $BiVO_4$, and a Reduced Graphene Oxide Electron Mediator. *J Am Chem Soc* **2016,** *138* (32), 10260-10264.

112. Melaet, G.; Ralston, W. T.; Li, C.-S.; Alayoglu, S.; An, K.; Musselwhite, N.; Kalkan, B.; Somorjai, G. A., Evidence of Highly Active Cobalt Oxide Catalyst for the Fischer–Tropsch Synthesis and CO_2 Hydrogenation. *J Am Chem Soc* **2014,** *136* (6), 2260-2263.

113. Han, H.; Frei, H., Visible light absorption of binuclear $TiOCo^{II}$ charge-transfer unit assembled in mesoporous silica. *Mat Res S C* **2007,** *103* (1–3), 265-272.

114. Han, H.; Frei, H., Controlled Assembly of Hetero-binuclear Sites on Mesoporous Silica: Visible Light Charge-Transfer Units with Selectable Redox Properties. *J Phys Chem C* **2008,** *112* (22), 8391-8399.

115. Edri, E.; Frei, H., Charge Transport through Organic Molecular Wires Embedded in Ultrathin Insulating Inorganic Layer. *J Phys Chem C* **2015,** *119* (51), 28326-28334.

116. Yamazaki, Y.; Takeda, H.; Ishitani, O., Photocatalytic reduction of CO_2 using metal complexes. *J Photoch Photobio C: Photochem Rev* **2015,** *25*, 106-137.

117. Jiao, F.; Frei, H., Nanostructured Cobalt Oxide Clusters in Mesoporous Silica as Efficient Oxygen-Evolving Catalysts. *Angew Chem Int Edit* **2009,** *48* (10), 1841-1844.

118. Liang, Y.; Wang, H.; Diao, P.; Chang, W.; Hong, G.; Li, Y.; Gong, M.; Xie, L.; Zhou, J.; Wang, J.; Regier, T. Z.; Wei, F.; Dai, H., Oxygen Reduction Electrocatalyst Based on Strongly Coupled Cobalt Oxide Nanocrystals and Carbon Nanotubes. *J Am Chem Soc* **2012,** *134* (38), 15849-15857.

119. Salgueiriño-Maceira, V.; Spasova, M.; Farle, M., Water-Stable, Magnetic Silica–Cobalt/Cobalt Oxide–Silica Multishell Submicrometer Spheres. *Adv Func Mater* **2005,** *15* (6), 1036-1040.

120. Yacou, C.; Smart, S.; Diniz da Costa, J. C., Long term performance cobalt oxide silica membrane module for high temperature H_2 separation. *Energ Environ Sci* **2012,** *5* (2), 5820-5832.

121. Jin, Q.; Fujishima, M.; Iwaszuk, A.; Nolan, M.; Tada, H., Loading Effect in Copper(II) Oxide Cluster-Surface-Modified Titanium(IV) Oxide on Visible- and UV-Light Activities. *J Phys Chem C* **2013,** *117* (45), 23848-23857.

122. Li, G.; Dimitrijevic, N. M.; Chen, L.; Rajh, T.; Gray, K. A., Role of Surface/Interfacial Cu^{2+} Sites in the Photocatalytic Activity of Coupled CuO−TiO_2 Nanocomposites. *J Phys Chemy C* **2008,** *112* (48), 19040-19044.

123. Iyemperumal, S. K.; Deskins, N. A., Activation of CO_2 by supported Cu clusters. *Phys Chem Chem Phys* **2017,** *19* (42), 28788-28807.

124. Li, Q.; Fu, J.; Zhu, W.; Chen, Z.; Shen, B.; Wu, L.; Xi, Z.; Wang, T.; Lu, G.; Zhu, J.-j.; Sun, S., Tuning Sn-Catalysis for Electrochemical Reduction of CO_2 to CO via the Core/Shell Cu/SnO_2 Structure. *J Am Chem Soc* **2017,** *139* (12), 4290-4293.

125. Liu, C.; Iyemperumal, S. K.; Deskins, N. A.; Li, G., Photocatalytic CO_2 reduction by highly dispersed Cu sites on TiO_2. *Photo E* **2016,** *7* (1), 012004-012004.

126. León, A.; Reuquen, P.; Garín, C.; Segura, R.; Vargas, P.; Zapata, P.; Orihuela, P., FTIR and Raman Characterization of TiO2 Nanoparticles Coated with Polyethylene Glycol as Carrier for 2-Methoxyestradiol. *Appl Sci* **2017,** *7* (1), 49.

127. Hadjiivanov, K.; Venkov, T.; Knözinger, H., FTIR Spectroscopic Study of CO Adsorption on Cu/SiO_2: Formation of New Types of Copper Carbonyls. *Catal Lett* **2001,** *75* (1), 55-59.

128. Emiroglu, S.; Bârsan, N.; Weimar, U.; Hoffmann, V., In situ diffuse reflectance infrared spectroscopy study of CO adsorption on SnO_2. *Thin Solid Films* **2001,** *391* (2), 176-185.

129. Melle-Franco, M.; Pacchioni, G., CO adsorption on SnO_2(110): cluster and periodic ab initio calculations. *Surf Sci* **2000,** *461* (1), 54-66.

130. Deshmane, V. G.; Owen, S. L.; Abrokwah, R. Y.; Kuila, D., Mesoporous nanocrystalline TiO_2 supported metal (Cu, Co, Ni, Pd, Zn, and Sn) catalysts: Effect of metal-support interactions on steam reforming of methanol. *J Mol Catal A: Chem* **2015,** *408*, 202-213.

131. Duan, Y.; Fu, N.; Liu, Q.; Fang, Y.; Zhou, X.; Zhang, J.; Lin, Y., Sn-Doped TiO_2 Photoanode for Dye-Sensitized Solar Cells. *J Phys Chem C* **2012,** *116* (16), 8888-8893.

132. Wang, E.; He, T.; Zhao, L.; Chen, Y.; Cao, Y., Improved visible light photocatalytic activity of titania doped with tin and nitrogen. *J Mater Chem* **2011,** *21*, 144-150.

133. Rasko, J.; Solymosi, F., Infrared Spectroscopic Study of the Photoinduced Activation of CO_2 on TiO_2 and Rh/TiO_2 Catalysts *J Phys Chem* **1994,** *98*, 7147 - 7152.